Development and Deployment of Optical Instruments to Measure Trace Atmospheric Species: I. Water Isotopologues; II. Glyoxal; III. Iodine Monoxide

Thesis advisor

Professor James G. Anderson

Author

Anthony Scott O'Brien

Development and Deployment of Optical Instruments to Measure Trace Atmospheric Species: I. Water Isotopologues; II. Glyoxal; III. Iodine Monoxide

Abstract

Understanding future climate requires observations of trace species that can significantly influence the chemical or radiative properties of the atmosphere. The development of optical instruments, utilizing laser-systems as high-resolution light sources, for making *in situ* observations of trace species from either airborne- or ground-based platforms and results from field campaigns are presented.

Glyoxal, the smallest α-dicarbonyl, is a common product during the oxidation of volatile organic compounds. An instrument using the technique of laser-induced phosphorescence was developed to measure glyoxal at the part per trillion by volume (pptv) level from a tower in a forest canopy. The instrument was deployed as part of the Community Atmosphere-Biosphere INteractions EXperiment. The instrumental limit of detection is 3 pptv with a 1-minute acquisition time. Nearly continuous measurements of glyoxal ranging between 5 – 75 pptv were acquired throughout the campaign and vertical gradients in the forest canopy were found to be driven by elevated temperature.

A sensitive instrument using laser-induced fluorescence detection was developed and deployed into remote marine environments to measure iodine monoxide (IO) where the mixing ratio is on the order of 1 – 5 pptv. The challenges and solutions of operating in this environment and results from the field and laboratory are discussed. Laboratory experiments show that IO can be generated from *Laminaria digitata*, a subtidal kelp species, in the presence of ozone.

Observations of the isotopic composition of condensed and vapor water above a large summertime tropical convective system obtained by Hoxotope and ICOS instruments during the TC4 campaign are used to analyze the role of convection in the lower tropical transition layer (TTL). Regions of ice that are characteristic of either convective lofting or in situ condensation are encountered above an active deep tropical convective system. Ice is an important component of water transport models in the TTL, yet its isotopic composition is a relatively unconstrained parameter. The implications from the direct observations of the isotopic composition of ice during convection is explored with respect to transport models of water in the TTL.

Contents

List of Figures

List of Tables

Acknowledgments

Through the years I have spent with group, I have had the good fortune of working alongside many great people, to whom it is impossible to convey my sincerest gratitude. What I offer here can only be taken as a small token of thanks owed to them.

Joe Demusz, you are a true friend and mentor. You always provided advice, and the best of it came unsolicited, that found a welcome home. Your insistence on teaching me electronics planted a seed that is just starting to grow. Tom Hanisco, thank you for inviting me to join the water isotopes project and showing me how experimental work is done, and how it's done right.

The development of the instruments discussed here brought me into close contact with the engineering team, a group of wonderful people who taught me so much and whose lessons I will carry with me for the rest of my life. Marco Rivero, you're willingness to always lend a hand made solving problems so much easier. Terry Martin, you are a paragon of grace under pressure. Ed Thompson, your reprise brought with it so much warmth. Norton Allen, you provided a sounding board that kept a non-programmer from wandering too far of the path. Larry Lapson, your return got us back on track. Mike Greenberg & Chris Tuozzolo, thank you for making the mechanical office such a welcome place to chat, in addition to introducing me to the concept of style points and the portable machine shop (a hand drill and a file, no less!).

Through the years I've had many office mates who've made it the zany place it is: Maryanne Sargent, Reem Hannun, Meghan Thurlow, Claire Healy, Jason Munster, Andy Ho, Yi-wen Huang, Dick Co, David Sayres, Jason St. Clair, Jon Gero, and

across the hallway, making you a part of the office whether you choose to be or not, Stephen Leroy. Rob Stanhope, you introduced me to the best of what Boston has to offer. John Dykema, I enjoyed the time we spent sharing pints and talking shop. The friendships I've formed in the group won't be forgotten.

For those of you who I have spent time in the field with: Meghan Thurlow, Reem Hannun, David Sayres, Jessica Smith, Mark Witinski, Jason St. Clair, Elliot Weinstock, Tom Hanisco, Chris Tuozzolo, Norton Allen, Marco Rivero, and Joe Demusz. Thank you for making the enjoyable place it was. And to those who I wasn't in the field with, and who remained in Cambridge, thank you for your help in getting us out of the door in the first place: Lenny Solomon, Rob Stanhope, Tara Manicsic, Joyce Eather, Terry Martin, Ed Thompson, Mike Greenberg, Matt Knight, Bob Lalibertè, David Wilmouth, Claire Healy, Jason Munster, Nick Demusz and Danny Spillane.

My parents, Thomas and Anne, provided constant support and were there every time I came to a fork in the road. To my brother, Marc: while our paths through this world may be very different, your pride in mine is a reflection of the courage you've embraced to follow yours. To my wife, and so much more, Katie, this is as much yours as it is mine—I honestly could not have done this without you.

And, finally, to my advisor Jim Anderson. Thank you for building the group you have—the science you lead and the people you've gathered speak to how truly a unique and incredible place it is to be a part of. My path through graduate school has not been traditional, and all the while your enthusiasm knew no bounds and your support has been infinite.

To my family, Thomas, Anne, Marc and Katie—
who showed me the world and encouraged
me to explore it in my own way.

Chapter 1

Introduction

> There is, as every schoolboy knows in this scientific age, a very close chemical relation between coal and diamonds. It is the reason, I believe, why some people allude to coal as "black diamonds." Both these commodities represent wealth; but coal is a much less portable form of property. There is, from that point of view, a deplorable lack of concentration in coal. Now, if a coal-mine could be put into one's waistcoat pocket—but it can't! At the same time, there is a fascination in coal, the supreme commodity of the age in which we are camped like bewildered travellers in a garish, unrestful hotel.
>
> ---
>
> *Victory*
> Joseph Conrad

In many respects the story of climate is deeply entwined with our demands for energy. The extraction, application, and transformation of energy has nourished humanity from the time of antiquity. Unique to carbon is a property that allows it to form long molecular chains, and to us, the ability to liberate an abstract form of free energy, available to do work, from the enthalpy and entropy that comes with the rearrangement of the atoms in those chains.

It was not until the time of the Industrial Revolution that this concept was fully refined and it became apparent that humankind could be responsible for directly altering the environment, and for good reason: this was the first time in the history of the Earth where natural resources were being exploited to feed the energy demands of a vast industrial machine. Near the turn of the 19^{th} century, an estimated 500 million tons of coal were being burned annually. This machine has grown at an exponential rate—driving economies, generating wealth, and enabling an explosion in population.

Yet energy is not the villain in this story. By the metrics available to judge quality of life and living conditions (e.g., infant mortality, life expectancy at birth, food availability, and adult literacy), improvements in these are well correlated with the availability of energy (Smil, 2005). It is the limited attention cast upon the sources and sinks required to generate this energy that leads to our predicament. Our direct impact on the chemical composition of the atmosphere is iconically demonstrated by the long-term, "routine" measurements of atmospheric CO_2 made by Charles David Keeling atop Mauna Loa, where the concentration in the mid-troposphere has steadily risen from 315 ppmv in 1960 to just shy of 390 ppmv today (Sundquist and Keeling, 2009).

Atmospheric CO_2 levels have changed throughout Earth's history and ice core observations reveal tight correlations between surface temperatures and the concentration of CO_2 in the atmosphere (Petit et al., 1999; Siegenthaler et al., 2005). Extreme contrasts in the Earth's climate are found between the Eocene (50 Ma) and the Last Glacial Maximum (20 ka), with temperatures in the high-latitudes supporting either tropical-like conditions or mile-thick ice sheets, respectively. The level of CO_2 in the atmosphere was about 90 ppmv lower during the Last Glacial Maximum (Lüthi et al., 2008) than the pre-industrial concentration of 280 ppmv. During the Eocene, CO_2 was four-times higher with an atmospheric mixing ratio that exceeded 1100 ppmv (Lowenstein and Demicco, 2006).

The most recent assessment report from the Intergovernmental Panel on Climate Change (IPCC) projects that atmospheric CO_2 will be somewhere between 550 – 950 ppmv by the end of the century, and is largely dependent on the socio-economic storyline we choose to follow (Solomon, 2007). At the high end of the projection scenarios, the large increase in CO_2 is driven by rapid economic growth, substantial reduction in income disparity and a priority to pursue personal wealth rather than environmental quality. Alternatively, a 550 ppmv CO_2 scenario is the result of a society with reductions in material intensity, a shift in economic structures toward one served chiefly through information and services and a high level of environmental and social consciousness that brings with it sustainable development through the introduction of clean and resource-efficient technologies. What these scenarios mean can only be interpreted by two methods: by looking at the history of the Earth's past through the records of paleoclimate or by simulating global climate with the

application of physics and chemistry to numerical models of the Earth, and neither can stand in isolation.

1.1 Energy in Balance: A Simple Climate Model

A simple model of the radiative balance of the Earth serves to illustrate the importance of an atmosphere in determining surface temperatures and the factors which influence surface temperatures. Such a model can be found in many introductory texts (e.g., Jacob, 1999; Houghton, 2002) so rather than focusing on the details of its development, the salient results are emphasized.

The total solar radiation intercepted by the Earth is determined by its distance from the Sun and the solar photon flux, set by the temperature of the Sun. Together these yield the solar constant for the Earth, $F_s = 1370$ W m^{-2}. The total incoming radiation at the top of the atmosphere is the product of the intercepted area, a circular disk that is equivalent to the cross-sectional area of the Earth, and the solar constant. As this radiation travels through the atmosphere to the surface of the Earth a fraction of it can be intercepted and reflected (e.g., by ice and aerosols) directly back into space such that the total radiation at the surface is attenuated by what is termed the planetary albedo A and currently has a value of 0.28. The total solar radiation that reaches the surface of the Earth is $F_s(1 - A)\pi R_E^2$, where R_E is the radius of the Earth. The mean solar radiation per unit area of the Earth's surface is found from the quotient of the total solar radiation at the surface and the total surface area of the Earth, $4\pi R_E^2$.

In order for the Earth to maintain thermal equilibrium, that is, a net zero rate of cooling or heating, the amount of outgoing radiation must be equivalent to the incoming radiation. Then the Earth must, too, act as blackbody radiator where the surface temperature is dictated by the radiation received:

$$\sigma T_0^4 = \frac{F_s(1-A)}{4} \tag{1.1}$$

where $\sigma = 5.67 \times 10^{-8}$ J s^{-1} m^{-2} K^{-4} is the Stefan-Boltzmann constant. Solving for the temperature yields an uncharacteristically cool surface temperature of the Earth, $T_0 = 255$ K. Such a result is similar to that obtained by Fourier, who then went on to suggest that the atmosphere must be responsible for trapping invisible heat rays.

While this simple radiative model (Eq. 1.1) has neglected the presence of an atmosphere it can be adjusted to mimic an atmosphere that is made up of a single layer of gases that is transparent to incoming shortwave (visible) solar radiation but absorbs some fraction f of outgoing longwave (infrared) radiation:

$$(1-f)\sigma T_0^4 + f\sigma T_1^4 = \frac{F_s(1-A)}{4} \tag{1.2}$$

Equation 1.2 is similar to Eq. 1.1 but accounts for the energy balance of the Earth and atmosphere system, where only a fraction $(1-f)$ of the outgoing surface radiation is emitted to space and there is the presence of a second blackbody (the atmospheric layer) at a cooler temperature T_1 which reemits the absorbed fraction. The temperature of the atmospheric layer is determined by its own energy balance equation: input energy is equivalent to the fraction of outgoing radiation the layer absorbs and

the outgoing radiation must be isotropic, such that it radiates an equivalent amount to space and back to Earth,

$$f\sigma T_0^4 = 2f\sigma T_1^4 \tag{1.3}$$

Combining the energy balance equation of the atmospheric layer with Eq. 1.2 yields the surface temperature of the Earth,

$$T_0 = \left[\frac{F_s(1-A)}{4\sigma(1-f/2)}\right]^{1/4} \tag{1.4}$$

which is controlled by the optical thickness or, equivalently, the fractional absorption of the atmospheric layer. A global mean surface temperature of 288 K corresponds to an atmosphere that absorbs 77 % of outgoing radiation in this simple model.

While this model does not account for the fact that atmospheric molecules do not uniformly absorb across all wavelengths or that the atmosphere is a continuously absorbing medium where density decreases with height, it encapsulates the foundation of the climate system. In the absence of variations in solar output or top of atmosphere insolation (i.e., Milankovitch cycles) the climate system can only be altered through changes in albedo or the amount of outgoing radiation that is absorbed. Processes that alter the structure or composition of the surface of the Earth (e.g., land use changes and cryosphere dynamics) or the atmosphere can directly impact climate. Feedbacks between the Earth (land, ocean and ice) and atmosphere systems can also induce indirect changes in climate.

In 1859, John Tyndall set out to determine if any of the gases comprising air could trap heat rays. Through careful laboratory work he identified several that

did, water vapor as the principal absorber of heat with significant contributions from CO_2, despite its relatively low abundance. With regard to these gases, he wrote (Tyndall, 1863), it were "as a dam built across a river causes a local deepening of the stream, so our atmosphere, thrown as a barrier across the terrestrial [infrared] rays, produces a local heightening at the Earth's surface."

The energy imbalance that Tyndall wrote of can be seen in the increasing heat content of the ocean, which over the last 5 decades has increased on the order of 100×10^{21} J (Levitus et al., 2005). Another 15×10^{21} J has flowed into the cryosphere over this same period, with much of it responsible for melting Arctic sea ice. Over this period, sea level has risen by about 100 mm, which corresponds to a historical trend of 1.9 mm year^{-1} (Church and White, 2011). In the Fourth Assessment Report by the IPCC it was suggested that approximately half this rise comes from thermal expansion of the oceans and the other half from land-sourced meltwater (Solomon, 2007) but recent data from a global network of ocean floats indicates that ocean thermal expansion is plateauing (Cazenave et al., 2009). Satellite altimetry data, available since 1993, suggest, that when considering only the last two decades, the rate of sea level rise has increased to 3.2 ± 0.4 mm yr^{-1} (Church and White, 2011). A consistent record of ice sheet mass balance over this two decade period implies that this increase in sea level rise is the result of the acceleration in combined Greenland and Antarctic ice sheet loss, which has outpaced the acceleration in glacier and ice cap loss; to illustrate the magnitude of this contribution, consider that in 2006 the combined loss of the Greenland and Antarctic ice sheet mass was estimated at 475 ± 158 Gt year^{-1}, equivalent to 1.3 ± 0.4 mm year^{-1} of sea level rise (Rignot et al.,

2011). Even at a stagnant rate, the 2006 rate indicates that sea level rise by the end of this century from the ice sheets alone will surpass the maximum estimates in the Fourth Assessment Report by a factor of 2 (Solomon, 2007). Estimates place the global mean sea level rise from the Greenland ice sheet at 7 m, such a dramatic rise illustrates the magnitude of the impact that an imbalance in the energy structure of the climate system has; the social and economic consequences of new climate states become readily apparent.

1.1.1 Climate Feedbacks

The climate system is not itself an isolated system, where the only variable of importance is temperature; it is part of global system where chemical and hydrological cycles are tightly coupled. It is not a new concept that changes in the climate system beget changes in the physical structure of the Earth, which in turn, beget changes in the climate system *ad infinitum* until a new state of equilibrium is reached. In a 1905 letter to C. G. Abbott, T. C. Chamberlain wrote (Fleming, 1998)

> Water vapor, confessedly the greatest thermal absorbent in the atmosphere, is dependent on temperature for its amount, and if another agent, as CO_2, not so dependent, raises the temperature of the surface, it calls into function a certain amount of water vapor which further absorbs heat, raises the temperature and calls forth for more vapor ...

This statement depicts the concept of positive feedbacks. While water vapor (and associated clouds) is often called the dominant greenhouse gas in the atmosphere, accounting for 75 % of the terrestrial radiation absorbed in the present day greenhouse effect (Schmidt et al., 2010), it is not considered a forcing agent. When

water vapor condenses to form clouds, the situation becomes increasingly complex. Condensed water enhances the absorption of outgoing longwave radiation but can also decrease the fraction of incoming solar radiation by reflecting it back to space, this feedback is termed the albedo effect of clouds. Accordingly, the IPCC (Solomon, 2007) has stated that "cloud feedbacks remain the largest source of uncertainty in climate sensitivity estimates." Cloud formation is primarily controlled through the horizontal and vertical distribution of water vapor and the temperature structure of the atmosphere.

Condensation and evaporation processes limit the lifetime of water vapor in the troposphere to roughly 10 days, whereas CO_2 and CH_4 have lifetimes on the order of many centuries and a decade, respectively. It is these non-condensing greenhouse gases, with CO_2 primary amongst them, which provide the stable temperature structure of the atmosphere that determines the water vapor distribution in such a way that CO_2 can be considered the "principal control knob governing Earth's temperature" (Lacis et al., 2010).

Only in the stratosphere, where the residence time of water vapor is on the order of years, can water vapor be considered a forcing agent. Understanding the mechanisms that control this distribution is therefore a necessity to minimizing the uncertainty in predicting future climate. At the crux of the climate issue is then understanding the response of water vapor to changes in CO_2; or equivalently, determining the components of the chain that make up mathematical expression $\partial[H_2O]_v/\partial[CO_2]$.

1.2 Stratospheric Water Vapor

Water vapor modulates stratospheric ozone in two ways. Firstly, it can directly enter into chemical reactions that dictate the concentration of ozone in the stratosphere. Secondly, it influences the radiative balance of the stratosphere which dictates the threshold temperature for the onset of heterogenous chemistry.

1.2.1 Stratospheric Ozone and Surface UV Dosage

An accurate assessment of ozone recovery and the associated UV flux at the Earth's surface requires long term monitoring in order to fully understand the factors which contribute directly to, and to the uncertainty of, ozone loss. Namely, such observations are aimed at decoupling changes in stratospheric ozone from decreases in ozone-depleting substances, controlled or banned by the 1987 Montreal Protocol and its subsequent amendments, from other factors that can include natural variability, stratospheric cooling and observational uncertainties.

Generally, stratospheric profiles of mid-latitude ozone (35 °N – 60 °N) have ceased to decline since the mid-1990s, however, on a global scale, signs of recovery are statistically small to none (WMO, 2011). Where long-term and large spatial-scale reconstructions of surface UV radiation (280 – 400 nm) can be made, increases are correlated with the observed decreases in column ozone. Additionally, surface level UV radiation can also be significantly influenced by cloud and aerosol activity (Seckmeyer et al., 2008; den Outer et al., 2005; McKenzie et al., 2008).

UV radiation has been linked to skin cancer (Setlow, 1974), cataracts (Taylor

et al., 1988) and adverse influences on biological production (Caldwell et al., 2007), in addition to hastened degradation of infrastructure materials. Indeed, the development of life on land was not possible until 500 Ma, when atmospheric oxygen and ozone levels reached near present values. At one extreme, models predict that in the scenario avoided (i.e., the absence of the Montreal protocol), that 67 % of globally-averaged column ozone would be destroyed by 2065, relative to 1980 levels, and the rate of skin cancer would be amplified by a factor of 5 (Newman et al., 2009; Newman and McKenzie, 2011). While halogen levels are not increasing, they are still high and this makes the stratosphere remain in a state of susceptibility—the WMO (2011) has recently stated that "substantial ozone losses could occur if stratospheric aerosol loading were to increase in the next few decades, while halogen levels are high."

1.2.2 Oxidation of Water in the Stratosphere

The only sink of water vapor in the upper atmosphere is through photochemical loss. One pathway by which this occurs is through direct photolysis, where water is directly photolyzed to produce OH and H radicals

$$\mathrm{H_2O} + h\nu \;\rightarrow\; \mathrm{H} + \mathrm{OH}. \tag{1.5}$$

Both products are part of the HO_x family. Atomic hydrogen is converted to HO_2 through either reaction with O_2 (cf., Rxn. 2.12) or ozone. This reaction occurs primarily in the mesosphere (above 61 km) where Lyman-α ($\sim$121 nm) and the

Schumann-Runge band (175–200 nm) fluxes are greater and photolysis can proceed.

In the stratosphere photochemical dissociation of ozone and the subsequent oxidation of water (Rxns. 1.6 & 1.7) is the primary HO_x production pathway from water (Minschwaner et al., 2011)

$$O_3 + h\nu_{\lambda<320\ \mathrm{nm}} \rightarrow O_2 + O(^1D) \tag{1.6}$$

$$O(^1D) + H_2O \rightarrow 2\,OH. \tag{1.7}$$

The hydroxyl radicals generated can enter the HO_x catalytic cycle, which proceeds to influence stratospheric ozone chemistry either independently or in concert with other cycles.

1.2.3 HO_x Catalytic Cycle

The odd hydrogen family, termed HO_x, is the chemical family comprising atomic hydrogen (H), the hydroxyl radical (OH) and the hydroperoxyl radical (HO_2). Due to the rapid interconversion of these species they can be treated as a single chemical family that is partitioned based on the local environment.

The hydroxyl radical directly catalyzes ozone loss in the stratosphere through the

following catalytic cycles:

$$\mathrm{OH} + \mathrm{O_3} \rightarrow \mathrm{HO_2} + \mathrm{O_2} \tag{1.8}$$

$$\mathrm{HO_2} + \mathrm{O_3} \rightarrow \mathrm{OH} + 2\,\mathrm{O_2} \tag{1.9}$$

$$\text{NET}: \quad 2\,\mathrm{O_3} \rightarrow 3\,\mathrm{O_2}$$

and

$$\mathrm{OH} + \mathrm{O_3} \rightarrow \mathrm{HO_2} + \mathrm{O_2} \tag{1.10}$$

$$\mathrm{HO_2} + \mathrm{O} \rightarrow \mathrm{OH} + 2\,\mathrm{O_2} \tag{1.11}$$

$$\text{NET}: \quad \mathrm{O_3} + \mathrm{O} \rightarrow 2\,\mathrm{O_2}.$$

The HO_x catalytic cycle involving Rxns. 1.8 & 1.9 dominates in the lower stratosphere at altitudes below 30 km. In the upper stratosphere the second cycle becomes important as the increase in the concentration of atomic oxygen makes Rxn. 1.11 more favorable. While additional catalytic cycles involving HO_x are known, these are shown to illustrate how increased water in the stratosphere can lead to an increase in the hydroxyl radical which is directly involved in reactions that destroy stratospheric ozone. The response of ozone loss to increased stratospheric humidity is dependent on altitude, latitude, and temperature, since HO_x is coupled to other catalytic cycles.

1.2.4 Catalytic Coupling of HO_x

The issue of predicting how an increase in stratospheric water vapor will impact ozone is not alone limited to understanding HO_x chemistry in stratosphere. The HO_x catalytic cycle is not isolated and directly interacts with other catalytic cycles. This interaction results in the partitioning of reactive and reservoir species which, too, are directly involved in regulating stratospheric ozone concentrations.

The HO_x cycle directly interacts with NO_x through the reaction:

$$OH + NO_2 + M \rightarrow HNO_3 + M. \tag{1.12}$$

NO_x catalytically destroys ozone through a cycle analogous to that of HO_x (Rxns. 1.10 – 1.11). However, the coupling of the HO_x and NO_x cycles effectively removes OH and NO_2 radicals by converting them to a more stable reservoir species.

OH can influence the partitioning of chlorine between reservoir and reactive species through activation:

$$OH + HCl \rightarrow H_2O + Cl. \tag{1.13}$$

In the lower stratosphere this liberated chlorine can speed up ozone loss through the

following catalytic cycle (Dvortsov and Solomon, 2001):

$$\mathrm{Cl} + \mathrm{O_3} \rightarrow \mathrm{O_2} + \mathrm{ClO} \tag{1.14}$$

$$\mathrm{ClO} + \mathrm{HO_2} \rightarrow \mathrm{O_2} + \mathrm{HOCl} \tag{1.15}$$

$$\mathrm{HOCl} + h\nu \rightarrow \mathrm{OH} + \mathrm{Cl} \tag{1.16}$$

$$\mathrm{O_3} + \mathrm{OH} \rightarrow \mathrm{HO_2} + \mathrm{O_2} \tag{1.17}$$

$$\text{NET}: \quad 2\,\mathrm{O_3} \rightarrow 3\,\mathrm{O_2}$$

1.2.5 Influence of Water on Heterogenous Chemistry

The observation of optically thin subvisible cirrus above the meteorological tropopause in the midlatitudes (e.g., Sassen, 1991; Ansmann et al., 1993) raised the question as to whether heterogenous chemistry could help explain the observed shape of ozone depletion profiles which proved problematic, particularly at midlatitudes, for models to simulate. Solomon et al. (1997) proposed that increases in stratospheric water vapor would enhance midlatitude ozone destruction through heterogenous chemistry that proceeds through the same reactions as occurring at the poles;

the key reactions that proceed with substantive efficiency include:

$$\mathrm{HCl} + \mathrm{ClONO_2} \rightarrow \mathrm{Cl_2} + \mathrm{HNO_3} \tag{1.18}$$

$$\mathrm{HCl} + \mathrm{HOCl} \rightarrow \mathrm{Cl_2} + \mathrm{H_2O} \tag{1.19}$$

$$\mathrm{ClONO_2} + \mathrm{H_2O} \rightarrow \mathrm{HOCl} + \mathrm{HNO_3} \tag{1.20}$$

$$\mathrm{HCl} + \mathrm{HOBr} \rightarrow \mathrm{BrCl} + \mathrm{H_2O} \tag{1.21}$$

Catalytic ozone loss in the midlatitude lower stratosphere is controlled by a combination of cycles involving free radicals, each of which has a rate-limiting species (Wennberg et al., 1994; Stimpfle et al., 1999). Chlorine monoxide (ClO) is the rate-limiting radical in halogen-catalyzed ozone loss and thus the mechanism proposed by Solomon et al. (1997) to explain midlatitude ozone observations centers on whether ClO could be enhanced to such levels as to make photochemical loss rates of ozone comparable to its rate of transport. Smith et al. (2001) found that heterogenous chemistry was unlikely based on in situ observations from aircraft flights of water vapor and ClO in the midlatitude lower stratosphere over the period 1995–1997: the stratosphere is extremely dry and there is no evidence of ice saturation above 500 m of the local tropopause; and there are no observations of large enhancements in ClO ($\geq$ 10 pptv), as necessitated by this heterogenous activation mechanism, that are outside of the instrumental detection limit ($\sim$ 1 pptv) in the lower stratosphere.

At the poles, the temperatures of the winter/spring vortex are sufficiently cold to allow the formation of polar stratospheric clouds (PSCs), despite the low water vapor mixing ratio in the stratosphere. The formation of PSCs leads to heterogenous

activation of halogen radicals and substantial ozone loss. Kirk-Davidoff et al. (1999) investigated the influence that changes in forcing, from a doubled CO_2 scenario, would have on the rate of Arctic ozone loss by evaluating how the temperature of the Arctic vortex and the threshold temperature for PSC formation would change in response to changes in surface temperature. These two quantities, the Arctic vortex temperature and the threshold temperature for PSC formation, serve as a predictor of ozone loss as they relate to efficiency of heterogenous activation through the product of aerosol surface area and reaction probability per collision. The analysis found that Arctic ozone loss would increase under the new climate scenario and would be driven primarily ($\sim$ 90 %) by the radiative effects of increased water vapor, leading to a decrease in the temperature of the vortex. The remainder of the loss comes from the direct chemical contribution of increased water towards an increased efficiency of heterogenous activation.

The observations that serve as the basis of the Smith et al. (2001) response to the mechanism proposed by Solomon et al. (1997) are consistent with the low mixing ratios of the background stratosphere. However, high mixing ratios of water have been observed in the stratosphere that directly result from the convective injection of ice (e.g., Corti et al., 2008; Hanisco et al., 2007). Yet, the simultaneous measurement of the key radical species controlling ozone loss in the lower stratosphere have not been made under such conditions. Results from the Kirk-Davidoff et al. (1999) analysis can be extended to the warmer temperatures of the midlatitude stratosphere and highlights the fact that heterogenous activation can still proceed with sufficient efficiency under scenarios where the mixing ratio of stratospheric water is elevated by

convection. Determining the influence that convection has on the overall temperature structure of the stratosphere remains a goal aided by quantifying the contribution of different water transport pathways to the water budget of the stratosphere.

1.3 Transport and the Control of Stratospheric Humidity

Ever since Brewer's surprising discovery of the aridity of the mid-latitude stratosphere made during the midst of the Second World War, various mechanisms that describe the transport of air and water into the stratosphere have been proposed. The fact that the midlatitude stratospheric frost-point temperature ($\sim$ 190 K) was depressed well below the local cold-point tropopause temperature ($\sim$ 220 K) led Brewer (1949) to ask as to how "the great dryness of the air only one or two km above the tropopause of southern England [is] maintained?" To which he answered:

> Two methods can be suggested *(a)* there is photo-chemical destruction of water or *(b)* by the advection of stratosphere air from the equator where the tropopause temperature is sufficiently low to condense the water out...

The notion of photochemical destruction being a major sink was quickly dismissed leaving large-scale ascent of air through the tropical tropopause as the mechanism responsible for setting the entry value of water vapor into the stratosphere.

In fact, transport of air into the stratosphere being confined to the Equatorial latitudes had been suggested two decades earlier by Dobson, Harrison, and Lawrence

(1929) to explain the latitudinal distribution of ozone and maintain consistency with the theory of photochemical production of ozone:

> The only way in which we can reconcile the observed high ozone concentration in the Arctic in spring and the low concentration in the tropics, with the hypothesis that the ozone is formed by the action of the sunlight, would be to suppose a general slow poleward drift in the highest atmosphere with a slow descent of air near the poles. Such a current would carry the ozone formed in low latitudes to the poles and concentrate it there. If this were the case the ozone at the poles would be distributed through a moderate depth of atmosphere while that in low latitudes would all be high up.

It was not until the 1950's when observations of total column ozone abundances became available that this mechanism of a global scale troposphere-stratosphere overturning was firmly established (Dobson, 1956) and came to be known as the "Brewer-Dobson circulation."

1.3.1 Transport & Dehydration Mechanisms

The flux of water into the stratosphere is controlled by dynamical processes in the troposphere. The following is a brief overview of proposed mechanisms that build upon the concept set forth by Brewer to explain observations of the water vapor distribution in the stratosphere.

1.3.1.1 Tropical Cold Trap

The cold-point temperature of the tropical tropopause sets the water vapor minimum, as described by Brewer (1949). As the tropical tropopause reflects the coldest temperatures that air will encounter, it effectively acts as a "cold trap." Changes in

the global mean tropical tropopause temperature would be expected to manifest as a change in the water vapor concentration in the lower stratosphere. Observations of thin and sub-visible cirrus near the tropopause suggest that uplift is common (e.g., Winker and Trepte, 1998; Lawson et al., 2008), however the absence of a thick and persistent cirrus deck at the tropical tropopause argues against uniform, steady uplift (Robinson, 1980).

1.3.1.2 Quasi-Stationary Disturbances or Propagating Waves

Synoptic- and mesoscale systems lift the stratosphere, inducing a cooling (Fritsch and Brown, 1982) which leads to in situ dehydration. On faster timescales, buoyancy waves near the tropopause (Potter and Holton, 1995) lift air masses, perhaps repeatedly, to induce cooling and dehydration and leading to a decrease in the HDO/H_2O ratio.

1.3.1.3 Stratospheric Fountain

A mechanism primarily proposed by Newell and Gould-Stewart (1981) which constrains the majority of transport of air into the stratosphere to "cold pools" in order to reconcile 100 mbar monthly mean temperatures with stratospheric water mixing ratios. These cold pools are found over the western tropical Pacific and the Indonesian archipelago between November – March and over the Bay of Bengal and Indian sub-continent during the Monsoon. Reexamination of the issue has left much room for debate as to whether spatial confinement of convection is a requirement to explain observations (e.g., Dessler, 1998; Kar et al., 2002) and, if so, the exact

location of the tropopause cold pools (e.g., Pommereau and Held, 2007).

1.3.1.4 Convective Dehydration

Convective events that penetrate into the stratosphere are rare (e.g., Folkins et al., 1999), so it must be dehydration processes in the upper troposphere which are responsible for setting the entry value of stratospheric water vapor. Dessler and Sherwood (2003) proposed a "convective dehydration" mechanism to reconcile the low water entry values with observations of the vertical invariance in water isotopologue ratios throughout the tropical upper troposphere. In order to maintain a constant isotopologue ratio throughout the upper troposphere, air is dehydrated by mixing with very dry air that detrains from overshooting convection. Dehydration occurs by dilution in such a process and, thus, isotopologue ratios are maintained. Gradual ascent, by contrast, is expected to preferentially deplete the heavy isotopologues leading to a vertical variance in the isotopologue ratio.

1.3.1.5 Lagrangian Trajectories

Holton and Gettelman (2001) suggested that the timescale of horizontal transport is much shorter than vertical transport. This notion decouples the location of entry into the stratosphere from its control on the entry value of water by the local tropopause temperature: the minimum temperature experienced by an air mass determines the entry value which can be thousands of kilometers away from entry. Lagrangian trajectory models (e.g., Bonazzola and Haynes, 2004; Fueglistaler et al., 2004) investigate such a transport mechanisms by calculating the back-trajectory

of air masses that reach the stratosphere using wind and temperature fields. This transport model captures the observed seasonal and interannual trends in stratospheric water variability, yet the interannual anomalies in stratospheric water vapor are dominated by anomalies in the zonal mean temperature rather than changes in transport or localized temperature anomalies (Fueglistaler and Haynes, 2005).

1.3.2 UT/LS Trends & Convective Pathways

While the mean temperature of the tropical tropopause may play a dominant role in controlling the amount of water which enters the stratosphere, it is not the only mechanism at play. There is some indication that stratospheric water vapor concentrations are increasing (Oltmans et al., 2000; Rosenlof et al., 2001) despite decreasing temperatures at the tropical tropopause (Seidel et al., 2001; Zhou et al., 2001). This apparent paradox implies the existence of mechanisms which are largely insensitive to the temperature of the tropical tropopause.

Despite the fact that the frequency of convection decreases with altitude in the UT/LS, convective lofting of ice is a mechanism which can deliver water to the stratosphere and bypasses the constraint on the maximum water vapor mixing ratio set by the cold point tropopause. Models estimate a convective contribution of approximately 0.5 ppmv of water vapor to regions of the stratosphere above the 380 K isentropic surface (e.g., Liu et al., 2010; Grosvenor et al., 2007). Convective processes operate on much faster timescales than large-scale, gradual ascent and it is expected that the chemical signature of air that enters will differ. The response of water pathways to alternate forcing scenarios is to some extent directly linked to

climate through the temperature of the cold-point tropopause, which sets the water vapor minimum of an air mass during large-scale, gradual ascent; but, at the same time, convective pathways represent a wildcard in terms of the stratospheric water vapor response to changes in climate.

It is difficult to conclusively state the existence of a long-term trend in stratospheric water vapor. Significant disagreement exists between models and observations of water vapor at 80 hPa (Gettelman et al., 2010), as well as between the observed and modeled trend in tropical tropopause temperatures (Gettelman et al., 2009). In fact, the discrepancies between models and observations led the WMO (2011) to state in its assessment report on stratospheric ozone and related processes that "we cannot provide any reliable prediction as to what the future evolution of stratospheric water vapor will be in a climate with increasing greenhouse gas concentrations."

Given the influence that stratospheric water vapor has on ozone chemistry (Sec. 1.2) and the large uncertainties in understanding the processes which determine its concentration, it is prudent that this uncertainty is minimized. The response of convective and slow-ascent pathways may differ to changes in forcing as they are driven by different mechanisms. Accurate forecasts of future climate-chemistry scenarios require a greater and more complete understanding of water transport pathways.

1.3.3 Tropical Transition Layer

Historically atmospheric layers have been defined in terms of their temperature structure, the troposphere exhibiting a positive lapse rate (decreasing temperature with altitude) and an inversion in lapse rate defining the stratosphere. The tropopause being the "cold point" where the minimum temperature is experienced and the temperature inversion occurs. It is formally defined by the WMO as the lowest level at which the lapse rate decreases to 2 K km^{-1} or less and the lapse rate averaged between this level and any level within the next 2 km does not exceed 2 K km^{-1}. While this thermal definition may be suitable in describing an atmosphere where tropospheric and stratospheric process are largely independent of one another, it does not reflect observations of the region between the troposphere and stratosphere where characteristics that are classically attributed to each layer can actually coexist over vertical scales that extend several kilometers. As such, this transition region has been termed the tropical transition layer (TTL).

There are many definitions of the TTL in the literature but they encompass the same general concept. With that in mind, the TTL is loosely defined here as a region in the tropical atmosphere between 12–20 km or, alternatively, 340–450 K (θ). Of importance is that this transition region includes both the level of zero net radiative heating (LZRH; 355 K, 150 hPa, 14 km) and the level where highest convection reaches (420–450 K, 70 hPa, 18–20 km) (Sherwood and Dessler, 2000).

The TTL is of interest not only because it serves as the transition region between two atmospheric layers but also because it is the region where the atmospheric fate of transported water and very short-lived species (VSLS) is decided and is therefore

referred to as the "gate to the stratosphere" (Fueglistaler et al., 2009). Above the LZRH air will rise under the influence of diabatic heating despite a negative vertical temperature gradient until the cold point tropopause. Under such conditions the air is expected to remain near saturation as it rises, so that the TTL is characterized as a region of high relative humidity.

1.4 Atmospheric Iodine Chemistry

1.4.1 Impact on Stratospheric Ozone

Iodine loading and its potential impact on stratospheric ozone was first proposed by Solomon et al. (1994b) in an attempt to reconcile non-polar ozone losses that proved difficult to explain by considering only local chlorine and bromine chemistry. The atmospheric lifetime of iodocarbons is very short, on the order of days to weeks, in the troposphere, owing to the lability of the iodine-carbon bond to photolytic cleavage. Despite this short atmospheric lifetime, observations of typically short-lived, insoluble tropospheric species in the upper troposphere and lower stratosphere (e.g., ^{222}Rn, NO_x, and hydrocarbons) make rapid convective pumping of iodocarbons into the stratosphere a possibility and set the basis for the proposed stratospheric iodine cycles.

It was suggested that concentrations of iodine monoxide (IO) as low as 1 pptv or fast coupled halogen kinetics ($k_{XO+IO} \approx 1 \times 10^{-10}$ cm^3 molecule^{-1} s^{-1}) could help explain some of the observed ozone levels in the lower stratosphere through coupled

halogen reactions (Solomon et al., 1994a):

$$\mathrm{X} + \mathrm{O_3} \rightarrow \mathrm{XO} + \mathrm{O_2} \tag{1.22}$$

$$\mathrm{I} + \mathrm{O_3} \rightarrow \mathrm{IO} + \mathrm{O_2} \tag{1.23}$$

$$\mathrm{XO} + \mathrm{IO} \rightarrow \mathrm{X} + \mathrm{I} + \mathrm{O_2} \tag{1.24a}$$

$$\rightarrow \mathrm{XOO} + \mathrm{I} \tag{1.24b}$$

$$\rightarrow \mathrm{IX} + \mathrm{O_2} \tag{1.24c}$$

$$\text{NET}: \quad 2\,\mathrm{O_3} \rightarrow 3\,\mathrm{O_2} \tag{1.25}$$

where X = (Cl or Br) and the alternate products in Rxns. 1.24b & 1.24c quickly decompose to regenerate the initial atomic halogens. This cycle is analogous to the synergistic coupling between bromine and chlorine suggested by McElroy et al. (1986) to account for the rapid loss of stratospheric ozone in the Antarctic spring that could not be accounted for by chlorine chemistry alone.

Laboratory studies have shown that the rates of coupling between IO and the halogen oxide family (Rxn. 1.24a) are slower than proposed by Solomon et al. (1994b): $k_{\mathrm{ClO+IO}} = (5.1 \pm 1.0) \times 10^{-12} \exp\left[(280 \pm 150)/T\right]$ cm^3 molecule^{-1} s^{-1} (Turnipseed et al., 1997) and $k_{\mathrm{BrO+IO}} = (6-10) \times 10^{-11}$ cm^3 molecule^{-1} s^{-1} (Laszlo et al., 1997; Gilles et al., 1997) for ClO and BrO, respectively.

Several remote measurements of IO in the lower stratosphere have been made. These are summarized in Table 1.1 and are typically found to be below 1 pptv. Considering the laboratory studies and remote measurements of IO, the current

Table 1.1: Remote Measurements of Stratospheric IO

$[IO]_{max.}$ (pptv)	Method†	Comments	Ref.
0.10–0.25	DOAS (b)	20 km; 43–68 °N	Bösch et al. (2003)
0.68–0.8 (±0.2)	DOAS (g)	79 °N	Wittrock et al. (2000)
0.2	SAOZ (b)	20 km; 44–70 °N	Pundt et al. (1998)
0.2 (+0.3/−0.2)	FTS (g)	32 °N	Wennberg et al. (1997)

† (g) ground-based; (b) balloon-borne

estimates for the ozone removal efficiency of iodine is between 150–300 times that of chlorine—less than the 1000 efficiency factor given to iodine by Solomon et al. (1994b). However large uncertainties still remain because of limited knowledge about OIO and heterogenous iodine chemistry.

Recent kinetics data suggest that the rate of reaction between IO and HO_2 is substantially faster (Maguin et al., 1992; Canosa-mas et al., 1999; Knight and Crowley, 2001) than used in the analysis by Solomon et al. (1994b). This highlights the increased importance of ozone loss that is placed on HO_x cycles (UNEP, 2008) and the potential coupling between short-lived halogen species and water transport pathways from deep convection.

1.4.1.1 Convective Transport

Iodine is primarily sourced biogenically and estimates of the annual production of precursors suggest that it eclipses the anthropogenic production of chlorine and bromine precursors. It follows that since the lifetime of inorganic iodine precursors is short, which themselves are largely organic, there should be substantially more iodine in the troposphere than the stratosphere. The dominant iodine source is methyl iodide, where its annual emission rate is estimated as 550 Gg I yr^{-1}, with

nearly equal open ocean and coastal source terms (Butler et al., 2007).

Tropical overshooting convection can inject surface air directly into the TTL and lower stratosphere. Injection of air into this region has been observed (Ricaud et al., 2007) and is simulated by convective transport models (Donner et al., 2007; James et al., 2008). The low solubility of methyl iodide and the decreasing probability of washout with height make transport via this pathway a possibility.

Transport simulations of methyl iodide using data from TC4 and Pre-AVE (Aschmann et al., 2009) and by Bell et al. (2002) suggest that the concentration of iodine is on the order of 0.1 pptv at the base of the TTL and falls of to 0.05 pptv at the cold point tropopause. Other iodocarbons may be important on local scales (Carpenter et al., 1999), but they are excluded from global assessments and transport to the UT/LS due to their short lifetimes. The deepest stratospheric injections are produced by high instability and breaking of gravity waves excited by strong convection inside super-cell thunderstorms; stratospheric water vapor enhancements have been observed to occur by this mechanism but no studies relating to the transport of short-lived species have been published (UNEP, 2008).

1.4.2 Tropospheric Processes

1.4.2.1 IO and Ozone Chemistry in the MBL

Iodine monoxide is involved in ozone destruction in the marine boundary layer. Observations of methyl iodide in the middle and upper free troposphere during the NASA Pacific Exploratory Mission in the western Pacific led to an analysis of the potential impact of iodine on tropospheric ozone (Davis et al., 1996). Ozone and

the free radicals generated by its photolysis are responsible for defining the oxidative capacity of the troposphere: a low-temperature flame that cleanses the atmosphere.

Davis et al. (1996) investigated the impact of various mixing ratios of inorganic iodine I_x ($I_x = I + IO + HI + HOI + 2\,I_2O_2 + INO_x$) that could result from differing emissions scenarios and found that total column O_3 destruction was meaningful when tropospheric iodine exceeded 1 pptv. The primary reactions controlling iodine in the troposphere were identified by Davis et al. (1996) as

$$2\,(I + O_3 \rightarrow IO + O_2) \tag{1.26}$$

$$IO + IO \rightarrow 2\,I + O_2 \tag{1.27}$$

$$\text{NET}: \quad 2\,O_3 \;\rightarrow\; 3\,O_2 \tag{1.28}$$

and

$$I + O_3 \rightarrow IO + O_2 \tag{1.29}$$

$$IO + HO_2 \rightarrow HOI + O_2 \tag{1.30}$$

$$HOI + h\nu \rightarrow I + OH \tag{1.31}$$

$$\text{NET}: \quad O_3 + HO_2 \;\rightarrow\; 2\,O_2 + OH \tag{1.32}$$

with the rate-limiting step in both reactions involving IO. This differs from the stratospheric pathway described by Solomon et al. (1994b) (Rxns. 1.22 – 1.25), a result of less chlorine and bromine in the troposphere.

The coupling of IO and HO_2 affects the partitioning of the HO_x family and influences the oxidative capacity of the atmosphere. Calculations constrained by observations during the North Atlantic Marine Boundary Layer Experiment (NAMBLEX) suggest that under low NO_x (NO $<$ 50 pptv) conditions the IO + HO_2 reaction accounts for up to 40 % of the HO_2 sink, and 15 % of the total daytime production of OH is produced by the subsequent photolysis of HOI (Bloss et al., 2005). The role of iodine in tropospheric ozone loss and aerosol formation is not an unrelated issue since a primary loss pathway for iodine in the troposphere is polymerization to form particles.

1.4.2.2 Atmospheric Mercury Deposition

The dominant form of mercury in the atmosphere is gaseous elemental mercury (Hg^0; GEM) with a lifetime on the order of 1–2 years (Schroeder and Munthe, 1998). This long lifetime makes atmospheric mercury a global-scale problem despite the fact that the vast majority of anthropogenic mercury is emitted into the atmosphere as point sources from coal-fired power generation, metal smelting and waste incineration (Pacyna et al., 2006; Streets et al., 2005). Current atmospheric concentrations of mercury are 3 times higher than preindustrial values (Mason et al., 1994) and this can largely by attributed to the anthropogenic source term.

Observations of rapid mercury depletion from the atmospheric boundary layer during the Arctic spring of 1998 that were correlated with ozone depletion events were the first suggestion that the Arctic environment could be a sink for atmospheric mercury (Schroeder and Munthe, 1998) and it has come to be understood that this is

an annual recurring springtime phenomenon (Steffen et al., 2005). Indeed, estimates place the magnitude of the Arctic sink at 325 tons yr^{-1} (Ariya et al., 2004)—the Arctic bears a sizable burden of the approximately 6000 tons of mercury present in the atmosphere on an annual basis (UNEP, 2008).

Mercury depletion events are driven by the oxidation of gaseous elemental mercury into reactive gaseous mercury (Hg^{2+} or Hg^{+}; RGM). This reactive form is more hygroscopic than elemental mercury and is readily deposited on aerosol or ice so that it can potentially be assimilated into the food chain upon snowmelt (Ariya et al., 2004). Inorganic Hg^{2+} can by methylated, forming very toxic methyl mercury which can be biomagnified and enter the human food chain (AMAP, 1998).

While the chemistry of atmospheric mercury depletion events is still poorly understood, the similar temporal evolution of these events with ozone depletion events (Schroeder and Munthe, 1998) and the large observed increases in springtime BrO columns from satellites (Richter et al., 1998; Mueller et al., 2002) have led to the suggestion that photochemical halogen, and bromine in particular, cycles are responsible. Calvert and Lindberg (2004a) found that modeled Br-BrO chemistry can account for the homogenous component of observed chemistry involving ozone, mercury and halogens. A companion study (Calvert and Lindberg, 2004b) found that iodine reactions with mercury are unimportant, since the decay of HgI is rapid, but that IO radicals interact with BrO and ClO radicals to enhance Br-atom concentrations and increase the rate of bromine-mercury reactions.

Strong emphasis has been placed on mercury depletion events in the Arctic, however, similar seasonal loss of ozone and mercury have also been observed in the

Antarctic (Ebinghaus et al., 2002; Brooks et al., 2008). Similar halogen chemistry is thought to responsible for initiating these episodes. Unlike the Arctic, the Antarctic marine boundary layer is known to exhibit elevated levels of iodine in the spring. The first measurements of IO in the Antarctic troposphere were made in 2001 (Frieß et al., 2001) with a DOAS instrument, and an IO mixing ratio in the marine boundary layer of up to 10 pptv was reported. This large concentration of IO was attributed to the photolytic destruction of methylated iodine produced by biological activity in the ocean. Chance et al. (2010) found that the large summertime algal blooms were accompanied by the accumulation of iodide in coastal Antarctica. Recent MAX-DOAS measurements of IO in the Antarctic snowpack suggest concentrations as high as 50 ppbv in the interstitial air (Frieß et al., 2010). Transport pathways of iodine to the snowpack from the coast are still speculative. Interaction between IO and BrO is expected to lead to an amplification of ozone destruction in the spring, which in turn raises the question as to the role of the Antarctic as a sink in the global mercury cycle.

There is little uncertainty that mercury emissions will continue to increase in the near future as a result of human activity. Coal and fossil fuel usage is predicted to increase 350 % by 2020, relative to 1990 levels, in Asia alone (van Aardenne et al., 1999). Changes in timing and extent of sea ice cover, which is already occurring, make it difficult to project the magnitude of the polar mercury sink under such a scenario since the mechanism by which halogen ions in the ocean interact with sea ice to be liberated into the atmosphere is still poorly understood.

1.5 Aerosols

Aerosols have played a role in several seminal works of physical science, including the determination of electron charge (Millikan, 1913) and the discovery of the positron (Anderson, 1933). Aerosols themselves have become the focus of a great deal of research since the 1970's when environmental awareness and the health effects of air pollution became priorities (Hinds, 1999).

Atmospheric aerosols are known to influence the radiative properties of the atmosphere, but the magnitude of their impact is obscured by large uncertainties. Aerosols can influence atmospheric radiation directly, largely by scattering incoming solar radiation and thereby acting as a cooling agent, or indirectly by modifying microphysical properties that dictate the behavior of clouds. Some of these indirect effects include increases in reflection of solar radiation from clouds, increased cloud height and increased cloud lifetime, all of which influence atmospheric radiation. It is primarily through the indirect effect that the large uncertainties in aerosol radiative forcing arise because of the difficulty in evaluating the chain of processes which link aerosol source gases to cloud albedo.

The main source of biogenic aerosols is either sulfate, formed from oceanic dimethyl sulfide, or organic, formed from the oxidation of non-methane hydrocarbons produced by terrestrial vegetation. Both of these sources are susceptible to changes in climate and chemistry.

1.5.1 Iodine Monoxide as Aerosol Precursor

The processes that control formation of particles in the marine environment are largely undetermined (Capaldo et al., 1999; Katoshevski et al., 1999) however it has been suggested that biogenic iodine may serve as a key component to the formation of aerosols in this environment. A smog chamber study by O'Dowd et al. (2002) studying the photolysis of CH_2I_2 found that the introduction of UV-radiation to a chamber containing CH_2I_2 and O_3 led to rapid homogenous nucleation and was followed by condensation and coagulation growth. No aerosol growth was observed if any of the three components (CH_2I_2, O_3, or UV-radiation) was absent.

Rapid photolysis of CH_2I_2 leads to production of atomic iodine, which in the presence of ozone forms IO. Iodine monoxide is the central species in the aerosol formation mechanism proposed by O'Dowd et al. (2002) where it undergoes self-polymerization or oxidation by HO_2 to form products I_2O_2, OIO or HOI, which undergo uptake to the aerosol phase. Additionally, the products I_2 and I_2O can be formed by IO reactions, and while they do not undergo direct aerosol uptake, can be converted to HOI by subsequent reactions. The contribution of each pathway to aerosol formation is dependent on the CH_2I_2 precursor concentration: at low concentrations (20 – 200 pptv) representative of coastal conditions the HOI pathway is dominant.

Saunders et al. (2010) found in a laboratory setting that IO and OIO form higher oxides I_2O_3 and I_2O_4 which subsequently polymerize and grow ultrafine particles. The study found that particulate iodine oxides could be formed without the addition of ozone; yet, this is not inconsistent with mechanisms proposed by O'Dowd et al.

(2002) where ozone was required, since ozone served as the oxidant for atomic iodine and was absent from later stage reactions. Saunders et al. (2010) were able to generate IO via the $O(^3P)$ + I reaction, where $O(^3P)$ was generated by photolysis of N_2O with an excimer laser, and were able to directly assess the impact of ozone on growth.

An understanding of the full chemical mechanism responsible for forming aerosols from iodine is incomplete, however the presence of IO as a precursor to particle formation is consistent.

Aerosols have important microphysical effects, particularly in pristine marine environments, where the increase in cloud condensation nuclei that result from the aerosol loading have been shown to slow the conversion of cloud drops into raindrops (Gunn and Phillips, 1957; Squires, 1958). This effectively shut downs precipitation from shallow and short-live clouds (Radke et al., 1989) and thereby influences both the radiative and heat structure of the troposphere (Rosenfeld et al., 2008).

1.6 Thesis Overview

The breadth of scientific questions that are spawned by the current state of understanding of ozone chemistry, aerosols and halogen chemistry, requires a multifaceted approach, fed by both observations and models, to be answered. In no certain manner can the body of work presented here be considered as directly contributing to each topic; although, the opposite is not necessarily true, as each of the topics presented serves to motivate the development of the instruments discussed within. What

follows must be considered an exploration of a subset of the body of knowledge that makes up halogen/ozone chemistry, chemical coupling and transport processes.

The entry of water into the stratosphere can proceed by two unique mechanisms: convection and large-scale ascent. The time scale of large-scale ascent subjects air that is transported by this mechanism to thermodynamic equilibrium—the mixing ratio of water in the air parcel is maintained at saturation. Conversely, convection rapidly transports air and the strong updraft velocities associated with it are also capable of transporting ice. The differing thermodynamic histories associated with these two process places water isotope measurements in a unique position to discriminate between them and, more importantly, to quantify the stratospheric contribution of each process. Such quantitative understanding is required to accurately predict how stratospheric water vapor will respond to forcing changes.

To this end, water isotope measurements in the TTL can assess the relative importance of the two transport pathways in troposphere-stratosphere exchange in the tropics. However, convection can directly influence the radiative properties of the TTL through ice lofting and the subsequent formation of cirrus clouds. Aircraft measurements of water vapor and ice isotopes during the TC4 mission served as a means to sample the outflow of active convection and the basis to evaluate how convection contributes to the water budget of the TTL.

The coupling between water and halogens, and the potential enhancement of these two species by convection, places a priority on their simultaneous measurement under such conditions. The need to accurately measure the iodine contribution in the stratosphere provided the initial motivation and constraints for the development

of an instrumental technique. While a flight system was not developed initially, investigating the role of iodine in the midlatitude marine boundary layer serves both as a testbed for validation of the prototype IO LIF instrument and as scientific motivation to deploy the instrument into the field.

In the midlatitude marine environment, ozone destruction and aerosol formation are the primary processes surrounding biogenic iodine. In the polar regions, the springtime bromine bloom makes halogen chemistry a public health issue since mercury is subsequently oxidized to a toxic form available for uptake and bioaccumulation. While bromine is primarily responsible for mercury depletion events, the potential amplification of bromine by iodine coupling motivates iodine monoxide measurements at high latitudes. The unique capabilities of the IO instrument as it was designed, which include a weatherproof enclosure, self-sufficiency, portability and ease of transport to source sites, mean that the instrument could be minimally modified to make measurements at the poles.

Abstractly, the motivation for a glyoxal measurement parallels that of midlatitude IO, where oxidation chemistry and aerosol formation are the dominant processes in forests. Yet, the precursors and specific details of chemical processes differ between the two environments. The flexibility of the sensitivity and specificity that are afforded by the techniques and components utilized in the IO instrument are demonstrated in the development of the glyoxal instrument.

If the motivation and interrelatedness of the research topics that make up the chapters of this thesis seem tenuous then that is only a signal of how science is done. While I have made it my goal to show the connectedness of what at times may

seem to be three seemingly unrelated topics (global and mesoscale water transport pathways, marine halogen chemistry, oxidation chemistry of biogenic organics), an understanding of what could be conceived of as largely independent topics is itself essential to understanding the Earth and climate as a system. Some of these research areas can be taken to be wholly independent, while others are tightly coupled, but all fit into our current understanding of this system.

In fact, one need only look at the history of assessment reports by the IPCC, which by their own account, reveal the incremental understanding of the body of knowledge of climate and its change. An illustration of this is the physics that is incorporated into climate models: models including only CO_2 and rain processes in the mid-1970s have grown to include land, oceans, ice, clouds, volcanic activity, aerosols, carbon cycles, rivers, chemistry, dynamical processes, and interactive vegetation. For each component of this system a comprehensive array of observations and models is required to understand how the dynamical behavior of one component ultimately affects all the others.

The contents of this thesis are made up of chapters detailing the development and results from several different *in situ* instruments. Chapter 2 describes the constraints set upon and the detection technique used in two water isotopologue instruments deployed aboard the NASA WB-57F high-altitude research aircraft. Chapter 3 investigates the role of water isotopologues in transport pathways and details observations of the isotopic composition of ice detrained from deep tropical convection during the TC4 field mission. The majority of Chapter 3 forms the basis of a paper to be submitted for publication:

> O'Brien, A., T. F. Hanisco, D. S. Sayres, J. M. St. Clair, J. B. Smith, E. M. Weinstock, and J. G. Anderson (2011), Measurements of the isotopic composition of ice and vapor above a tropical convective system, *Journal of Geophysical Research* (to be submitted).

Chapter 4 details the development of a laser-induced phosphorescence instrument and results from the CABINEX field campaign. Many of the subsystems (e.g., White cell, cavity ringdown, data acquisition) are similar to those of the iodine monoxide laser-induced fluorescence instrument, described in Chapter 5, and are discussed in detail only upon first introduction. Preliminary results and engineering data from field deployments with the iodine monoxide instrument are discussed in Chapter 5. Chapter 6 provides some concluding remarks and open questions that the instruments described here can help to resolve.

References

AMAP. *AMAP Assessment Report: Arctic Pollution Issues*. Arctic Monitoring and Assessment Programme, Oslo, Norway, 1998.

C. D. Anderson. The Positive Electron. *Physical Review*, 43:491–494, Mar. 1933. doi: 10.1103/PhysRev.43.491.

A. Ansmann, J. Bösenberg, G. Brogniez, S. Elouragini, P. H. Flamant, K. Klapheck, H. Linn, L. Menenger, W. Michaelis, M. Riebesell, C. Senff, P.-Y. Thro, U. Wandinger, and C. Weitkamp. Lidar Network Observations of Cirrus Morphological and Scattering Properties during the International Cirrus Experiment 1989: The 18 October 1989 Case Study and Statistical Analysis. *Journal of Applied Meteorology*, 32(10):1608–1622, 2011/11/05 1993. doi: 10.1175/1520-0450(1993)032⟨1608:LNOOCM⟩2.0.CO;2.

P. A. Ariya, A. P. Dastoor, M. Amyot, W. H. Schroeder, L. Barrie, K. Anlauf, F. Raofie, A. Ryzhkov, D. Davignon, J. Lalonde, and A. Steffen. The Arctic: a sink for mercury. *Tellus B*, 56:397, Nov. 2004. doi: 10.1111/j.1600-0889.2004.00118.x.

J. Aschmann, B.-M. Sinnhuber, E. L. Atlas, and S. M. Schauffler. Modeling the transport of very short-lived substances into the tropical upper troposphere and lower stratosphere. *Atmospheric Chemistry and Physics*, 9(23):9237–9247, 2009. doi: 10.5194/acp-9-9237-2009.

N. Bell, L. Hsu, D. J. Jacob, M. G. Schultz, D. R. Blake, J. H. Butler, D. B. King, J. M. Lobert, and E. Maier-Reimer. Methyl iodide: Atmospheric budget and use as a tracer of marine convection in global models. *Journal of Geophysical Research*, 107(D17), 09 2002. doi: 10.1029/2001JD001151.

W. J. Bloss, J. D. Lee, G. P. Johnson, R. Sommariva, D. E. Heard, A. Saiz-Lopez, J. M. C. Plane, G. McFiggans, H. Coe, M. Flynn, P. Williams, A. R. Rickard, and Z. L. Fleming. Impact of halogen monoxide chemistry upon boundary layer OH and HO_2 concentrations at a coastal site. *Geophysical Research Letters*, 320: L06814, Mar. 2005. doi: 10.1029/2004GL022084.

M. Bonazzola and P. Haynes. A trajectory-based study of the tropical tropopause region. *Journal of geophysical research*, 109(D20):D20112, 2004.

H. Bösch, C. Camy-Peyret, M. P. Chipperfield, R. Fitzenberger, H. Harder, U. Platt, and K. Pfeilsticker. Upper limits of stratospheric IO and OIO inferred from center-

to-limb-darkening-corrected balloon-borne solar occultation visible spectra: Implications for total gaseous iodine and stratospheric ozone. *Journal of Geophysical Research*, 108:4455, Aug. 2003. doi: 10.1029/2002JD003078.

A. W. Brewer. Evidence for a world circulation provided by the measurements of helium and water vapour distribution in the stratosphere. *Quarterly Journal of the Royal Meteorological Society*, 75:351–363, Oct. 1949. doi: 10.1002/qj.49707532603.

S. Brooks, S. Lindberg, G. Southworth, and R. Arimoto. Springtime atmospheric mercury speciation in the McMurdo, Antarctica coastal region. *Atmospheric Environment*, 42(12):2885–2893, 2008. doi: 10.1016/j.atmosenv.2007.06.038.

J. H. Butler, D. B. King, J. Lobert, S. A. Montzka, S. A. Yvon-Lewis, B. D. Hall, N. J. Warwick, D. J. Mondeel, M. Aydin, and J. W. Elkins. Oceanic distributions and emissions of short-lived halocarbons. *Global Biogeochemical Cycles*, 21(1), 2007. doi: 10.1029/2006GB002732.

M. M. Caldwell, J. F. Bornman, C. L. Ballare, S. D. Flint, and G. Kulandaivelu. Terrestrial ecosystems, increased solar ultraviolet radiation, and interactions with other climate change factors. *Photochemical & Photobiological Sciences*, 6:252–266, 2007. doi: 10.1039/B700019G.

J. G. Calvert and S. E. Lindberg. Potential influence of iodine-containing compounds on the chemistry of the troposphere in the polar spring. I. Ozone depletion. *Atmospheric Environment*, 38(30):5087 – 5104, 2004a. doi: 10.1016/j.atmosenv.2004.05.049.

J. G. Calvert and S. E. Lindberg. The potential influence of iodine-containing compounds on the chemistry of the troposphere in the polar spring. II. Mercury depletion. *Atmospheric Environment*, 38(30):5105 – 5116, 2004b. doi: 10.1016/j.atmosenv.2004.05.050.

C. Canosa-mas, M. Flugge, D. Shah, A. Vipond, and R. Wayne. Kinetics of the Reactions of IO with HO_2 and $O(^3P)$. *Journal of Atmospheric Chemistry*, 34: 153–162, 1999. doi: 10.1023/A:1006262306459.

K. P. Capaldo, P. Kasibhatla, and S. N. Pandis. Is aerosol production within the remote marine boundary layer sufficient to maintain observed concentrations? *Journal of Geophysical Research*, 104:3483–3500, Feb. 1999. doi: 10.1029/1998JD100080.

L. J. Carpenter, W. T. Sturges, S. A. Penkett, P. S. Liss, B. Alicke, K. Hebestreit, and U. Platt. Short-lived alkyl iodides and bromides at Mace Head, Ireland: Links to biogenic sources and halogen oxide production. *Journal of Geophysical Research*, 104:1679–1690, 1999. doi: 10.1029/98JD02746.

A. Cazenave, K. Dominh, S. Guinehut, E. Berthier, W. Llovel, G. Ramillien, M. Ablain, and G. Larnicol. Sea level budget over 2003-2008: A reevaluation from GRACE space gravimetry, satellite altimetry and Argo. *Global and Planetary Change*, 65:83–88, Jan. 2009. doi: 10.1016/j.gloplacha.2008.10.004.

R. Chance, K. Weston, A. R. Baker, C. Hughes, G. Malin, L. Carpenter, M. P. Meredith, A. Clarke, T. D. Jickells, P. Mann, and H. Rossetti. Seasonal and interannual variation of dissolved iodine speciation at a coastal Antarctic site. *Marine Chemistry*, 118(3–4):171–181, 2010. doi: 10.1016/j.marchem.2009.11.009.

J. A. Church and N. J. White. Sea-Level Rise from the Late 19th to the Early 21st Century. *Surveys in Geophysics*, 32:585–602, Sept. 2011. doi: 10.1007/s10712-011-9119-1.

T. Corti, B. Luo, M. De Reus, D. Brunner, F. Cairo, M. Mahoney, G. Martucci, R. Matthey, V. Mitev, F. Dos Santos, et al. Unprecedented evidence for overshooting convection hydrating the tropical stratosphere. *Geophysical Research Letters*, 35, 2008.

D. Davis, J. Crawford, S. Liu, S. McKeen, A. Bandy, D. Thornton, F. Rowland, and D. Blake. Potential impact of iodine on tropospheric levels of ozone and other critical oxidants. *Journal of Geophysical Research*, 101(D1):2135–2147, 1996. doi: 10.1029/95JD02727.

P. N. den Outer, H. Slaper, and R. B. Tax. UV radiation in the Netherlands: Assessing long-term variability and trends in relation to ozone and clouds. *Journal of Geophysical Research (Atmospheres)*, 110:D02203, Jan. 2005. doi: 10.1029/2004JD004824.

A. E. Dessler. A reexamination of the "stratospheric fountain" hypothesis. *Geophysical Research Letters*, 25:4165–4168, 1998. doi: 10.1029/1998GL900120.

A. E. Dessler and S. C. Sherwood. A model of hdo in the tropical tropopause layer. *Atmospheric Chemistry and Physics*, 3(6):2173–2181, 2003. doi: 10.5194/acp-3-2173-2003.

G. M. B. Dobson. Origin and Distribution of the Polyatomic Molecules in the Atmosphere. *Royal Society of London Proceedings Series A*, 236:187–193, Aug. 1956. doi: 10.1098/rspa.1956.0127.

G. M. B. Dobson, D. N. Harrison, and J. Lawrence. Measurements of the Amount of Ozone in the Earth's Atmosphere and Its Relation to Other Geophysical Conditions. Part III. *Royal Society of London Proceedings Series A*, 122:456–486, Feb. 1929.

L. J. Donner, L. W. Horowitz, A. M. Fiore, C. J. Seman, D. R. Blake, and N. J. Blake. Transport of radon-222 and methyl iodide by deep convection in the GFDL Global Atmospheric Model AM2. *Journal of Geophysical Research*, 112(D17), 09 2007. doi: 10.1029/2006JD007548.

V. Dvortsov and S. Solomon. Response of the stratospheric temperatures and ozone to past and future increases in stratospheric humidity. *Journal of Geophysical Research*, 106(D7):7505–7514, 2001.

R. Ebinghaus, H. H. Kock, C. Temme, J. W. Einax, A. G. Löwe, A. Richter, J. P. Burrows, and W. H. Schroeder. Antarctic springtime depletion of atmospheric mercury. *Environmental Science & Technology*, 36(6):1238–1244, 2002. doi: 10.1021/es015710z.

J. R. Fleming. *Historical Perspectives on Climate Change*. Oxford University Press, New York, 1998.

I. Folkins, M. Loewenstein, J. Podolske, S. Oltmans, and M. Proffitt. A barrier to vertical mixing at 14 km in the tropics: Evidence from ozonesondes and aircraft measurements. *Journal of Geophysical Research*, 104(D18):22095–22102, Sept. 1999.

U. Frieß, T. Wagner, I. Pundt, K. Pfeilsticker, and U. Platt. Spectroscopic measurements of tropospheric iodine oxide at Neumayer station, Antarctica. *Geophysical Research Letters*, 28:1941–1944, May 2001. doi: 10.1029/2000GL012784.

U. Frieß, T. Deutschmann, B. S. Gilfedder, R. Weller, and U. Platt. Iodine monoxide in the Antarctic snowpack. *Atmospheric Chemistry & Physics*, 10:2439–2456, Mar. 2010.

J. M. Fritsch and J. M. Brown. On the Generation of Convectively Driven Mesohighs Aloft. *Monthly Weather Review*, 110:1554, 1982. doi: 10.1175/1520-0493(1982)110⟨1554:OTGOCD⟩2.0.CO;2.

S. Fueglistaler and P. Haynes. Control of interannual and longer-term variability of stratospheric water vapor. *Journal of Geophysical Research*, 110:D24108, 2005.

S. Fueglistaler, H. Wernli, and T. Peter. Tropical troposphere-to-stratosphere transport inferred from trajectory calculations. *Journal of Geophysical Research*, 109: 1979–1993, 2004.

S. Fueglistaler, A. E. Dessler, T. J. Dunkerton, I. Folkins, Q. Fu, and P. W. Mote. Tropical tropopause layer. *Reviews of Geophysics*, 47:RG1004, Feb. 2009. doi: 10.1029/2008RG000267.

A. Gettelman, T. Birner, V. Eyring, H. Akiyoshi, S. Bekki, C. Brühl, M. Dameris, D. E. Kinnison, F. Lefevre, F. Lott, E. Mancini, G. Pitari, D. A. Plummer, E. Rozanov, K. Shibata, A. Stenke, H. Struthers, and W. Tian. The Tropical Tropopause Layer 1960-2100. *Atmospheric Chemistry & Physics*, 9:1621–1637, Mar. 2009.

A. Gettelman, M. I. Hegglin, S.-W. Son, J. Kim, M. Fujiwara, T. Birner, S. Kremser, M. Rex, J. A. Añel, H. Akiyoshi, J. Austin, S. Bekki, P. Braesike, C. Brühl, N. Butchart, M. Chipperfield, M. Dameris, S. Dhomse, H. Garny, S. C. Hardiman, P. Jöckel, D. E. Kinnison, J. F. Lamarque, E. Mancini, M. Marchand, M. Michou, O. Morgenstern, S. Pawson, G. Pitari, D. Plummer, J. A. Pyle, E. Rozanov, J. Scinocca, T. G. Shepherd, K. Shibata, D. Smale, H. Teyssèdre, and W. Tian. Multimodel assessment of the upper troposphere and lower stratosphere: Tropics and global trends. *Journal of Geophysical Research*, 115(D14), 2010. doi: 10.1029/2009JD013638.

M. K. Gilles, A. A. Turnipseed, A. R. Ravishankara, and S. Solomon. Kinetics of the IO Radical. 2. Reaction of IO with BrO. *The Journal of Physical Chemistry A*, 101(30):5526–5534, 2011/11/09 1997. doi: 10.1021/jp9709159.

D. P. Grosvenor, T. W. Choularton, H. Coe, and G. Held. A study of the effect of overshooting deep convection on the water content of the TTL and lower stratosphere from Cloud Resolving Model simulations. *Atmospheric Chemistry & Physics*, 7:4977–5002, Sept. 2007.

R. Gunn and B. B. Phillips. An experimental investigation of the effect of air pollution on the initiation of rain. *Journal of Meteorology*, 14(3):272–280, 2011/12/02 1957. doi: {10.1175/1520-0469(1957)014⟨0272:AEIOTE⟩2.0.CO;2}.

T. F. Hanisco, E. J. Moyer, E. M. Weinstock, J. M. St. Clair, D. S. Sayres, J. B. Smith, R. Lockwood, J. G. Anderson, A. E. Dessler, F. N. Keutsch, J. R. Spackman, W. G. Read, and T. P. Bui. Observations of deep convective influence on stratospheric water vapor and its isotopic composition. *Geophysical Research Letters*, 34(4), 02 2007.

W. C. Hinds. *Aerosol technology: properties, behavior, and measurement of airborne particles*. Wiley-Interscience. Wiley, second edition, 1999.

J. Holton and A. Gettelman. Horizontal transport and the dehydration of the stratosphere. *Geophysical Research Letters*, 28(14):2799–2802, 2001.

J. T. Houghton. *The physics of atmospheres*. Cambridge University Press, New York, NY, third edition, 2002.

D. Jacob. *Introduction to atmospheric chemistry*. Princeton University Press, Princeton, NJ, 1999.

R. James, M. Bonazzola, B. Legras, K. Surbled, and S. Fueglistaler. Water vapor transport and dehydration above convective outflow during Asian monsoon. *Geophysical Research Letters*, 35(20), 10 2008. doi: 10.1029/2008GL035441.

J. Kar, R. K. Choudhary, and K. K. Mahajan. Revisiting the stratospheric fountain hypothesis using UARS/HALOE data. *Advances in Space Research*, 29:1725–1729, 2002. doi: 10.1016/S0273-1177(02)00115-1.

D. Katoshevski, A. Nenes, and J. H. Seinfeld. A study of processes that govern the maintenance of aerosols in the marine boundary layer. *Journal of Aerosol Science*, 30(4):503 – 532, 1999. doi: 10.1016/S0021-8502(98)00740-X.

D. Kirk-Davidoff, E. Hintsa, J. Anderson, and D. Keith. The effect of climate change on ozone depletion through changes in stratospheric water vapour. *Nature*, 402 (6760):399–401, 1999.

G. P. Knight and J. N. Crowley. The reactions of IO with HO_2, NO and CH_3SCH_3: Flow tube studies of kinetics and product formation. *Physical Chemistry Chemical Physics*, 3:393–401, 2001. doi: 10.1039/B008447F.

A. A. Lacis, G. A. Schmidt, D. Rind, and R. A. Ruedy. Atmospheric CO_2: Principal Control Knob Governing Earth's Temperature. *Science*, 330:356, 2010. doi: 10.1126/science.1190653.

B. Laszlo, R. E. Huie, M. J. Kurylo, and A. W. Miziolek. Kinetic studies of the reactions of BrO and IO radicals. *Journal of Geophysical Research*, (102):1523–1532, 1997. doi: 10.1029/96JD00458.

R. P. Lawson, B. Pilson, B. Baker, Q. Mo, E. Jensen, L. Pfister, and P. Bui. Aircraft measurements of microphysical properties of subvisible cirrus in the tropical tropopause layer. *Atmospheric Chemistry and Physics*, 8(6):1609–1620, 2008. doi: 10.5194/acp-8-1609-2008.

S. Levitus, J. Antonov, and T. Boyer. Warming of the world ocean, 1955–2003. *Geophysical Research Letters*, 32:2604, 2005. doi: 10.1029/2004GL021592.

X. M. Liu, E. D. Rivière, V. Marécal, G. Durry, A. Hamdouni, J. Arteta, and S. Khaykin. Stratospheric water vapour budget and convection overshooting the tropopause: modelling study from SCOUT-AMMA. *Atmospheric Chemistry & Physics*, 10:8267–8286, Sept. 2010. doi: 10.5194/acp-10-8267-2010.

T. K. Lowenstein and R. V. Demicco. Elevated Eocene Atmospheric CO_2 and Its Subsequent Decline. *Science*, 313(5795):1928, 2006. doi: 10.1126/science.1129555.

D. Lüthi, M. Le Floch, B. Bereiter, T. Blunier, J. Barnola, U. Siegenthaler, D. Raynaud, J. Jouzel, H. Fischer, K. Kawamura, et al. High-resolution carbon dioxide concentration record 650,000–800,000 years before present. *Nature*, 453(7193): 379–382, 2008.

F. Maguin, G. Laverdet, G. Le Bras, and G. Poulet. Kinetic study of the reactions iodine monoxide + hydroperoxo and iodine monoxide + nitrogen dioxide at 298 K. *The Journal of Physical Chemistry*, 96(4):1775–1780, 1992. doi: 10.1021/j100183a052.

R. P. Mason, W. F. Fitzgerald, and F. M. M. Morel. The biogeochemical cycling of elemental mercury: Anthropogenic influences. *Geochimica et Cosmochimica Acta*, 58:3191–3198, Aug. 1994. doi: 10.1016/0016-7037(94)90046-9.

M. B. McElroy, R. J. Salawitch, S. C. Wofsy, and J. A. Logan. Reductions of Antarctic ozone due to synergistic interactions of chlorine and bromine. *Nature*, 321:759–762, June 1986. doi: 10.1038/321759a0.

R. L. McKenzie, C. Weinreis, P. V. Johnston, B. Liley, H. Shiona, M. Kotkamp, D. Smale, N. Takegawa, and Y. Kondo. Effects of urban pollution on UV spectral irradiances. *Atmospheric Chemistry and Physics*, 8(18):5683–5697, 2008. doi: 10.5194/acp-8-5683-2008.

R. A. Millikan. On the Elementary Electrical Charge and the Avogadro Constant. *Physical Review*, 2:109–143, Aug. 1913. doi: 10.1103/PhysRev.2.109.

K. Minschwaner, G. L. Manney, S. H. Wang, and R. S. Harwood. Hydroxyl in the stratosphere and mesosphere — Part 1: Diurnal variability. *Atmospheric Chemistry and Physics*, 11(3):955–962, 2011. doi: 10.5194/acp-11-955-2011.

R. W. Mueller, H. Bovensmann, J. W. Kaiser, A. Richter, A. Rozanov, F. Wittrock, and J. P. Burrows. Consistent interpretation of ground based and GOME BrO slant column data. *Advances in Space Research*, 29:1655–1660, 2002. doi: 10.1016/S0273-1177(02)00097-2.

R. E. Newell and S. Gould-Stewart. A Stratospheric Fountain?. *Journal of Atmospheric Sciences*, 38:2789–2789, Dec. 1981. doi: 10.1175/1520-0469(1981)038⟨2789:ASF⟩2.0.CO;2.

P. A. Newman and R. McKenzie. UV impacts avoided by the Montreal Protocol. *Photochemical & Photobiological Sciences*, 10:1152–1160, 2011. doi: 10.1039/C0PP00387E.

P. A. Newman, L. D. Oman, A. R. Douglass, E. L. Fleming, S. M. Frith, M. M. Hurwitz, S. R. Kawa, C. H. Jackman, N. A. Krotkov, E. R. Nash, J. E. Nielsen, S. Pawson, R. S. Stolarski, and G. J. M. Velders. What would have happened to the ozone layer if chlorofluorocarbons (CFCs) had not been regulated? *Atmospheric Chemistry and Physics*, 9(6):2113–2128, 2009. doi: 10.5194/acp-9-2113-2009.

C. D. O'Dowd, J. L. Jimenez, R. Bahreini, R. C. Flagan, J. H. Seinfeld, K. Hämeri, L. Pirjola, M. Kulmala, S. G. Jennings, and T. Hoffmann. Marine aerosol formation from biogenic iodine emissions. *Nature*, 417:632–636, June 2002.

S. J. Oltmans, H. Vömel, D. J. Hofmann, K. H. Rosenlof, and D. Kley. The increase in stratospheric water vapor from balloonborne, frostpoint hygrometer measurements at Washington, D.C., and Boulder, Colorado. *Geophysical Research Letters*, 27:3453–3456, Nov. 2000. doi: 10.1029/2000GL012133.

E. G. Pacyna, J. M. Pacyna, F. Steenhuisen, and S. Wilson. Global anthropogenic mercury emission inventory for 2000. *Atmospheric Environment*, 40(22):4048 – 4063, 2006. doi: 10.1016/j.atmosenv.2006.03.041.

J. Petit, J. Jouzel, D. Raynaud, N. Barkov, J. Barnola, I. Basile, M. Bender, J. Chappellaz, M. Davis, G. Delaygue, et al. Climate and atmospheric history of the past

420,000 years from the Vostok ice core, Antarctica. *Nature*, 399(6735):429–436, 1999.

J.-P. Pommereau and G. Held. Is there a stratospheric fountain? *Atmospheric Chemistry & Physics Discussions*, 7:8933–8950, June 2007.

B. E. Potter and J. R. Holton. The Role of Monsoon Convection in the Dehydration of the Lower Tropical Stratosphere. *Journal of Atmospheric Sciences*, 52:1034–1050, Apr. 1995. doi: 10.1175/1520-0469(1995)052⟨1034:TROMCI⟩2.0.CO;2.

I. Pundt, J.-P. Pommereau, C. Phillips, and E. Lateltin. Upper Limit of Iodine Oxide in the Lower Stratosphere. *Journal of Atmospheric Chemistry*, 30:173–185, 1998. 10.1023/A:1006071612477.

L. F. Radke, J. A. Coakley, and M. D. King. Direct and Remote Sensing Observations of the Effects of Ships on Clouds. *Science*, 246:1146–1149, Dec. 1989. doi: 10.1126/science.246.4934.1146.

P. Ricaud, B. Barret, J.-L. Attié, E. Motte, E. Le Flochmoën, H. Teyssèdre, V.-H. Peuch, N. Livesey, A. Lambert, and J.-P. Pommereau. Impact of land convection on troposphere-stratosphere exchange in the tropics. *Atmospheric Chemistry and Physics*, 7(21):5639–5657, 2007. doi: 10.5194/acp-7-5639-2007.

A. Richter, F. Wittrock, M. Eisinger, and J. P. Burrows. GOME observations of tropospheric BrO in northern hemispheric spring and summer 1997. *Geophysical Research Letters*, 25:2683–2686, 1998. doi: 10.1029/98GL52016.

E. Rignot, I. Velicogna, M. R. van den Broeke, A. Monaghan, and J. Lenaerts. Acceleration of the contribution of the Greenland and Antarctic ice sheets to sea level rise. *Geophysical Research Letters*, 38:L05503, Mar. 2011. doi: 10.1029/2011GL046583.

G. D. Robinson. The transport of minor atmospheric constituents between troposphere and stratosphere. *Quarterly Journal of the Royal Meteorological Society*, 106:227–253, Apr. 1980. doi: 10.1002/qj.49710644802.

D. Rosenfeld, U. Lohmann, G. B. Raga, C. D. O'Dowd, M. Kulmala, S. Fuzzi, A. Reissell, and M. O. Andreae. Flood or Drought: How Do Aerosols Affect Precipitation? *Science*, 321:1309–1313, Sept. 2008. doi: 10.1126/science.1160606.

K. Rosenlof, S. Oltmans, D. Kley, J. Russell III, E. Chiou, W. Chu, D. Johnson, K. Kelly, H. Michelsen, G. Nedoluha, et al. Stratospheric water vapor increases over the past half-century. *Geophysical Research Letters*, 28(7):1195–1198, 2001.

K. Sassen. Corona-producing cirrus cloud properties derived from polarization lidar and photographic analyses. *Applied Optics*, 30(24):3421–3428, Aug 1991. doi: 10.1364/AO.30.003421.

R. W. Saunders, R. Kumar, J. C. Gómez Martín, A. S. Mahajan, B. J. Murray, and J. M. C. Plane. Studies of the formation and growth of aerosol from molecular iodine precursor. *Zeitschrift für Physikalische Chemie*, 224(7-8):1095–1117, 2011/12/14 2010. doi: 10.1524/zpch.2010.6143.

G. A. Schmidt, R. A. Ruedy, R. L. Miller, and A. A. Lacis. Attribution of the present-day total greenhouse effect. *Journal of Geophysical Research*, 115(D14): 20106, 2010. doi: 10.1029/2010JD014287.

W. H. Schroeder and J. Munthe. Atmospheric mercury–An overview. *Atmospheric Environment*, 32(5):809–822, 1998. doi: 10.1016/S1352-2310(97)00293-8. ¡ce:title¿Atmospheric Transport, Chemistry and Deposition of Mercury¡/ce:title¿.

G. Seckmeyer, M. Glandorf, C. Wichers, R. McKenzie, D. Henriques, F. Carvalho, A. Webb, A.-M. Siani, A. Bais, B. Kjeldstad, C. Brogniez, P. Werle, T. Koskela, K. Lakkala, J. Grobner, H. Slaper, P. denOuter, and U. Feister. Europe's darker atmosphere in the UV-B. *Photochem. Photobiol. Sci.*, 7:925–930, 2008. doi: 10.1039/B804109A.

D. J. Seidel, R. J. Ross, J. K. Angell, and G. C. Reid. Climatological characteristics of the tropical tropopause as revealed by radiosondes. *Journal of Geophysical Research*, 106:7857–7878, 2001. doi: 10.1029/2000JD900837.

R. B. Setlow. The Wavelengths in Sunlight Effective in Producing Skin Cancer: A Theoretical Analysis. *Proceedings of the National Academy of Sciences*, 71(9): 3363–3366, 1974.

S. C. Sherwood and A. E. Dessler. On the control of stratospheric humidity. *Geophysical Research Letters*, 27:2513–2516, Aug. 2000. doi: 10.1029/2000GL011438.

U. Siegenthaler, T. Stocker, E. Monnin, D. Luthi, J. Schwander, B. Stauffer, D. Raynaud, J. Barnola, H. Fischer, V. Masson-Delmotte, et al. Stable carbon cycle-climate relationship during the late Pleistocene. *Science*, 310(5752):1313, 2005.

V. Smil. *Energy at the crossroads: global perspectives and uncertainties*. MIT Press, Cambridge, MA, 2005.

C. Smith, J. Haigh, and R. Toumi. Radiative forcing due to trends in stratospheric water vapour. *Geophysical Research Letters*, 28(1):179–182, 2001.

S. Solomon. *Climate Change 2007: the physical science basis. Contribution of Working Group I to the Fourth Assessment Report of the Intergovernmental Panel on Climate Change*. Cambridge University Press, Cambridge, United Kingdom and New York, NY, USA, 2007.

S. Solomon, J. B. Burkholder, A. R. Ravishankara, and R. R. Garcia. Ozone depletion and global warming potentials of CF_3I. *Journal of Geophysical Research*, 992: 20929–20936, Oct. 1994a. doi: 10.1029/94JD01833.

S. Solomon, R. R. Garcia, and A. R. Ravishankara. On the role of iodine in ozone depletion. *Journal of Geophysical Research*, 992:20491–20500, Oct. 1994b. doi: 10.1029/94JD02028.

S. Solomon, S. Bormann, R. R. Garcia, R. Portmann, L. Thomason, L. R. Poole, D. Winker, and M. P. McCormick. Heterogeneous chlorine chemistry in the tropopause region. *Journal of Geophysical Research*, 1022:21411–21430, 1997. doi: 10.1029/97JD01525.

P. Squires. The microstructure and colloidal stability of warm clouds. *Tellus*, 10(2): 256–261, 1958. doi: 10.1111/j.2153-3490.1958.tb02011.x.

A. Steffen, W. Schroeder, R. Macdonald, L. Poissant, and A. Konoplev. Mercury in the Arctic atmosphere: An analysis of eight years of measurements of GEM at Alert (Canada) and a comparison with observations at Amderma (Russia) and Kuujjuarapik (Canada). *Science of The Total Environment*, 342(1-3):185–198, 2005. doi: 10.1016/j.scitotenv.2004.12.048.

R. M. Stimpfle, R. C. Cohen, G. P. Bonne, P. B. Voss, K. K. Perkins, L. C. Koch, J. G. Anderson, R. J. Salawitch, S. A. Lloyd, R. S. Gao, L. A. Del Negro, E. R. Keim, and T. P. Bui. The coupling of $ClONO_2$, ClO, and NO_2 in the lower stratosphere from in situ observations using the NASA ER-2 aircraft. *Journal of Geophysical Research*, 1042:26705–26714, 1999. doi: 10.1029/1999JD900288.

D. G. Streets, J. Hao, Y. Wu, J. Jiang, M. Chan, H. Tian, and X. Feng. Anthropogenic mercury emissions in China. *Atmospheric Environment*, 39(40):7789 – 7806, 2005. doi: 10.1016/j.atmosenv.2005.08.029.

E. T. Sundquist and R. F. Keeling. The Mauna Loa carbon dioxide record: Lessons for long-term Earth observations. In B. J. McPherson and E. T. Sundquist, editors, *Carbon Sequestration and Its Role in the Global Carbon Cycle, Geophys. Monogr. Ser.*, volume 183, pages 27–35. AGU, Washington, D. C., 2009. doi: 10.1029/2009GM000913.

H. R. Taylor, S. K. West, F. S. Rosenthal, B. Muñoz, H. S. Newland, H. Abbey, and E. A. Emmett. Effect of Ultraviolet Radiation on Cataract Formation. *New England Journal of Medicine*, 319(22):1429–1433, 1988. doi: 10.1056/NEJM198812013192201.

A. A. Turnipseed, M. K. Gilles, J. B. Burkholder, and A. R. Ravishankara. Kinetics of the IO Radical. 1. Reaction of IO with ClO. *The Journal of Physical Chemistry A*, 101(30):5517–5525, 1997. doi: 10.1021/jp970914g.

J. Tyndall. On Radiation through the Earth's Atmosphere. *Philosophical Magazine*, ser. 4(25):200–206, 1863.

UNEP. *The Global Atmospheric Mercury Assessment: Sources, Emissions and Transport*. UNEP Chemicals Branch, Geneva, 2008.

J. A. van Aardenne, G. R. Carmichael, H. L. II, D. Streets, and L. Hordijk. Anthropogenic NO_x emissions in Asia in the period 1990—2020. *Atmospheric Environment*, 33(4):633–646, 1999. doi: 10.1016/S1352-2310(98)00110-1.

P. O. Wennberg, R. C. Cohen, R. M. Stimpfle, J. P. Koplow, J. G. Anderson, R. J. Salawitch, D. W. Fahey, E. L. Woodbridge, E. R. Keim, R. S. Gao, C. R. Webster, R. D. May, D. W. Toohey, L. M. Avallone, M. H. Proffitt, M. Loewenstein, J. R. Podolske, K. R. Chan, and S. C. Wofsy. Removal of Stratospheric O_3 by Radicals: In Situ Measurements of OH, HO_2, NO, NO_2, ClO, and BrO. *Science*, 266:398–404, Oct. 1994. doi: 10.1126/science.266.5184.398.

P. O. Wennberg, J. W. Brault, T. F. Hanisco, R. J. Salawitch, and G. H. Mount. The atmospheric column abundance of IO: Implications for stratospheric ozone. *Journal of Geophysical Research*, 102:8887–8898, Apr. 1997. doi: 10.1029/96JD03712.

D. M. Winker and C. R. Trepte. Laminar cirrus observed near the tropical tropopause by lite. *Geophysical Research Letters*, 25(17):3351–3354, Sep 1998.

F. Wittrock, R. Müller, A. Richter, H. Bovensmann, and J. P. Burrows. Measurements of Iodine monoxide (IO) above Spitsbergen. *Geophysical Research Letters*, 27:1471, May 2000. doi: 10.1029/1999GL011146.

WMO. *Scientific Assessment of Ozone Depletion: 2010*. Global Ozone Research and Monitoring Project–Report No. 52. World Meteorological Organization, Geneva, Switzerland, 2011.

X.-L. Zhou, M. A. Geller, and M. Zhang. Cooling trend of the tropical cold point tropopause temperatures and its implications. *Journal of Geophysical Research*, 106:1511–1522, 2001. doi: 10.1029/2000JD900472.

Chapter 2

Water Isotopologue Instruments

> How profound that mystery of the Invisible is! We cannot fathom it with our miserable senses, with our eyes which are unable to perceive what is either too small or too great, too near to us, or too far from us—neither the inhabitants of a star nor of a drop of water...
>
> *The Horla*
> Guy de Maupassant

2.1 Introduction

The sensitivity requirements set forth to accurately detect water isotopologues in UT/LS, with constraints on fast sampling times to achieve adequate spatial resolution dictated by the cruise speed of an aircraft, are determined by the natural abundance of the isotopes and the physical factors controlling the vertical profile of water vapor. To measure water vapor throughout the entire troposphere presents instrumentation challenges in itself, where the water vapor mixing ratio ranges from a few percent near the surface to a few parts per million at the tropopause: a dynamic range covering 6 orders of magnitude. Instruments developed to for the UT/LS cover a more limited dynamic range, yet must grapple with low water vapor mixing ratios. If a detection channel designed to measure the isotopes of water is required, the natural abundance of semi-heavy water (HDO), which at the surface is one part in nearly every 3200 molecules of water, illustrates the increased challenge. Furthermore, isotopic fractionation preferentially removes the heavier isotopologues (e.g., HDO or $H_2^{18}O$) during condensation, so that the mixing ratio of these can be less than one part per billion by volume in the upper troposphere! To resolve large cloud-scale features requires spatial resolutions less than a kilometer on aircraft traveling 200 m s^{-1}, means that sampling times must be on the order of a few seconds.

2.1.1 Geochemical Notation & Molecular Detection

Delta-notation δ is generally expressed in terms of the ratio of the heavier isotope to the lighter isotope, deuterium relative to hydrogen for instance, and is referenced

Table 2.1: Isotope Abundance in VSMOW

Isotope	Mass	Abundance	Isotope	Mass	Abundance
^{1}H (H)	1.00782	0.99984426(5)	^{16}O	15.994915	0.9976206(5)
^{2}H (D)	2.01410	0.00015574(5)	^{17}O	16.999132	0.0003790(9)
^{3}H (T)	3.01604	*	^{18}O	17.999160	0.0020004(5)

mass: Audi and Wapstra (1993, 1995); abund.: de Laeter et al. (2003).
* ^{3}H (tritium) is extremely rare, abund. $< 10^{-17}$ %.

to that same ratio in a standard:

$$\delta\mathrm{D} = \left[\frac{([\mathrm{D}]/[\mathrm{H}])_{sample}}{([\mathrm{D}]/[\mathrm{H}])_{std.}} - 1\right] \times 1000 \tag{2.1}$$

where $([\mathrm{D}]/[\mathrm{H}])_{std.}$ is a defined isotope ratio termed "Vienna Standard Mean Ocean Water" (VSMOW) and has a value, $\mathrm{D/H} = 155.76 \pm 0.1 \times 10^{-6}$ (de Laeter et al., 2003). Delta-notation expresses the difference between the isotopic composition of a sample and a standard, which is often small, hence being expressed terms of per mille (i.e., part per thousand). Historically, the isotopic composition of a sample is determined by mass analysis of bulk elemental composition, where the reference to a known standard yields an instrumental calibration.

However, when making an isotopic measurement in terms of molecular structure a transformation is required to express the isotope ratio in the δD framework. Consider the ratio of deuterium to hydrogen in a sample of water: water is present in light (H_2O), semi-heavy (HDO) and heavy (D_2O) forms for each isotope of oxygen (^{16}O, ^{17}O and ^{18}O), such that the ratio of deuterium to hydrogen must be expressed for

all the possible isotopologues of water

$$\left(\frac{[\mathrm{D}]}{[\mathrm{H}]}\right)_{sample} = \frac{\sum_{i=16}^{18}[\mathrm{HD}^{i}\mathrm{O}] + 2\sum_{i=16}^{18}[\mathrm{D}_2{}^{i}\mathrm{O}]}{2\sum_{i=16}^{18}[\mathrm{H}_2{}^{i}\mathrm{O}] + \sum_{i=16}^{18}[\mathrm{HD}^{i}\mathrm{O}]} \tag{2.2}$$

where each molecule of semi-heavy water contributes 1 atom of hydrogen and deuterium and the light and heavy isotopologues contribute 2 atoms of either hydrogen or deuterium, respectively. Tritium is an extremely rare isotope (see Table 2.1) and can be neglected.

The only significant contribution to the deuterated form of water is from $\mathrm{HD}^{16}\mathrm{O}$ (see Table 2.2), which makes up over 99.7 % of deuterated water. The dominant contributor to hydrogen is $\mathrm{H}_2^{16}\mathrm{O}$, making up the vast majority of water isotopologues. Neglecting the minor contributors, equation 2.2 can be simplified, to a very good approximation, as

$$\left(\frac{[\mathrm{D}]}{[\mathrm{H}]}\right)_{sample} \approx \frac{[\mathrm{HD}^{16}\mathrm{O}]}{2[\mathrm{H}_2^{16}\mathrm{O}]}. \tag{2.3}$$

Measurements of water isotopologues (i.e., the isotopes of molecular water) can therefore be expressed in terms of δD notation by substituting eq. 2.3 into eq. 2.1, adjusting for the fact that each molecule of $\mathrm{H}_2^{16}\mathrm{O}$ is the source of 2 hydrogen atoms:

$$\begin{aligned}\delta\mathrm{D} &= \left[\frac{([\mathrm{D}]/[\mathrm{H}])_{sample}}{([\mathrm{D}]/[\mathrm{H}]_{std.})} - 1\right] \times 1000 \\ &= \left[\frac{([\mathrm{HD}^{16}\mathrm{O}]/[\mathrm{H}_2^{16}\mathrm{O}])_{sample}}{2 \times \mathrm{VSMOW}} - 1\right] \times 1000.\end{aligned} \tag{2.4}$$

Table 2.2: Abundance of Water Isotopologues in VSMOW

Isotopologue	Abundance
$H_2^{16}O$	0.997309885
$H_2^{18}O$	0.001999777
$H_2^{17}O$	0.000378882
$HD^{16}O$	0.000310690
$HD^{18}O$	6.22988×10^{-7}
$HD^{17}O$	1.18033×10^{-8}
$D_2^{16}O$	2.41972×10^{-8}
$D_2^{18}O$	4.85196×10^{-11}
$D_2^{17}O$	9.19263×10^{-12}

2.2 Hoxotope Total Water Instrument

Both the optical detection scheme of Hoxotope and the general subsystems of the instrument have been previously discussed (St. Clair et al., 2008; Wennberg et al., 1994). A brief description of the instrument is given here and recent modifications to the instrument will be discussed in greater detail.

2.2.1 Measurement Technique: Photolysis/LIF

The hydrogen isotopes of water (H_2O and HDO) are detected by a combination of photolysis and laser-induced fluorescence (LIF). A photolysis system produces OH and OD from H_2O and HDO, respectively. The nascent OH and OD radicals are then detected using the same technique as previously used to detect OH in the Harvard ER-2 HO_x instrument (Wennberg et al., 1994).

Photolysis of H_2O and HDO to produce ground-state radicals relies on the ab-

sorption of vacuum ultraviolet (VUV) radiation:

$$\mathrm{H_2O} + h\nu_{172\,\mathrm{nm}} \rightarrow \mathrm{H} + \mathrm{OH}(\chi^2\Pi)(v'' = 0) \quad \Phi_{\mathrm{OH}} = 1, \tag{2.5}$$

$$\mathrm{HDO} + h\nu_{172\,\mathrm{nm}} \rightarrow \mathrm{H} + \mathrm{OD}(\chi^2\Pi)(v'' = 0) \quad \Phi_{\mathrm{OD}} = 0.8. \tag{2.6}$$

The quantum yield for photolysis of OH in Equation (2.5) is unity (Sander et al., 2006), while the quantum yield for OD in Equation (2.6) is roughly 80 %, depending on wavelength (Shafer et al., 1989; Zhang et al., 1989).

The nascent OH and OD are then detected downstream via LIF. OH and OD fluoresce via a mechanism that is initiated by collisional relaxation of the excited state (Vaghjiani and Ravishankara, 1987; Steffens and Crosley, 2000):

$$\mathrm{OH}(\chi^2\Pi)(v'' = 0) + h\nu_{288\,\mathrm{nm}} \rightarrow \mathrm{OH}(A^2\Sigma)(v' = 1), \tag{2.7}$$

$$\mathrm{OH}(A^2\Sigma)(v' = 1) + \mathrm{M} \rightarrow \mathrm{OH}(A^2\Sigma)(v' = 0), \tag{2.8}$$

$$\mathrm{OH}(A^2\Sigma)(v' = 0) \rightarrow \mathrm{OH}(\chi^2\Pi)(v'' = 0) + h\nu_{309\,\mathrm{nm}}. \tag{2.9}$$

The combination of a spectral separation of the excitation and fluorescence signals and the long lifetime ($\approx$ 100 ns at 11.5 Torr) of OH in the $A^2\Sigma(v' = 0)$ state give this detection scheme a great degree of sensitivity.

2.2.2 Optical Design & Components

2.2.2.1 Laser System & Light Source

A Nd^{3+}:YAG (Spectra Physics T40-X30) laser produces nearly 2.5 W of 532 nm light at a repetition rate of 10 kHz with each pulse having a length of 25 ns (FWHM). This is used to pump a dye laser (Chromatix, modified) circulating Rhodamine 6G dye in ethanol. Broadband wavelength selection is achieved by three prisms in combination with a motor-actuated bellows to tune the dye laser by modifying pressure. An intracavity etalon, on a rotating ferrofluidic cylinder driven by a linear actuated stepper motor, provides narrow linewidth selection of the dye laser's wavelength. The fundamental wavelength is frequency-doubled by an intracavity barium borate (BBO) crystal to produce 288 nm ultraviolet radiation that is used to initiate an electronic transition in OH.

The instrument utilizes a frequency reference cell to maintain control over the laser wavelength. OD is produced in the reference cell by reaction of a D_2O source (heated $CaCO_3 \cdot D_2O$) with O_2 on a glowing NiChrome filament in the presence of N_2. While no OH is generated in the frequency reference cell, the OH line position is easily obtained by moving a fixed number of steps from the OD line position. This is possible due to the low root-mean-square error of the etalon stepper driver across the scanning region (< 4 parts per thousand).

2.2.2.2 UV Photolysis System

The photolysis system is comprised of two Xe excimer lamps (Osram XERADEX 20) providing a total of 16 W of nearly monochromatic 172 nm light. The lamps are

operated with a repetition rate of 30 kHz with each pulse lasting for 2 μs giving a duty cycle of approximately 6 %. A modified commercial power supply, implementing an in-house master timing circuit to synchronize the output from the flash lamps and the detection laser trigger, is used to eliminate most lamp scatter from detection by the gated PMT.

2.2.2.3 Optical Detection

The 288 nm light generated by the dye laser is directed into a White cell that is orthogonal to the flow in the horizontal-plane along the detection axis. Mirrors are located 266 mm apart providing 22-passes of the excitation laser. A cross-sectional area of 4 cm^2 of the core of the flow is sampled by this White Cell configuration.

A PMT is situated orthogonal to the White cell in the vertical-plane. An interference filter centered at 309 nm with a 6 nm bandwidth (FWHM) is used to block the excitation laser at shorter wavelengths and background signal in the PMT response range (200 – 700 nm). Interferences from the excitation laser are further minimized by gating the PMT to collect the long-lived OH and OD fluorescence after the laser pulse. Additionally, background interference from prompt Raman and Rayleigh scattering are minimized by this gated detection scheme.

2.2.3 Sampling

Water vapor is sampled from the bulk flow by a pick-off valve. A pinch valve assembly upstream of the pick-off and prior to the detection axis maintains a constant pressure of 11.5 Torr in the detection assembly, regardless of pressure fluctuations in

the bulk flow. A pinch valve modifies the pressure by changing the conductance of a tube by deformation and does so without adding stagnant "dead" volumes.

St. Clair et al. (2008) evaluated the potential contamination in Hoxotope by comparison with the Lyman-α instrument during the AVE-WIIF campaign. Hoxotope was deployed as a vapor phase water isotope instrument during this mission so that an intercomparison with Lyman-α throughout all regions of flight was possible. The Harvard Lyman-α water vapor instrument is a well established instrument and has a long heritage of measurements in the upper troposphere and lower stratosphere aboard both the ER-2 and WB-57 research aircraft. Simultaneous photofragmentation fluorescence and absorption techniques give Lyman-α a dynamic range suitable for making measurements from the lower troposphere to the lower stratosphere, where water vapor concentrations vary from a few percent to as low as 2 ppm. Lyman-α experiences significantly higher flow rates ($\sim$ 50 – 60 m/s) during flight than Hoxotope and wall contamination has been demonstrated to not be an issue (Hintsa et al., 1999).

Early in a flight, following ascent, a large water contamination signal is usually seen in Hoxotope which is the result of condensation during ascent. Excluding this data, excellent agreement between the two instruments is found for all measurements of $H_2O < 200$ ppm. Time series comparisons of both instruments throughout all flights found that the fractional difference between Hoxotope and Lyman-α stayed within the 95 % confidence (2σ) envelope across flights, even when moving between regions with a sharp gradient in H_2O. The absence of wall contamination and sampling artifacts in Hoxotope when sampling vapor is a preliminary requirement for a

subsequent implementation as a total water instrument.

2.2.4 Calibration

Hoxotope is calibrated in the laboratory by the standard addition of a known quantity of water vapor to the bulk flow. The bulk flow consists of either dry nitrogen or ultra-zero air passed through a desiccant so that contains less than 3 ppmv H_2O. Saturated air is added to the bulk flow through either of two flow controllers (MKS, 1197A). Saturated air or nitrogen is generated by passing this supplementary flow through bubblers. The quantity of water in the air is determined by the pressure and temperature dependent saturation ratio. The bubblers are kept very near 1 atm and the temperature of the bubblers are constantly monitored so that the saturation ratio can be accurately determined. Fractionation of isotopes is inevitable in an evaporative process (such as generating saturated air with a bubbler) however a temperature dependent functional form for fractionation, given by $\ln(R_c/R_v) = -0.1 + 15013/T^2$ (Johnson et al., 2001), is used to account for this.

In the laboratory, a relationship between the fluorescence signal and concentration of OH and OD is determined from the standard water addition. In the absence of any loss pathway, the concentration of OH is related to the concentration of water added by the effective photolysis yield, $[OH] = \phi[H_2O]$. However, the UV flash lamps

initiate a considerable amount of chemistry in the detection axis:

$$\mathrm{O_2} + h\nu_{172\,\mathrm{nm}} \rightarrow 2\,\mathrm{O} \tag{2.10}$$

$$\mathrm{O} + \mathrm{O_2} \rightarrow \mathrm{O_3} \tag{2.11}$$

$$\mathrm{H} + \mathrm{O_2} + \mathrm{M} \rightarrow \mathrm{HO_2} + \mathrm{M} \tag{2.12}$$

$$\mathrm{OH} + \mathrm{O_3} \rightarrow \mathrm{HO_2} + \mathrm{O_2} \tag{2.13}$$

$$\mathrm{HO_2} + \mathrm{O_3} \rightarrow \mathrm{OH} + 2\,\mathrm{O_2} \tag{2.14}$$

$$\mathrm{OH} + \mathrm{HO_2} \rightarrow \mathrm{H_2O} + \mathrm{O_2} \tag{2.15}$$

A full chemical model of OH described by the reactions above can be used during calibration, although it is cumbersome (St. Clair et al., 2008). A simplified model of the evolution of OH in the detection axis is obtained by considering only the dominant loss pathway for OH, described by reaction 2.15. The rate of change in the concentration of OH is then

$$\frac{d[\mathrm{OH}]}{dt} = -k[\mathrm{OH}][\mathrm{HO_2}]. \tag{2.16}$$

The heterolytic photolysis of $\mathrm{H_2O}$ (rxn. 2.5) produces equivalent fractions of H and OH. H-atoms produced by this process are generally regarded (Fuchs et al., 2011) as being completely converted to $\mathrm{HO_2}$ as collisions quickly remove excess energy from H eliminating losses to competing pathways. Furthermore, since $k_{2.12}[\mathrm{H}][\mathrm{O_2}][\mathrm{M}] \gg k_{2.15}[\mathrm{OH}][\mathrm{HO_2}]$ (for instance at 11.5 Torr and 100 ppb of OH, reaction 2.12 proceeds 2 orders of magnitude faster than reaction 2.15), H is fully converted to $\mathrm{HO_2}$ prior

to initiation of reaction 2.15 (Sander et al., 2006; Kurylo, 1972). The initial concentration of HO_2 is then equivalent to OH, by virtue of reactions 2.5 and 2.12, and remains equivalent to OH throughout reaction 2.15 as this is the only loss pathway in this simplified model, the rate of loss of OH can thus be taken to be second order in OH giving an analytical solution for the loss of OH in the duct:

$$[\mathrm{OH}]_t = \frac{\phi[\mathrm{H_2O}]}{kt\phi[\mathrm{H_2O}] + 1} \tag{2.17}$$

where ϕ is the effective yield of photolysis, t is the time between photolysis and detection and k is the rate constant for the reaction between OH and HO_2. A "laboratory calibration" of [OH] is determined from $[H_2O]$ by a least squares fit of ϕ and t to the data. Note that any first order losses in OH are accounted for in the fit parameters. The diminishing sensitivity to OH, resulting from non-linearities at high water concentrations, and the typical abundance of water in the UT/LS place a practical upper limit of laboratory calibrations near 300 ppm H_2O; although calibrations up to 1000 ppm are performed to evaluate the instrumental response during high water encounters. During flight, $[H_2O]$ is determined from [OH] by inverting equation 2.17.

2.2.5 New Isokinetic Inlet

The major modification made to Hoxotope for the TC4 mission was the transition to sampling total water (i.e., condensed + vapor phases), whereas in previous field deployments only the vapor phase was sampled. Accurate measurements of

total water can only be achieved by accurate sampling of the condensed phase; the following sampling conditions must be met:

1. *Isokinetic flow*—the velocity at the inlet is equivalent to the free-stream velocity in order to create undistorted streamlines upstream of the inlet. Particles are sampled equivalently regardless of size if this condition is met. If the velocity at the inlet is greater (less) than the free-stream velocity, divergent (convergent) streamlines near the inlet result in oversampling of large (small) particles due to particle inertia in the region of curved streamlines near the inlet (see Fig. 2.2).

2. *Contamination free sampling*—there are no sampling artifacts from residual liquid water in the inlet. Liquid water contamination, a result of water sticking to the walls or trapped in dead volumes, in a closed system introduces measurement errors. This is an issue when sampling in and out of clouds, where cloud features may not be resolved as a result of hysteresis in measurements.

3. *Complete evaporation*—accurate measurements of the condensed phase require that it is completely converted to the gas phase prior to detection. Incomplete conversion of the condensed phase will produce erroneously low measurements of total water.

2.2.5.1 Theory of Isokinetic Sampling

Isokinetic flow is established at the inlet by maintaining a zero-differential pressure (static) between the inlet and the external free-stream. A throttle-valve as-

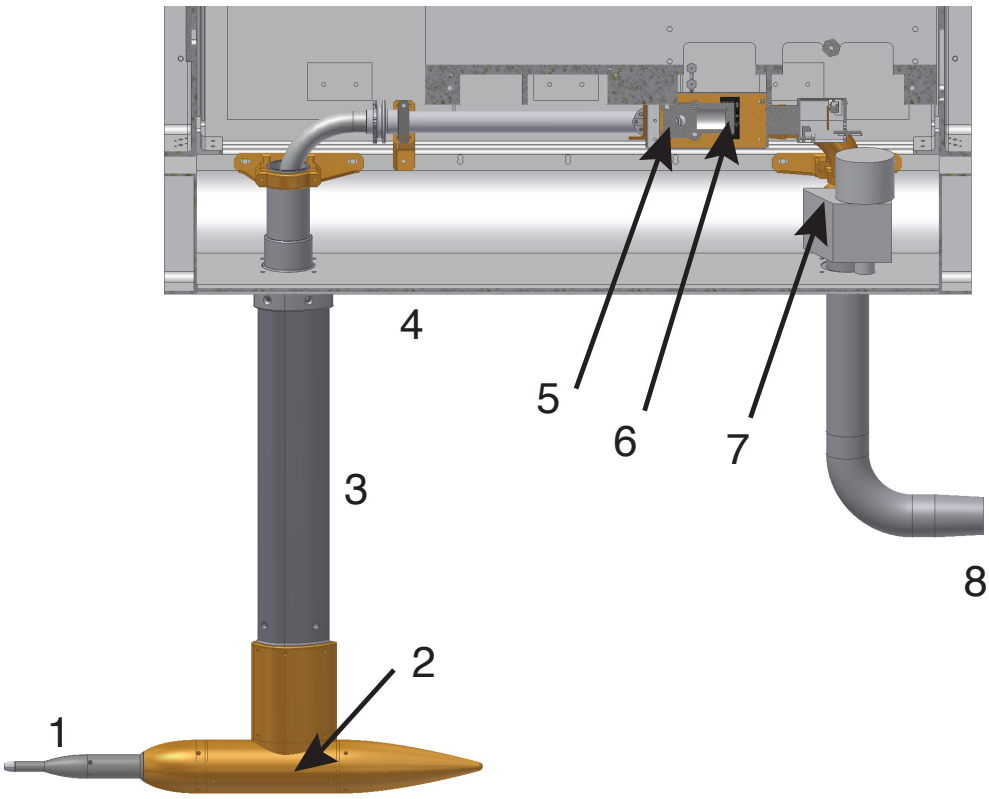

Figure 2.1: The isokinetic inlet as mounted in a standard WB-57 pallet, labels refer to: (1) pressure ports and inlet cartridge heater; (2) cartridge heater at elbow, differential sensor mounted aft of elbow; (3) winglet extends 0.81 m from pallet wall, heating tape along length of inlet duct; (4) pallet skin wall, port-side; (5) pick-off inlet to sampling duct; (6) pitot tube and thermistor; (7) throttle valve; (8) Venturi exhaust.

sembly located downstream of the detection axis pickoff maintains isokinetic flow velocities through the main inlet by regulating upstream pressure in the inlet with the use of a butterfly-type valve. The valve's position is driven by a stepper motor that operates in a PID loop and is controlled by the differential pressure sensor (All Sensors, 1 INCH-D-4V-MIL).

The fact that isokinetic sampling can be achieved by maintaining null differential static pressure between the inlet and the free-stream is illustrated here. Consider two hypothetical pitot-static tubes: one placed upstream on the inlet such that it measures the flow velocity of the free-stream, w, and the other placed in the middle of the inlet such that it measures the flow velocity at the inlet, v. Applying Bernoulli's equation to the pressure differential measured across the dynamic and static ports of each pitot-static tube allows for the flow velocity to be determined,

$$w = \sqrt{\frac{2RTp_d}{Mp_s}} \quad \text{and} \quad v = \sqrt{\frac{2RTp'_d}{Mp'_s}} \tag{2.18}$$

where R is the universal gas constant, T is the temperature, M is the molecular weight of the gas, p_d is the differential pressure, and p_s is the static pressure. The differential pressure is the difference between the total pressure (i.e., stagnation = dynamic + static) and the static pressure and, therefore, represents the dynamic pressure in a pitot-static tube. Isokinetic sampling is satisfied under the condition that the flow velocity through the inlet is equal to external free-stream flow velocity,

that is when $v = w$. If this condition is satisfied, the following equation holds true:

$$\frac{2RT}{M}\left(\frac{p_d}{p_s} - \frac{p'_d}{p'_s}\right) = 0. \tag{2.19}$$

In the case of isokinetic sampling, the temperature of the external flow and that at the inlet can be treated as constant. Any changes to the temperature of the flow at the inlet as a result of the inlet heaters would be negligible at the point where the inlet's static pressure is measured. The identity above is satisfied when

$$\frac{p_d}{p_s} = \frac{p'_d}{p'_s} \tag{2.20}$$

or, equivalently,

$$p_d = p'_d \quad \text{when} \quad p'_s = p_s. \tag{2.21}$$

Maintaining a zero-differential pressure between the inlet and free-stream (i.e., $p'_s = p_s$) results in an equivalent dynamic pressure in the two regions, thereby generating a constant flow velocity between the free-stream and the inlet.

The benefit of isokinetic sampling is that no calibration factor is required to account for deviations in the particle count between particles sampled and those in the free-stream. In the case that the velocity at the inlet is less than that of the free-stream, $v_{inlet} < v_{tas}$, sampling is said to be *subisokinetic*. Under such conditions the free-flow streamlines diverge at the inlet and larger particles are over-sampled due to their inertia. For the opposite case, *superisokinetic* sampling, where the velocity at the inlet is greater than the free-stream, $v_{inlet} > v_{tas}$, the free-flow streamlines con-

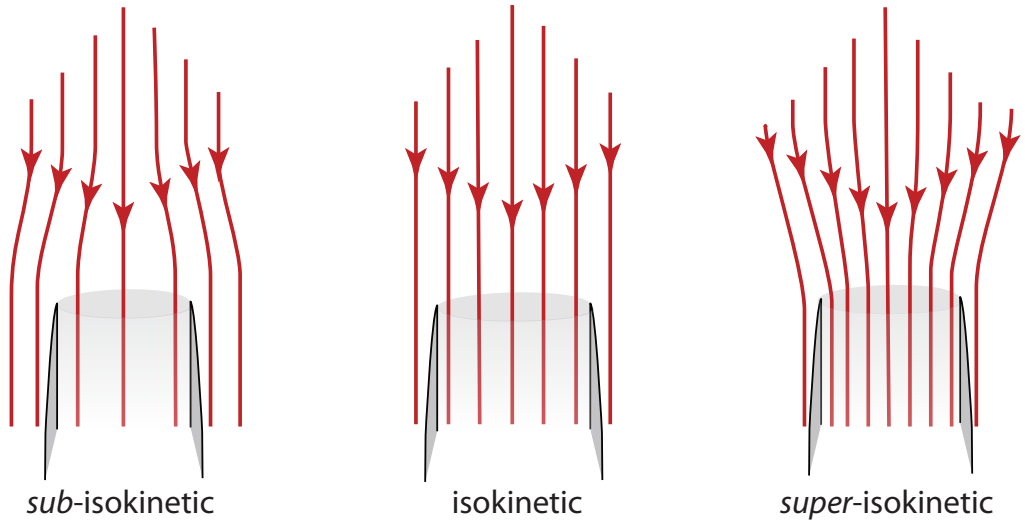

Figure 2.2: Three possible sampling regimes are shown. Under sub-isokinetic conditions the inlet velocity is less than the free-stream velocity generating a divergence at the inlet. Large particles tend to be over-sampled since they follow the initial streamlines. Under the super-isokinetic condition the inlet velocity exceeds the free-stream velocity, streamlines converge at the inlet and large particles are under-sampled. Only under the isokinetic conditions, where the inlet velocity is equivalent to the free-stream velocity, are particles sampled with equal efficiency regardless of size.

verge at the inlet and particles are under-sampled. Only under isokinetic conditions is the sampling efficiency for all particles unity as the inertial effect does not operate for streamlines that neither converge nor diverge.

2.2.5.2 Mechanical Description

Design considerations and the performance of the new total water inlet are discussed. Air, containing both condensed and vapor phase water, is sampled by a forward-facing inlet that extends 0.81 m from the surface normal of the port side pallet wall. A ram pressure design in conjunction with a rear-facing Venturi exhaust

generate bulk flow through the inlet (Fig. 2.1) with flow velocities of 20 – 25 m/s, measured at the pitot tube downstream of the detection pick-off. Only 15% of the total flow is diverted from the core, by the pick-off valve, to the detection axis.

2.2.5.2.1 Inlet Heaters & Particle Evaporation Accurate measurements of total water require that the condensed phase be completely converted to vapor prior to detection. The inlet was designed to completely vaporize particles during the transit time from the entrance of the inlet to the detection axis pick-off. A series of heaters (440 W total) along the primary duct provide sufficient heat to vaporize particles and establish a flow temperature of 30 °C near the detection pick-off: 80 W of heat are applied at the entrance of the inlet by two cartridge heaters and is controlled by a thermostat set to 0 °C; 180 W of heat are applied by a heating block at the first elbow and is controlled to 18 °C by a thermostat; 180 W from tape heaters (Minco) are applied along the remaining length of the duct until the detection pick-off and are actively controlled to maintain a flow temperature of 30 °C as measured by a thermistor behind the detection pickoff.

The rate of evaporation of a particle in a heated duct is limited by diffusion and the particle lifetime for complete evaporation can be calculated (Hinds, 1999):

$$t = \frac{R\rho_p d_p^2}{8D_v M\left(\frac{p_d}{T_d} - \frac{p_\infty}{T_\infty}\right)} \tag{2.22}$$

where R is the gas constant; ρ_p is the density of the particle; D_v is the diffusion coefficient of vapor in air; M is the molecular weight; p_d is the partial pressure; and T is the temperature. Subscripts p, d, and ∞ refer, respectively, to properties

of the bulk particle, at the particles surface and away from the particle (ambient). Equation 2.22 is valid for particles with diameters between 1 – 50 μm, for particles larger than 50 μm the evaporation rate is increased by an additional factor due to settling velocities (Hinds, 1999). An analysis by Weinstock et al. (2006) found that the lifetime for complete evaporation of a 1000 μm particle is on the order of 1.25 seconds for a duct held at 30 °C and at pressures characteristic of the upper troposphere (tropopause). Residence time for detection in our duct is on the order of 100 ms, when the aircraft is traveling with a typical 200 m s^{-1} cruise velocity, and thus it is expected that only particles with diameters less than 80 μm would fully evaporate. Occasionally particles over 900 μm were measured by the Cloud Imaging Probe (CIP) instrument, however, for the 8 August flight (discussed in Chapter 3), 90 % of the ice water content was contained in particles with diameters less than 400 μm.

While the above analysis predicts that residence time through the inlet duct is insufficient for complete evaporation of all sampled particles it must be noted that the model is conservative and does not fully reflect conditions throughout the duct. The flow temperature of 30 °C is characteristic of the core of the flow near the detection pick-off. A strong temperature gradient exist across the duct, with laboratory tests indicating wall temperatures approaching 60 °C. Duct temperatures of 60 °C would evaporate all particles with diameters less than 200 μm during the residence time to detection as calculated by Eq. 2.22. Computational fluid dynamics calculations show that a flow inversion between the core and the walls occurs at the elbows. Shattering of particles, especially larger particles, is expected to be

significant at the elbows where particles will maintain flow along inertial streamlines, despite the flow inversion, and impact the wall and shatter. Shattering artifacts will experience the highest temperatures at the wall which are in direct contact with heaters. Furthermore, the particle evaporation model is conservative in that it calculates the lifetime of spherical particles. Cirrus particles are often non-spherical, having larger surface area-to-volume ratios and, thus, would experience greater rates of evaporation.

It is important to note that incomplete conversion of the condensed phase to vapor would give erroneously low values for the ice water content of H_2O and HDO. However, with the assumption that the isotope ratio is consistent across the size distribution of particles sampled at any instant, the reported δD values for ice would be largely unaffected by incomplete evaporation. Here we explore the error constraints for incomplete conversion. With an average temperature of 30 °C for the flow, the equilibrium isotope effect (eq. 3.22) would give a maximum depletion of 9 % ($\delta D_{\text{max. error}} = -90$ ‰) for HDO relative to H_2O. The depletion error approaches 0 % with complete conversion of the condensed phase (see Sec. 3.2.3). In the absence of shattering the maximum amount of ice contained in particles larger than 80 μm is 46 %. Treating particles over this 80 μm threshold as completely unconverted gives a maximum depletion error of less than 4.1 %. If just 10 % of condensed phase were not converted to vapor then the depletion error would be less than 1 % ($\delta D_{\text{max. error}} = -10$ ‰).

There is no evidence for incomplete conversion of the condensed phase to vapor prior to sampling. This analysis is based on qualitative descriptions of processes

occurring in the duct and any errors that could result from incomplete evaporation of particles are impossible to quantify. To remove any doubt, or at a minimum to serve as a data quality diagnostic, the placement of a diode and detector across the duct near the pick-off in a future iteration would be invaluable. Backscatter ratios would indicate the presence of particles, although the condensed phase fraction could not be quantified.

2.2.5.3 Flow Control

A pitot tube located downstream of the detection pick-off is the only location where the flow velocity in the main inlet is measured. However, the flow velocity at the inlet can be calculated by applying the continuity equation for fluid flow. This application allows us to evaluate the performance of the isokinetic inlet during the field campaign.

2.2.5.3.1 Determining Flow Velocity at the Inlet The continuity equation for fluid flow states that the mass of an incompressible fluid flowing through an infinitesimal cross-sectional area must be constant,

$$\rho_1 v_1 A_1 = \rho_2 v_2 A_2. \tag{2.23}$$

Where ρ is the density of air, v the velocity and A the cross-sectional area at a given point along the duct.

The density of air can be calculated from the temperature, T, and pressure, p,

by using the equation of state,

$$\rho = \frac{Mp}{RT}, \tag{2.24}$$

where M is the molecular weight of air and R is the universal gas constant.

Combining Equations 2.23 and 2.24 allows for the velocity at the inlet to be determined in terms of the flow velocity measured by the pitot tube, v_{pitot}:

$$v_{inlet} = \frac{v_{pitot}\, p_{duct}\, T_{inlet}\, A_{duct}}{p_{inlet}\, T_{duct}\, A_{inlet}} \tag{2.25}$$

where the *duct* location refers to the position along the duct where the pitot tube and thermistor are located, and *inlet* refers most upstream point of the inlet where the sample enters the inlet. Ambient pressure and temperature measurements made by the Meteorological Measurement System (MMS) instrument are used as a proxy for those parameters at the location of the inlet. As no measurement of the free-stream velocity is possible we make the assumption that the aircraft's true air-speed, v_{tas}, is equivalent to the free-stream velocity.

2.2.5.3.2 Anisokinetic Errors The fraction of time the inlet velocity is within a given percentage of isokinetic sampling is evaluated in Figure 2.3. Ten second averaged data for the entire mission is represented by the cyan line. Included in this is data from the flight on 3 August 2007, which is considerably worse than for the remainder of the mission. Following the first flight (3 Aug), the gain of the PID-controller was increased to make the throttle valve more responsive to pressure fluctuations between the inlet and the free-stream. Removing this data results in a

significant decrease in anisokinetic error for a given time fraction, especially at the ±4 to ±6 percentage error range as shown by the magenta line. The data is further filtered to include only those points where the true air-speed of the aircraft is greater than 50 m s^{-1}, the static pressure is less than 450 mbar (roughly where altitude is greater than 6.25 km in the tropics), and where the absolute gradient in the pressure is less than 1.5 mbar s^{-1} which excludes regions of rapid ascent or descent; this is representative of conditions of sampling ice clouds in the TTL and further increases the time fraction in the same error range as is indicated by the black line.

2.2.6 Hoxotope Field Evaluation

2.2.6.1 Vapor Phase Measurements

Utilizing simultaneous water vapor measurements by the Harvard Lyman-α Water Vapor instrument (HWV) (Weinstock et al., 1990; Weinstock et al., 1994; Hintsa et al., 1999) serves not only as a means to determine ice water content but also provides an independent measure to evaluate the issue of contamination during sampling in regions of clear air and during transitions from clouds to clear air. Measurements made by Hoxotope in clear air regions can be directly compared with those made by HWV to evaluate its baseline accuracy in flight.

Comparison between the two instruments during regions of clear air provides a first-order evaluation of the accuracy of Hoxotope (HOX). While excellent agreement between the two instrument has been demonstrated in the past (St. Clair et al., 2008), the introduction of artifacts or a bias stemming from the new inlet or changes in longterm accuracy must be explicitly evaluated. For this analysis, clear air is

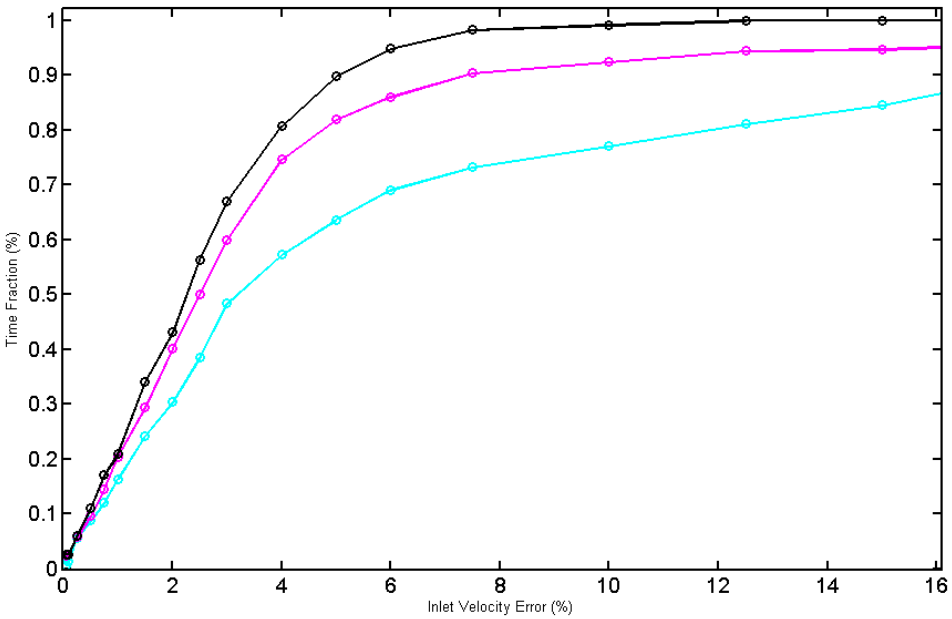

Figure 2.3: The fraction of the time the error in the inlet velocity is within a given percentage of isokinetic sampling is evaluated. Different filtering parameters are represented by the various lines: data for the entire mission is given by the cyan line; the magenta line excludes the data from 3 August 2007; the black line excludes the data from 3 August and, additionally, only includes data that is representative of sampling periods of ice (see text).

defined as regions where particle number concentrations are less than 250 L^{-1} in the 0.5 – 3.0 μm diameter range and ice water content is less than 4 ppm. The particle number concentration is taken from the Cloud and Aerosol Spectrometer (Baumgardner et al., 2001) and an independent ice water content is taken from the Colorado Laser Hygrometer (CLH) total water instrument (Davis et al., 2007). Additional constraints include: pressures less than 400 mbar as measured by MMS to exclude regions of ascent or descent, where water vapor is high and contamination from condensation in the inlet is known to occur, and water vapor less than 175 ppmv as measured by either Hoxotope or Lyman-α. Data above 175 ppmv were discarded due to the decrease in signal-to-noise in Hoxotope at high water vapor concentrations.

With these constraints a total of 2072 data points at 10 second resolution, corresponding to 19 % of the total data from the mission, are available for a regression between Hoxotope and Lyman-α. A regression which accounts for the uncertainty in both measurements demonstrates close agreement ($R^2 = 0.986$) between the instruments that spans three orders of magnitude; fit parameters reveal that measurements by Hoxotope are slightly less than Lyman-α (slope $= 0.9446 \pm 0.0024$) and there is very little bias (intercept $= -0.0095 \pm 0.0643$ ppm), with both parameters within the calibration uncertainties (± 5 %) of the instruments.

2.2.6.2 Total Water Measurements

While there is very good agreement between Hoxotope and HWV in clear air, there is much less agreement with the University of Colorado Laser Hygrometer (CLH) in regions of clouds. The CLH instrument suffers from baseline drift which

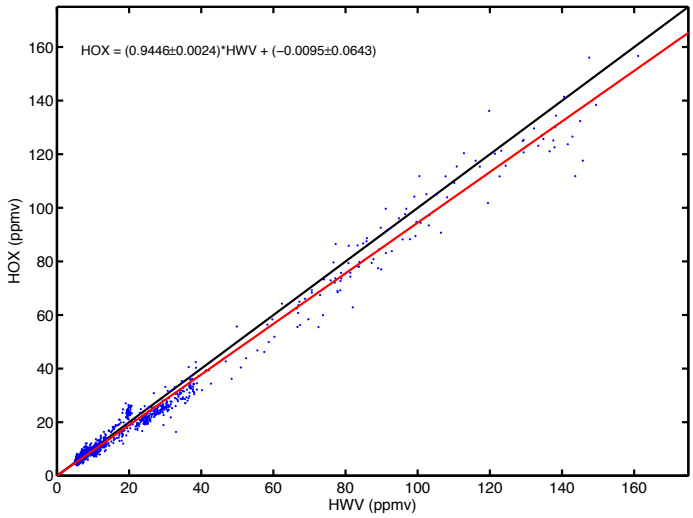

Figure 2.4: One-to-one comparison of clear air measurements made by Hoxotope and and Lyman-α during the TC4 mission. The agreement between instruments is within experimental error.

was manually removed from all the TC4 data. This baseline drift affects the ice water content (IWC) measurements less than 15 ppmv. However, removing the baseline drift did not significantly improve agreement between the instruments at low IWC. In general CLH reported larger IWC than Hoxotope for the TC4 mission.

2.2.6.3 Isotope Measurements Comparison

The ability to measure water isotopologues (H_2O & HDO) set Hoxotope and ICOS (see Sec. 2.3) apart from the other water instruments carried aboard the WB-57 during TC4. During the TC4 mission, ICOS flew in the second pallet, directly aft of Hoxotope, making measurements of vapor phase H_2O and HDO. These vapor phase measurements are required to determine the isotopic composition of ice par-

ticles encountered. ICOS data from TC4 is only available for two flights (8 and 9 August) providing a limited data set to analyze the isotopic composition of ice particles. To achieve this goal, we must have confidence in the vapor phase isotopologue measurements made by Hoxotope: this is investigated by intercomparison with ICOS during regions of the flight that are free from ice.

Figure 2.5(b) shows the percentage difference in δD measurements between Hoxotope and ICOS versus the potential temperature as recorded by MMS. The percentage difference for vapor phase measurements is shown in blue: the dashed vertical line corresponds to where there is no disagreement between the instruments, which is what is expected for vapor phase measurements. The disagreement between the instruments is within the uncertainty of both instruments below 410 K. Any deviation in these measurements outside of the instrument errors is an indication of the isotopic composition of the condensed phase. While the dataset available for comparison is limited to slightly more than 8.5 hours of flight time over the course of 2 days, the mostly complete dataset from the flight on 8 August provided sampling of significant convective activity in the Panama Bight and of TTL cirrus clouds. The only significant deviation of the isotopic composition of the condensed phase from the vapor phase occurs between 346 – 347 K.

2.2.7 Isokinetic Inlet Evaluation

2.2.7.1 Isokinetic Sampling

Isokinetic sampling was maintained at all sampling altitudes (Fig. 2.6) as evidenced by the near agreement between the flow velocity at the inlet and the free-

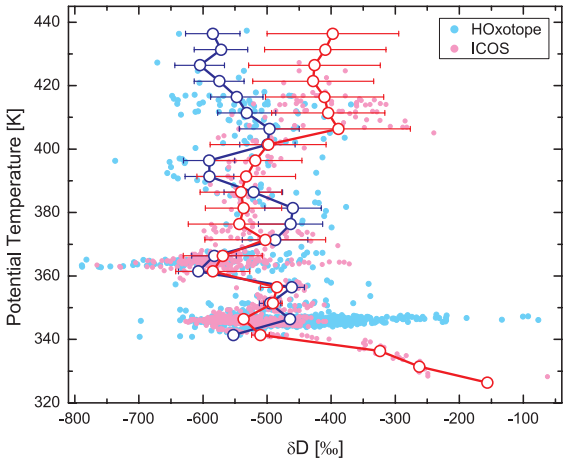

(a)

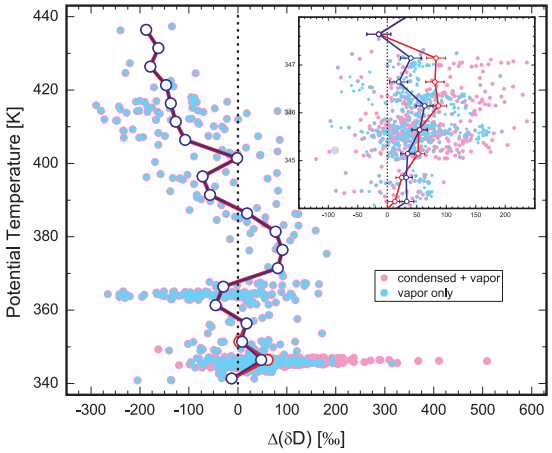

(b)

Figure 2.5: (a) Hoxotope (cyan) and ICOS (magenta) raw measurements and 5 K (θ) bins and instrumental uncertainties (blue and red, respectively) during TC4. Above 350 K, only vapor phase water is encountered and there is good agreement between the instruments. Above 420 K, disagreement between the instruments fall outside instrument uncertainty but data points are sparse. (b) Percentage difference between Hoxotope and ICOS in terms of vapor (blue & cyan) and total water (red & magenta). Significant disagreement is only seen near 345 K, when ice clouds from convective outflow were encountered.

stream velocity, taken as the true airspeed of the WB-57, as well as the constant zero differential pressure across the inlet for all pressures above 300 mbar. A small discrepancy between the two different measurements of true airspeed can be seen, especially at lower pressures, which is likely due to variations in the local flow and pressure fields around the aircraft. Sharp transitions in the differential pressure are found near 4.5, 4.8 and 5.4 $\times 10^4$ s and are the result of scanning the throttle valve across its range as part of inflight diagnostics. Data collected during these diagnostic periods are omitted from the final data set. Anisokinetic conditions observed for times less than 4.5 $\times 10^4$ s and greater than 5.9 $\times 10^4$ s correspond to periods of ascent and descent, respectively, and are likely attributable to a variation in the pressure field between the two ports of the differential pressure sensor as a result of the angle of attack.

2.2.7.2 Inlet Contamination

The issue of contamination as a result of water sticking to the walls of the inlet are addressed by additional comparison with HWV. A concern with the total water inlet is the potential for residual water to remain in the inlet after sampling in regions of high water, specifically when sampling in regions with water in the condensed phase. While the inlet heaters are designed to completely evaporate the condensed water prior to sampling, the potential for contamination exists during regions with high concentration of water in the condensed phase as a result of water that is retained in the inlet. Liquid water has a propensity to stick to surfaces, to reduce this problem the interior walls on the inlet were coated with FluoroPel (Cytonix Corporation), a

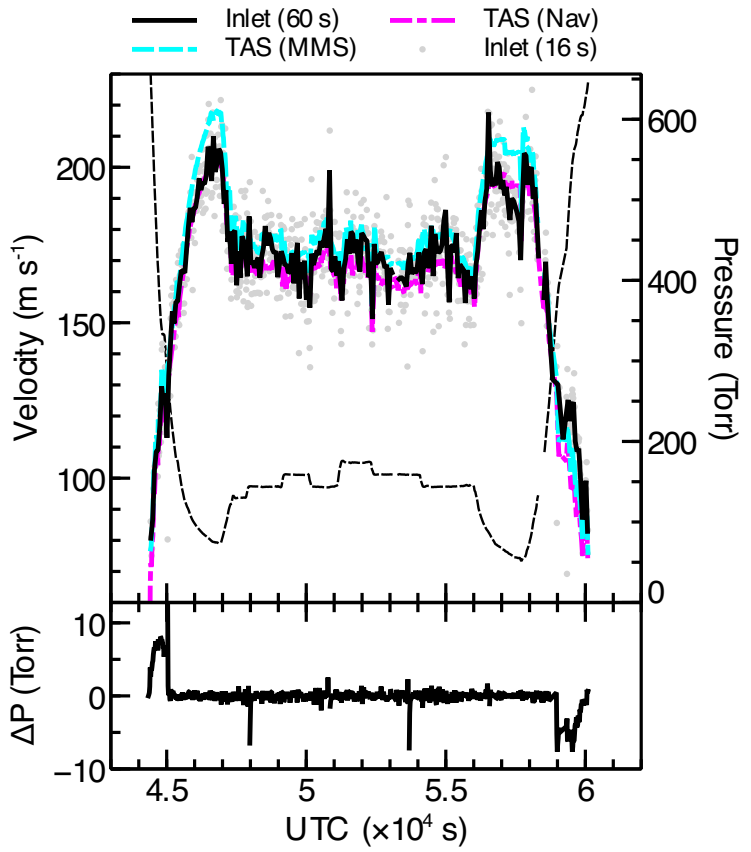

Figure 2.6: (upper panel) The instantaneous sixteen second data (grey circles) shows greater error than the sixty second averaged data (black line) because of the active PID-control of the throttle valve to maintain zero-differential static pressure between the inlet and the free-stream (i.e., isokinetic flow). Free-stream flow velocity is indicated by either the MMS (cyan dashed line) or the navigation system (magenta dashed line) true-air speed measurements; the isokinetic condition represents identical flow velocities at both the inlet and in the free-stream. Note the discrepancy between the reported true-air speed from the MMS and navigation systems, particularly at high velocity. (lower panel) Difference between static pressure of the inlet and ambient. Sampling errors with the static differential pressure of magnitude less than zero are representative of super-isokinetic sampling ($v_{inlet} > v_{free-stream}$), while sampling errors with magnitude greater than zero are representative of sub-isokinetic sampling ($v_{inlet} < v_{free-stream}$).

hydrophobic coating. Additionally, to minimize the potential for water to remain in the inlet, sections of the inlet were designed to fit together whilst eliminating dead volume.

Wall contamination, or hysteresis, is investigated by evaluating the time response of HOX with respect to HWV when transitioning from regions containing condensed water to clear air, as shown in Fig. 2.7. HWV operates in a higher flow rate regime (50 – 70 m s^{-1}) than HOX (15 – 25 m s^{-1} in the duct at the pitot tube) where outgassing from the walls and residual water hysteresis effects have been demonstrated as not being an issue (Weinstock et al., 1994). The flight of 8 August 2007 provides several regions to investigate the potential wall contamination in the HOX inlet when moving between regions of high condensed water and clear air.

In Fig. 2.7, total water (HOX) and water vapor measurements (HWV) are shown (top panel) in a time series plot. Simultaneous ice water content (IWC) and particle concentrations in the 0.5 – 3.0 μm diameter range are shown by the semi-log plot in the lower panel. Several regions exist during the flight where a sharp transition occurs between clouds and clear air, notable occurrences can be seen near 4.93 $\times 10^4$, 5.35 $\times 10^4$, 5.4 $\times 10^4$, and 5.6 $\times 10^4$ seconds. The regions near 4.93 $\times 10^4$ and 5.6 $\times 10^4$ seconds are explored in detail in Fig. 2.7 (b) and (c), respectively. Fig. 2.7(b) illustrates a transition from a region of high concentration of condensed water (400 ppm) to a region of relatively high vapor but is nearly ice free as indicated by the particle number concentration recorded by CAS. While the transition is gradual to the ice free region at 4.96 $\times 10^4$ seconds, the rate of decrease of enhanced water, that is the contribution from the condensed phase, relative to HWV qualitatively tracks

very closely with CLH. Fig. 2.7(c) provides compelling evidence that sampling errors due to wall contamination is not an issue. Near 5.61 $\times 10^4$ seconds the aircraft made a sharp transition from a cloud region to a very dry clear air region. IWC content derived by the difference between HOX and HWV show a maximum of about 140 ppm in Fig. 2.7(c) prior to the transition into clear air. Both CLH IWC and CAS particle concentrations show that the transition into clear air is abrupt and occurs at 5.61 $\times 10^4$ seconds. At this transitional period, the enhancement in Hoxotope's total water (due to condensed phase water) diminishes at a rate comparable to both CLH and particle concentration. The CAS instrument contains an open path imaging probe, so wall contamination and hysteresis are not an issue. As the aircraft moves into the ice free region, Hoxotope matches HWV measurements and indicates no delay as a result from wall contamination.

2.3 ICOS Isotopologue Instrument

The Integrated Cavity Output Spectroscopy (ICOS) instrument has been previously described (Sayres et al., 2009) in a configuration nearly identical to that during the TC4 mission. A complete description of the instrument is not presented, however the development of the theory of the ICOS technique is presented and is done for reasons twofold.

Firstly, in order to model the evolution of light inside an optical cavity and to develop the theory of the ICOS, cavity ringdown spectroscopy must be introduced. While cavity ringdown spectroscopy is the progenitor to ICOS and must be intro-

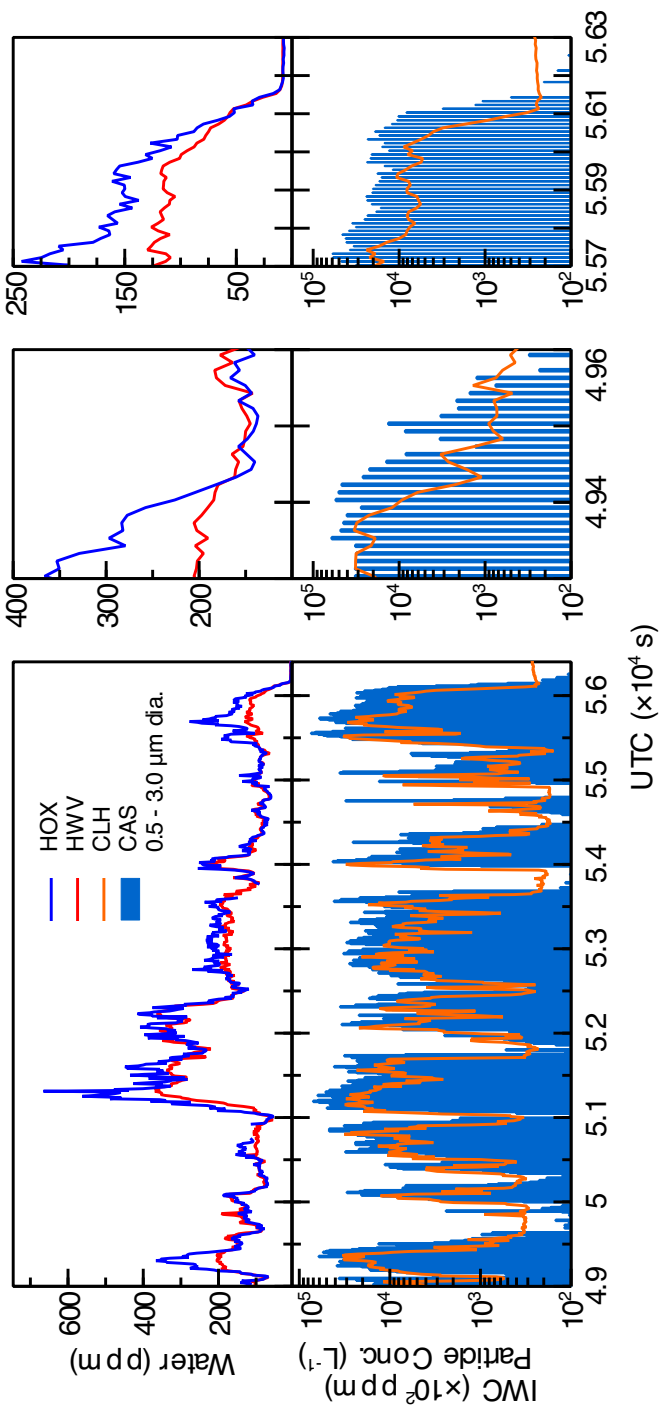

Figure 2.7: The transition between cloud and ice-free regions is shown for the 7 August 2007 flight (left-panel). Two regions are looked in closer detail to investigate possible contamination. The transition from a cloud region with a high-water content ($\sim$ 350 ppmv) to an ice-free region with a high water vapor content ($\sim$ 150 ppmv) shows no contamination in Hoxotope as the particle number concentration falls by over an order of magnitude (center-panel). Near the end of the flight, a sharp transition from an ice-cloud region with high-water content (total water $\approx$ 250 ppmv; vapor $\approx$ 175 ppmv) to a very dry ice-free region ($<$ 10 ppmv) shows no contamination artifacts in Hoxotope (right-panel).

duced in that regard, it must also be discussed as it is used as a calibration technique in both the glyoxal and iodine monoxide instruments. Specific details relevant to calibration are discussed in later chapters.

Secondly, ICOS results from the use of continuous wave (CW) lasers combined with a cavity enhanced techniques. This generates long effective path lengths, making the sensitive detection of water isotopologues at the low mixing ratios of the upper troposphere and lower stratosphere with a direct absorption technique possible. This technique is not limited to the detection of water and therefore a discussion of the theoretical aspects of this technique are applicable to the development of future instruments.

2.3.1 Measurement Technique: Application of Absorption Spectroscopy to Trace Gas Detection

Absorption spectroscopy probes vibrational transitions within molecules which induce a change in the dipole moment. The technique is therefore extremely useful due to its ability to differentiate molecular species on the basis of their quantum mechanical properties. Not only are molecular species discriminated but so too are molecules whose atomic composition differ by a single isotope (isotopologues)—a physical manifestation of the role that mass plays at quantum level.

This spectroscopic technique identifies and measures the concentration of a molecular species by the measurement of the change in intensity of a source of radiation as it passes through a medium containing an absorber as function of the frequency of the source. The change in intensity of the source as it interacts with an absorber

is directly related to the concentration of the absorber by the Beer-Lambert Law:

$$I(\nu) = I_0(\nu)e^{-\sigma(\nu)lN} = I_0(\nu)e^{-\alpha(\nu)l} \tag{2.26}$$

where I_0 and I are the incoming and outgoing intensities of the radiation passing through a sample, $\sigma(\nu)$ is the frequency-dependent absorption cross-section, l the path length that the absorber is present over, and N the number density of the absorber. It is common to take the product of the absorption cross-section and the number density giving the frequency-dependent absorption coefficient, $\alpha(\nu)$.

The concentration C in units molecules cm^{-3} is related to the absorption coefficient via the physical relationship

$$\alpha(\nu) = C\,\frac{S_{\eta\eta'}}{\sqrt{\pi/\ln(2)}\,\gamma_D}K(\nu,\, \nu_{\eta\eta'},\, \gamma_L/\gamma_D) \tag{2.27}$$

where $S_{\eta\eta'}$ is the spectral line intensity for a transition between states η and η' in cm^{-1} (molecules $\mathrm{cm}^{-2})^{-1}$, γ_D and γ_L are the Doppler and Lorenztian half-widths at half maximum (HWHM), respectively, and K is the Voigt lineshape function. The Voigt lineshape results from the convolution of independent Doppler and Lorentzian line broadening mechanisms (Armstrong, 1967).

The ultimate sensitivity of this technique lies in the ability to separate a small change in the intensity from noise, optical noise in the radiation source and electrical noise in the detector, in the limit of weak absorbances (low optical depths). When probing molecular species with low concentrations and/or weak transition line intensities (absorption cross-sections) the sensitivity of the measurement can be im-

proved by increasing the path length. Large increases in the effective path length over which the radiation interacts with the absorber can be achieved with the use of high-finesse optical cavities. Recent developments in mirror coatings allowing for high reflectivities in the infrared have driven developments in enhanced absorption techniques.

2.3.1.1 Cavity Ringdown Spectroscopy

ICOS spectroscopy stems from the development of cavity ringdown spectroscopy by utilizing a continuous wave laser light source instead of a pulsed laser. The theory of cavity ringdown is developed here prior to a discussion of ICOS for this reason. Moreover, both glyoxal and IO instruments are calibrated by the cavity ring-down spectroscopy technique so this discussion is relevant to both these instruments and will be referred to in later chapters.

Cavity ringdown spectroscopy (CRDS) utilizes an optical cavity formed by two highly reflective mirrors in order to generate extremely long effective path lengths to detect gas phase species. This spectroscopic technique differs from traditional absorption measurements in that the decay time of the signal is measured rather than the change in intensity of light source.

Consider an instantaneous pulse of light that enters a cavity, with an initial intensity I_0, formed by two highly-reflective mirrors ($R = 0.9998$, as an example) separated by a distance L. A detector placed behind one of the mirrors (here termed the *exit mirror*) of the cavity allows the decay of light within the cavity to be monitored as it slowly leaks out. As the pulse traverses the cavity it loses 200 parts per

million (ppm) of its initial intensity every time it hits a mirror. The intensity of light transmitted to the detector, T_{det}, upon reflection is simply given by the portion that is not reflected by the mirrors

$$T_{det} = I(1 - R). \tag{2.28}$$

The amount of light that falls on the detector can then be calculated each time the pulse hits the exit mirror by equation 2.28 as long as the incoming intensity is known.

The intensity of the incoming pulse before each reflection by the exit mirror n is related to the previous intensity prior to a round-trip within the cavity

$$\begin{aligned} I_1 &= I_0 \\ I_2 &= I_0 R^2 \\ I_3 &= I_2 R^2 = I_0 R^4 \\ &\vdots \\ I_n &= I_{n-1} R^2 = I_0 R^{2(n-1)} \end{aligned} \tag{2.29}$$

where I_0 is the intensity which entered the cavity. The detector would measure a series of discrete pulses, each with an intensity

$$I_{n,\,det} = I_0 R^{2(n-1)}(1 - R) \tag{2.30}$$

with each pulse separated by the round-trip travel time of 6 nanoseconds. Most detectors can not resolve the individual pulses and instead record the exponential

decay envelope as shown in Figure 2.8.

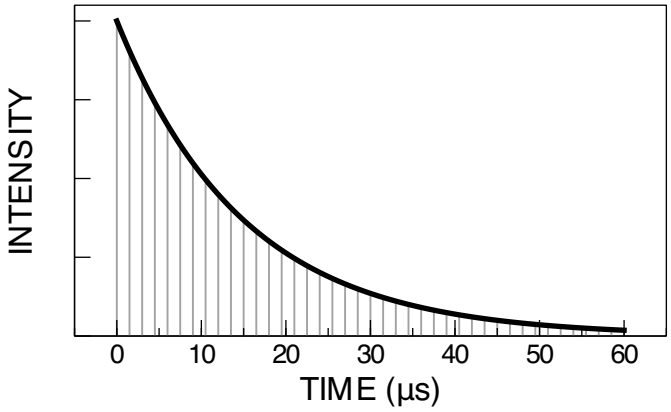

Figure 2.8: The expected decay profile for an instantaneous pulse which enters a cavity formed by two highly-reflective mirrors ($R = 0.9998$) and separated by 90 cm, and is termed cavity ringdown. Only every 250^{th} round trip of the pulse is plotted for clarity. The exponential decay envelope as measured by a detector is shown by the black line.

Since only the decay envelope is measured by a detector this technique can be extended beyond instantaneous pulses to light sources that have finite pulse-widths. If the only loss pathway for the pulse of light out of the cavity is through the mirrors then the average amount of time that light is trapped in the cavity is dependent only on the length of the cavity L and the mirrors' reflectivity R,

$$\tau = \frac{L}{c(1-R)} \tag{2.31}$$

where c is the speed of light and τ is termed the *cavity time constant*.

If an absorbing molecular species is introduced into the cavity there is an additional mechanism for the loss of light as the pulse traverses the cavity. The cavity

time constant is decreased and equation 2.31 is modified to account for the intracavity absorption,

$$\tau = \frac{L}{c[1 - R + \alpha(\nu)L]} \tag{2.32}$$

where $\alpha(\nu)$ is the frequency dependent absorption coefficient of the molecular species and L is the path length. If the decay of light, τ, is measured as a function of the laser frequency, ν, an absorption spectrum is generated.

2.3.1.2 Integrated Cavity Output Spectroscopy

The use of a continuous wave (CW) laser necessitates additional analysis to account for the fact light is continuously entering the cavity as its decay is simultaneously being monitored. Three factors control the intensity of light in the cavity: the transmission of light through the mirrors; the amount of time that the light is allowed to build up inside the cavity; and the loss of light through the cavity mirrors or by molecular absorption. If the laser's frequency is scanned at a rate comparable to the cavity time constant, at any time there are multiple frequencies of light in the cavity, each decaying with their own time constant $\tau(\nu)$.

The evolution of light in the cavity can be modeled (Sayres et al., 2009) by considering the intensity of light inside the cavity as a function of time. The intensity of light that builds up in the cavity from time t' to time $t' + \Delta t$ is

$$\begin{aligned} I_{t' \to t'+\Delta t} &= \int_0^{\Delta t} P(t') T e^{-t/\tau(t')}\, dt \\ &= P(t') T \tau(t') \left[1 - e^{-\Delta t/\tau(t')}\right] \end{aligned} \tag{2.33}$$

where T is the transmission of the mirror and Δt is small enough that the power emitted by the laser $P(t')$ and the decay time constant $\tau(t')$ can be assumed to be constant in the interval between t' and $t + \Delta t$. The terms before the bracket in equation 2.33 describe how much of the laser power gets transmitted into the cavity, and the exponential term accounts for the characteristic ringing-up of light in the cavity as seen in Figure 2.9(a). After a period of 2τ the intensity of light in the cavity will have grown past 86 % of its maximum value.

While light is continuously entering the cavity during the interval characterized by Δt, it is also being lost through the mirrors or by molecular absorption. The intensity of light at some future point in time t is therefore a convolution of the ring-up (eq. 2.33) and ring-down $\left(I = I_o e^{-t/\tau}\right)$ intensities, yielding a model that fully accounts for the evolution of light within the cavity

$$I_{t' \to t'+\Delta t}(t) = P(t')T\tau(t')\Big[1 - e^{-\Delta t/\tau(t')}\Big]e^{-(t-t')/\tau(t')}. \tag{2.34}$$

Both the laser power P and the cavity time constant τ are dependent on when the light entered the cavity since the laser is being scanned and the frequency of light is thereby time-dependent.

The intensity of light that exits the cavity $I_{out}(t)$ at any instant in time and falls on the detector is determined by summing equation 2.34 for all previous times

$$I_{out}(t) = \sum_{t'=-\infty}^{t} \tfrac{1}{2}P(t')T^2\tau(t')\Big[1 - e^{-\Delta t/\tau(t')}\Big]e^{-(t-t')/\tau(t')} \tag{2.35}$$

where the additional factor of T is due to the additional transmission of light through

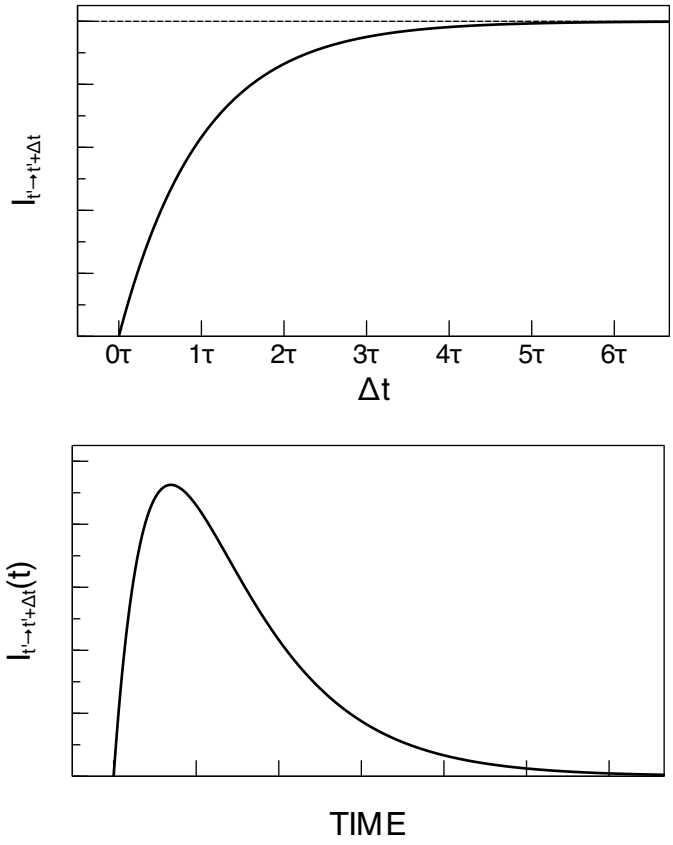

Figure 2.9: (a) For a continuous wave laser, light slowly leaks into the cavity (cavity ringup). The relative intensity of light which enters the cavity is a function of the amount of time that the laser is on (or remains at a single frequency) until saturation is reached. The saturation intensity is determined by the mirrors reflectivity and the laser power. (b) The evolution of light in cavity is a convolution of cavity ringup and cavity ringdown and has the characteristic shape that is shown.

the exit mirror before being recorded on a detector and the factor of 1/2 accounts for the fact that light escapes from both mirrors equally although the detector only samples the transmission through one mirror. The discretization of the output spectrum, as in equation 2.35, is the most useful method for fitting data acquired at discrete sample times (Sayres et al., 2009).

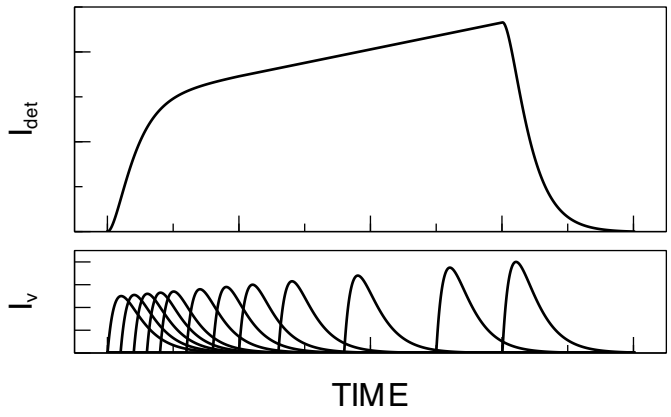

Figure 2.10: (upper) A simulated output spectrum in the absence of an absorber. The lasers power is not constant with frequency but instead ramps. (lower) The evolution of single frequencies (arbitrarily spaced for clarity) are shown as the laser scans across its range. The integrated output measured by the detector is just the sum all the frequencies in the cavity at any instant in time. Absorption features result from a modified ringdown time constant.

Equation 2.35, which is illustrated in Figure 2.10, can be written in matrix form:

$$\begin{matrix} P_1 & P_1\tau_1^* & P_1\tau_1^{*^2} & P_1\tau_1^{*^3} & P_1\tau_1^{*^4} & \dots \\ 0 & P_2 & P_2\tau_2^* & P_2\tau_2^{*^2} & P_2\tau_2^{*^3} & \\ 0 & 0 & P_3 & P_3\tau_3^* & P_3\tau_3^{*^2} & \\ 0 & 0 & 0 & P_4 & P_4\tau_4^* & \\ 0 & 0 & 0 & 0 & P_5 & \\ \vdots & & & & & \ddots \end{matrix} \tag{2.36}$$

with $\tau^* \equiv e^{-dt/\tau}$ defined as the fractional loss per unit time, and τ is defined in equation 2.32, and P_ν the power at a particular frequency in the cavity. The row elements of the matrix represent the evolution of a single frequency in the cavity (i.e. Figure 2.10, lower-panel) and the sum of each column represents the total intensity of light in the cavity at any instant in time (i.e. Figure 2.10, upper-panel).

Each sampling time step dt_i represents the decay of multiple frequencies of light $\nu_{i_{1,\,2,\,\dots,\,n}}$ which can be represented by a single average frequency ν_i of the group. The signal that falls on the detector at any time (Figure 2.10, upper-panel) is just the sum of the decay profiles of each frequency of light present in the cell (Figure 2.10, lower-panel).

2.3.2 Hardware Overview

2.3.2.1 Optical Components & Layout

2.3.2.1.1 Quantum Cascade Lasers ICOS would not be a suitable technique for airborne measurements without the parallel advancements in compact solid state laser systems. At the heart of the ICOS optical system are quantum cascade lasers (QCLs) which were originally developed for use in fiber-optic telecommunication systems. QCLs were first demonstrated in 1994 at Bell Labs (Faist et al., 1994) and have become widely used in spectroscopic applications due to their broad gain profiles, high power and narrow linewidths. The novelty of QCLs and the revolution in optics and materials that they embody merits discussion.

Traditional semiconductor (diode) lasers rely on electron-hole pair recombinations to generate photons and therefore the frequency of the emitted light is determined by the energy of the band gap of the semiconductor: $\nu \approx E_g/h$, where E_g is the band gap energy and h is Planck's constant. Diode lasers are ubiquitous and, despite the simplicity of their operating principles, have been difficult to extend into wavelengths suitable for infrared absorption spectroscopy (> 2 μm) due to technical considerations relating to band gap material properties and temperature stabilities (Curl et al., 2010).

QCLs operate on an entirely different physical principle to generate photons, bypassing the restrictions faced by diode lasers, and operate in the mid- and far-infrared (3–24 & 60–300 μm). The radical design of a QCL relies on electrons undergoing quantum jumps between energy levels E_n and E_{n-1} in the active region of a semiconductor creating a photon of frequency $\nu = (E_n - E_{n-1})/h$. These energy levels are

not intrinsic to the semiconductor material but are artificially created by depositing material into the band gap region of nanometer thickness and generating quantum well structures. Photons are generated by the transition of an electron between quantized energy states within a well structure, not across the band gap as in diode lasers, and remain in the conduction band after emitting a photon. An electron can then tunnel into a neighboring well, emitting an additional photon, and so on. The cascade of photons by the recycling of electrons across quantum well structures is responsible for the high optical powers produced by these lasers.

2.3.2.1.2 Off-Axis Benefits Complications arise if the laser is aligned along the axis of the cavity as this configuration allows for a resonant coupling between the modes of the cavity and the laser's frequency whenever a half-integer ($n/2,$ for $n = 1,\ 2,\ 3\ldots$) number of wavelengths between the mirrors are satisfied. The power in the cavity is much larger during resonant conditions than non-resonant conditions, this is reflected in the output intensity as an oscillation that obscures absorption features. The optical cavity is effectively behaving as a free space etalon (Paul et al., 2001) and the spacing between modes is given by the free spectral range of the cavity (FSR) and is only dependent on its length L

$$\mathrm{FSR} = \frac{c}{2L} \tag{2.37}$$

where c is the speed of light. For a 1 meter mirror spacing the FSR of the cavity is 150 MHz and a typical laser linewidth is about 5 MHz. This can be overcome by injecting the laser into the cavity off-axis so that multiple passes are required

before the beam becomes reentrant, thereby increasing the effective path length of the cavity and subsequently decreasing its free spectral range such that multiple cavity modes are excited within the linewidth of the laser. However, since the beam is Gaussian in shape some overlap occurs before the beam is totally reentrant and produces cavity etalons. These can be minimized by scanning the laser at a rate comparable to the cavity time constant so that the time that the resonant condition is met is limited. This comes at the expense of high-speed acquisition and spectral fitting electronics.

2.3.2.2 Sampling

Ambient air is drawn into ICOS from a rear-facing inlet, preventing the uptake of the condensed phase. Air is drawn into the sampling cell by an identical vacuum pump (Varian TriScroll 600 dry pump) as that used on Hoxotope. The pressure in the cell is regulated by the same pinch valve assembly used by Hoxotope, where downstream pressure is modified by deforming a tube and thereby changing the conductance. This minimizes dead volumes and removes the possibility of contamination by retained water. A heated inlet minimizes any potential condensation and maintains a constant temperature (25 ± 0.5 °C) of the sampled air.

2.3.2.3 Calibration

The accuracy of any absorption technique relies on how well the absorption line can be fit to equation 2.27 and on how accurately $S_{\eta\eta'}$ is known. Most of the spectroscopic line parameters in equation 2.27 can be taken from the HITRAN database

(Rothman et al., 2009). Considering the importance of the line parameters, as well as the uncertainty in their temperature and pressure dependencies, a careful laboratory calibration procedure is critical to accurately measure water vapor with the ICOS technique.

ICOS utilizes a similar calibration procedure as Hoxotope where saturated air is added to a dry bulk flow via a glass frit bubbler system. By adding known amounts of H_2O and HDO into the cell, corrections to the line parameters can be made that reflect the conditions inside the sampling cell.

References

G. Audi and A. Wapstra. The 1993 atomic mass evaluation: (I) Atomic mass table. *Nuclear Physics A*, 565(1):1–65, 1993. doi: 10.1016/0375-9474(93)90024-R.

G. Audi and A. Wapstra. The 1995 update to the atomic mass evaluation. *Nuclear Physics A*, 595(4):409–480, 1995. doi: 10.1016/0375-9474(95)00445-9.

D. Baumgardner, H. Jonsson, W. Dawson, D. O'Connor, and R. Newton. The cloud, aerosol and precipitation spectrometer: A new instrument for cloud investigations. *Atmospheric Research*, 59:251–264, 2001.

R. Curl, F. Capasso, C. Gmachl, A. Kosterev, B. McManus, R. Lewicki, M. Pusharsky, G. Wysocki, and F. Tittel. Quantum cascade lasers in chemical physics. *Chemical Physics Letters*, 487(1-3):1–18, 2010.

S. M. Davis, A. G. Hallar, L. M. Avallone, and W. Engblom. Measurement of Total Water with a Tunable Diode Laser Hygrometer: Inlet Analysis, Calibration Procedure, and Ice Water Content Determination. *Journal of Atmospheric and Oceanic Technology*, 24:463, 2007. doi: 10.1175/JTECH1975.1.

J. R. de Laeter, J. K. Böhlke, P. De Bièvre, H. Hidaka, H. S. Peiser, K. J. R. Rosman, and P. D. P. Taylor. Atomic weights of the elements. Review 2000 (IUPAC Technical Report). *Pure Appl. Chem.*, 75(6):683–800, 2003. doi: 10.1351/pac200375060683.

J. Faist, F. Capasso, D. Sivco, C. Sirtori, A. Hutchinson, and A. Cho. Quantum Cascade Laser. *Science*, 264(5158):553–556, 1994. doi: 10.1126/science.264.5158.553.

H. Fuchs, B. Bohn, A. Hofzumahaus, F. Holland, K. D. Lu, S. Nehr, F. Rohrer, and A. Wahner. Detection of HO_2 by laser-induced fluorescence: calibration and interferences from RO_2 radicals. *Atmospheric Measurement Techniques Discussions*, 4 (1):1255–1302, 2011. doi: 10.5194/amtd-4-1255-2011.

W. C. Hinds. *Aerosol technology: properties, behavior, and measurement of airborne particles*. Wiley-Interscience. Wiley, second edition, 1999.

E. J. Hintsa, E. M. Weinstock, J. G. Anderson, R. D. May, and D. F. Hurst. On the accuracy of in situ water vapor measurements in the troposphere and lower stratosphere with the Harvard Lyman-α hygrometer. *Journal of Geophysical Research*, 104:8183–8190, 1999. doi: 10.1029/1998JD100110.

D. Johnson, K. Jucks, W. Traub, and K. Chance. Isotopic composition of stratospheric water vapor- implications for transport. *Journal of Geophysical Research*, 106:12, 2001.

M. J. Kurylo. Absolute rate constants for the reaction H + O2 + M $\rightarrow$ HO_2 + M over the temperature range 203–404 K. *The Journal of Physical Chemistry*, 76 (24):3518–3526, 1972. doi: 10.1021/j100668a002.

J. Paul, L. Lapson, and J. Anderson. Ultrasensitive absorption spectroscopy with a high-finesse optical cavity and off-axis alignment. *Applied Optics*, 40(27):4904–4910, 2001.

L. S. Rothman, I. E. Gordon, A. Barbe, D. C. Benner, P. F. Bernath, M. Birk, V. Boudon, L. R. Brown, A. Campargue, J.-P. Champion, K. Chance, L. H. Coudert, V. Dana, V. M. Devi, S. Fally, J.-M. Flaud, R. R. Gamache, A. Goldman, D. Jacquemart, I. Kleiner, N. Lacome, W. J. Lafferty, J.-Y. Mandin, S. T. Massie, S. N. Mikhailenko, C. E. Miller, N. Moazzen-Ahmadi, O. V. Naumenko, A. V. Nikitin, J. Orphal, V. I. Perevalov, A. Perrin, A. Predoi-Cross, C. P. Rinsland, M. Rotger, M. Šimečková, M. A. H. Smith, K. Sung, S. A. Tashkun, J. Tennyson, R. A. Toth, A. C. Vandaele, and J. Vander Auwera. The HITRAN 2008 molecular spectroscopic database. *Journal of Quantitative Spectroscopy and Radiative Transfer*, 110:533–572, June 2009. doi: 10.1016/j.jqsrt.2009.02.013.

S. P. Sander, B. J. Finlayson-Pitts, R. R. Friedl, D. M. Golden, R. E. Huie, H. Keller-Rudek, C. E. Kolb, M. J. Kurylo, M. J. Molina, G. K. Moortgat, V. L. Orkin, A. R. Ravishankara, and P. H. Wine. *Chemical Kinetics and Photochemical Data for Use in Atmospheric Studies, Evaluation Number 15*. Jet Propulsion Laboratory, Pasadena, CA, 2006.

D. S. Sayres, E. J. Moyer, T. F. Hanisco, J. M. S. Clair, F. N. Keutsch, A. O'Brien, N. T. Allen, L. Lapson, J. N. Demusz, M. Rivero, T. Martin, M. Greenberg, C. Tuozzolo, G. S. Engel, J. H. Kroll, J. B. Paul, and J. G. Anderson. A new cavity based absorption instrument for detection of water isotopologues in the upper troposphere and lower stratosphere. *Review of Scientific Instruments*, 80 (4):044102, 2009. doi: 10.1063/1.3117349.

N. Shafer, S. Satyapal, and R. Bersohn. Isotope effect in the photodissociation of HDO at 157.5 nm. *Journal of Chemical Physics*, 90:6807–6808, June 1989. doi: 10.1063/1.456302.

J. M. St. Clair, T. F. Hanisco, E. M. Weinstock, E. J. Moyer, D. S. Sayres, F. N. Keutsch, J. H. Kroll, J. N. Demusz, N. T. Allen, J. B. Smith, J. R. Spackman, and J. G. Anderson. A new photolysis laser-induced fluorescence instrument for the detection of H_2O and HDO in the lower stratosphere. *Review of Scientific Instruments*, 79(6):064101, June 2008. doi: 10.1063/1.2940221.

K. L. Steffens and D. R. Crosley. Vibrational energy transfer in OH $A^2\Sigma^+$ between 195 and 295 K. *Journal of Chemical Physics*, 112:9427–9432, June 2000. doi: 10.1063/1.481562.

G. L. Vaghjiani and A. R. Ravishankara. Quenching of OD ($A^2\Sigma^+$, $v' = 0$ and 1) by various gases. *Journal of Chemical Physics*, 87(12):7050–7058, 1987.

E. Weinstock, E. Hintsa, A. Dessler, J. Oliver, N. Hazen, J. Demusz, N. Allen, L. Lapson, and J. Anderson. New fast-response photofragment fluorescence hygrometer for use on the NASA ER-2 and the Perseus remotely piloted aircraft. *Review of Scientific Instruments*, 65(11):3544–3554, NOV 1994.

E. M. Weinstock, J. J. Schwab, J. B. Nee, M. J. Schwab, and J. G. Anderson. A cryogenically cooled photofragment fluorescence instrument for measuring stratospheric water vapor. *Review of Scientific Instruments*, 61:1413–1432, May 1990. doi: 10.1063/1.1141198.

E. M. Weinstock, J. B. Smith, D. Sayres, J. R. Spackman, J. V. Pittman, N. Allen, J. Demusz, M. Greenberg, M. Rivero, L. Solomon, and J. G. Anderson. Measurements of the Total Water Content of Cirrus Clouds. Part I: Instrument Details and Calibration. *Journal of Atmospheric and Oceanic Technology*, 23:1397, 2006. doi: 10.1175/JTECH1928.1.

P. O. Wennberg, R. C. Cohen, N. L. Hazen, L. B. Lapson, N. T. Allen, T. F. Hanisco, J. F. Oliver, N. W. Lanham, J. N. Demusz, and J. G. Anderson. Aircraft-borne, laser-induced fluorescence instrument for the in situ detection of hydroxyl and hydroperoxyl radicals. *Review of Scientific Instruments*, 65:1858–1876, June 1994. doi: 10.1063/1.1144835.

J. Z. Zhang, D. G. Imre, and J. H. Frederick. HOD spectroscopy and photodissociation dynamics — selectivity in OH/OD bond breaking. *Journal of Physical Chemistry*, 93(5):1840–1851, March 9 1989.

Chapter 3

Measurements of the Isotopic Composition of Ice and Vapor Above a Tropical Convective Cell

> And the hooded clouds, like friars,
> Tell their beads in drops of rain...
>
> *Midnight Mass for the Dying Year*
> Henry Wadsworth Longfellow

3.1 Introduction

Water plays a critical role in the climate system by exerting an influence on the dynamic and radiative balance of the upper troposphere and lower stratosphere (UT/LS). Stratospheric water vapor concentrations impact surface dosages of UV radiation by influencing reactions which catalytically destroy stratospheric ozone (Dvortsov and Solomon, 2001; Kirk-Davidoff et al., 1999). Water vapor not only regulates the radiative balance (Smith et al., 2001; Shindell, 2001; Minschwaner and Dessler, 2004) of the UT/LS but changes in the concentration of water vapor contribute disproportionately to the radiative imbalance of the region by amplifying carbon dioxide and methane forcing, primarily through the associated cloud feedback (Solomon, 2007; Stephens, 2005).

It is understood that the bulk of air enters the stratosphere in the tropics (Holton et al., 1995) although the details of the mechanisms that control the humidity of the region are not fully understood (Rosenlof, 2003). Models that accurately describe the distribution of water vapor in this region by synoptic-scale meteorology and simple microphysical assumptions (Bonazzola and Haynes, 2004; Fueglistaler et al., 2004; Fueglistaler and Haynes, 2005) are at odds with the observed $HDO/H_2^{16}O$ ratios (Moyer et al., 1996; Johnson et al., 2001b). Any model that attempts to explain water mixing ratios in the UT/LS is burdened by the quantitative constraints of the isotopic composition of water. Reliable long-term climate forecasts rely on accurate descriptions of the exact nature of the response of water in the UT/LS to climate forcing and, as such, quantifying the influence of convection remains a first-order problem.

Considering the importance of ice lofting in TTL mixing models, the δD of ice has been a relatively unconstrained parameter. Previous measurements of the isotopic composition of total water (combined condensed and vapor phases) in the subtropics showed ice-laden air with a wide range of values between -400 ‰ and 0 ‰ (Webster and Heymsfield, 2003). In this paper we present direct measurements of the isotopic composition of ice above a large tropical convective cell during the boreal summer. A simple isotopic physics model is developed to determine the origin of the observed ice clouds. Finally, we use our observations of ice and vapor isotopes as a quantitative constraint to explore the implications on models of convective ice lofting and in situ cirrus formation in the TTL.

3.2 The Role of Isotopes

The isotopologues of water (HDO, $H_2^{18}O$ and $H_2^{16}O$; where $H_2^{16}O$ is hereafter referred to as H_2O) are useful tracers of convection and are suited to addressing the role of convective influence to the water budget of the UT/LS. Differences in the vapor pressures of the isotopologues are manifested by the preferential removal of the heavier molecular isotopes to the condensed phase when multiple phases of water are present at thermodynamic equilibrium, a process termed "isotopic fractionation." The degree to which the isotopes are fractionated is dependent on the phase transition (condensation/evaporation or deposition/sublimation) and the equilibrium temperature. Water isotope ratios (HDO/H_2O and $H_2^{18}O/H_2O$) then serve as a record of the condensation history of an air parcel (Pollock et al., 1980; Moyer et al., 1996; Keith,

2000). Isotope ratios are customarily expressed in terms of δ notation which relates the ratio of the heavier isotope to the lighter isotope against a standard reference, for instance: $\delta\mathrm{D}(‰) = 1000(\frac{[\mathrm{HDO}]/[\mathrm{H_2O}]}{2\times R_{\mathrm{VSMOW}}} - 1)$, where $2 \times R_{\mathrm{VSMOW}} = 3.115 \times 10^{-4}$ is the ratio of $\mathrm{HDO/H_2O}$ in Vienna Standard Mean Ocean Water (VSMOW) (Craig, 1961a). An analogous expression is obtained for $\delta^{18}\mathrm{O}$, with the $\mathrm{H_2^{18}O/H_2O}$ ratio in VSMOW equivalent to 2.0052×10^{-3}.

Rayleigh distillation (Dansgaard, 1964) is a process that models the isotopic composition of an air parcel during "gradual dehydration," (Holton and Gettelman, 2001) where condensate forms upon saturation and is immediately removed (Keith, 2000) thereby decreasing ("depleting") the δD of the remaining vapor. Despite its simplicity the model has been shown to describe the isotope ratio of water in the lower and middle troposphere under stably stratified conditions (Gedzelman, 1988); however, it over-predicts the depletion of HDO entering the stratosphere ($\delta\mathrm{D} \approx -900$ ‰) where measurements of water isotopes in the stratosphere set the entry value of HDO near -670 ‰ (Moyer et al., 1996; Johnson et al., 2001b; McCarthy et al., 2004).

3.2.1 Isotopic Fractionation Factor

The isotopic fractionation factor describes the ratio of an isotope between two phases. For any isotopic species between phases A and B the isotopes fractionate and the fractionation factor is simply: $\alpha_{A-B} \equiv R_A/R_B$, where R denotes the ratio of the heaver isotope to the lighter isotope in the indicated phase (see Fig. 3.1).

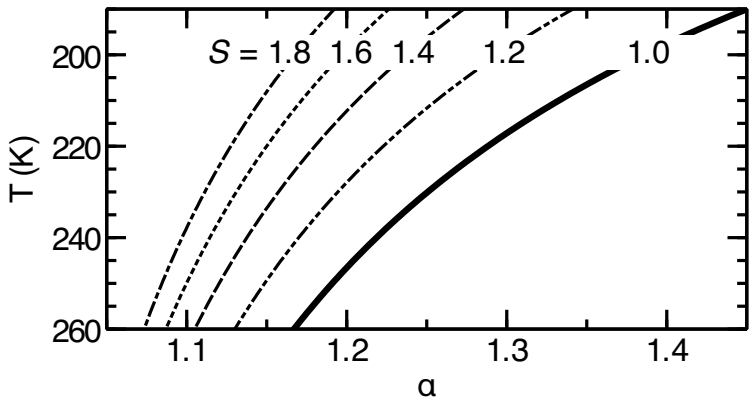

Figure 3.1: The isotopic fractionation factor α describes the partitioning of water isotopologues, HDO and H_2O in this case, during ice-vapor transitions and is temperature dependent, in addition to being influenced by the saturation ratio S at which condensation occurs.

3.2.2 Rayleigh Fractionation in an Open System

As an air parcel is lifted through the atmosphere by convection it cools and looses water vapor by the process of condensation. If the condensate is immediately removed from the air mass as it is formed, condensation can be viewed as a kinetic (non-equilibrium) process and can be modeled by Rayleigh fractionation. The water vapor isotopes are removed from the air mass by the uni-directional reactions:

$$\mathrm{HDO}_{(g)} \xrightarrow{k_{\mathrm{HDO}}} \mathrm{HDO}_{(l)} \tag{3.1a}$$

$$\mathrm{H_2O}_{(g)} \xrightarrow{k_{\mathrm{H_2O}}} \mathrm{H_2O}_{(l)}. \tag{3.1b}$$

The rate of removal of each water vapor isotope is not identical due to differences in the vapor pressure resulting from mass differences between deuterium and

hydrogen. The rate of removal of each water vapor isotope is given by,

$$\frac{d\left[\mathrm{HDO}_{(g)}\right]}{dt} = -k_{\mathrm{HDO}}\left[\mathrm{HDO}_{(g)}\right] \tag{3.2a}$$

$$\frac{d\left[\mathrm{H_2O}_{(g)}\right]}{dt} = -k_{\mathrm{H_2O}}\left[\mathrm{H_2O}_{(g)}\right] \tag{3.2b}$$

for $\mathrm{HDO}_{(g)}$ and $\mathrm{H_2O}_{(g)}$, respectively. It is the ratio of HDO to H_2O that is ultimately measured. At any instant, the change in the ratio of the water vapor isotopes is given by the quotient of 3.2a and 3.2b,

$$\frac{d\left[\mathrm{HDO}_{(g)}\right]}{d\left[\mathrm{H_2O}_{(g)}\right]} = \frac{k_{\mathrm{HDO}}\left[\mathrm{HDO}_{(g)}\right]}{k_{\mathrm{H_2O}}\left[\mathrm{H_2O}_{(g)}\right]}. \tag{3.3}$$

Rearranging equation 3.3 yields:

$$d\ln\left[\mathrm{HDO}_{(g)}\right] = \alpha\, d\ln\left[\mathrm{H_2O}_{(g)}\right], \tag{3.4}$$

where $\alpha = k_{\mathrm{HDO}}/k_{\mathrm{H_2O}}$ is the *isotopic fractionation factor* (Merlivat and Nief, 1967) and is the direct result of the vapor pressure isotope effect (see Fig. 3.1).

The isotopic profile the air mass can be calculated by integrating equation 3.4,

$$\int_{\left[\mathrm{HDO_{(g)}}\right]_0}^{\left[\mathrm{HDO_{(g)}}\right]} d\ln\left[\mathrm{HDO_{(g)}}\right] = \alpha \int_{\left[\mathrm{H_2O_{(g)}}\right]_0}^{\left[\mathrm{H_2O_{(g)}}\right]} d\ln\left[\mathrm{H_2O_{(g)}}\right] \tag{3.5}$$

to yield,

$$\ln\frac{\left[\mathrm{HDO}_{(g)}\right]}{\left[\mathrm{HDO}_{(g)}\right]_0} = \alpha\, \ln\frac{\left[\mathrm{H_2O}_{(g)}\right]}{\left[\mathrm{H_2O}_{(g)}\right]_0} \tag{3.6}$$

Exponentiating the above equation,

$$\frac{\left[\mathrm{HDO}_{(g)}\right]}{\left[\mathrm{HDO}_{(g)}\right]_0} = \left(\frac{\left[\mathrm{H_2O}_{(g)}\right]}{\left[\mathrm{H_2O}_{(g)}\right]_0}\right)^{\alpha} \tag{3.7}$$

and dividing through by the quantity $\left[\mathrm{H_2O}_{(g)}\right]/\left[\mathrm{H_2O}_{(g)}\right]_0$ gives the result,

$$\frac{\left[\mathrm{HDO}_{(g)}\right]/\left[\mathrm{H_2O}_{(g)}\right]}{\left[\mathrm{HDO}_{(g)}\right]_0/\left[\mathrm{H_2O}_{(g)}\right]_0} = \left(\frac{\left[\mathrm{H_2O}_{(g)}\right]}{\left[\mathrm{H_2O}_{(g)}\right]_0}\right)^{\alpha-1}. \tag{3.8}$$

Since $[\mathrm{H_2O}] \gg [\mathrm{HDO}]$ the total amount of water in the air mass can be approximated by $[\mathrm{H_2O}]$ exclusively and the fraction of water remaining in the air mass can be approximated by $f \approx \left[\mathrm{H_2O}_{(g)}\right]/\left[\mathrm{H_2O}_{(g)}\right]_0$. Using this approximation and the notation R and R_0 for the ratio of $[\mathrm{HDO}]$ to $[\mathrm{H_2O}]$ in the air mass for any fraction of water vapor remaining ($f < 1$) and the initial isotope ratio ($f = 1$), respectively, ultimately yields the familiar form of the Rayleigh equation for fractionation in an open system:

$$\frac{R}{R_0} = f^{\alpha-1}. \tag{3.9}$$

This can be written in terms of δD notation as:

$$\delta D = (\delta D_0 + 1000)\, f^{\alpha-1} - 1000. \tag{3.10}$$

3.2.3 Batch Fractionation in a Closed System

A model for the fractionation of water's isotopologues is a closed is developed here. The ratio of water's isotopologues in the lower troposphere is described by Rayleigh

fractionation in a open system. It is common to use a model where condensate is instantaneously removed from an air parcel upon formation. In a closed system the air parcel is subject to mass conservation, the sum of the isotopes across its various phases is conserved.

Developed here is a model that describes the partitioning of isotopes between the vapor and ice phases as a means of analysis for observations of $\delta\mathrm{D}_{ice}$ in anvil cirrus during the flight of 8 August 2007. Closed system batch fractionation is used to model the formation of ice in an air parcel following the detrainment. In this model an air mass can be lifted by convection but condensation does not occur until after detrainment of the air mass. Additionally, the detrained air mass may mix with ambient air masses and the fractionation of the isotopologues between the condensed and vapor phases is determined by the equilibrium temperature of the condensation process.

The initial number of water molecules in an air mass of volume V is related to the concentration (molecules cm^{-3})

$$N_{v_i} = N_{\mathrm{H_2O}\,(v)_i} + N_{\mathrm{HDO}\,(v)_i} = V \times \left([\mathrm{H_2O}\,(v)]_i + [\mathrm{HDO}\,(v)]_i\right) \tag{3.11}$$

and must be conserved during condensation as there is no loss and only partitioning between the vapor N_v and condensed N_c phases occurs,

$$N_{v_i} = N_v + N_c. \tag{3.12}$$

The fraction of HDO in any phase χ is simply given by the proportionality factor

$$R_\chi = N_{\mathrm{HDO}\,(\chi)} / \left(N_{\mathrm{H_2O}\,(\chi)} + N_{\mathrm{HDO}\,(\chi)} \right). \tag{3.13}$$

HDO is conserved amongst all the phases and can be written in terms of the total number of water molecules as:

$$N_{v_i} R_{v_i} = N_v R_v + N_c R_c. \tag{3.14}$$

Dividing equation 3.14 by N_{v_i} and defining $f \equiv N_v / N_{v_i}$ as the fraction of the initial vapor remaining and, similarly, the fraction of ice which has formed $1 - f \equiv N_c / N_{v_i}$, yields

$$R_{v_i} = f R_v + (1 - f) R_c. \tag{3.15}$$

Since $N_{\mathrm{H_2O}} \gg N_{\mathrm{HDO}}$ (for instance in seawater H_2O is, approximately, 3200 times more abundant than HDO) the total amount of water in the parcel is to a very good approximation described by the amount of H_2O (for VSMOW this approximation is better than 315 parts per million) and R can be written as $R \approx N_{\mathrm{HDO}} / N_{\mathrm{H_2O}}$. The fractionation of isotopes between the condensed and vapor phases is determined experimentally and can be written in terms of R

$$\alpha \equiv \frac{\left(N_{\mathrm{HDO}} / N_{\mathrm{H_2O}} \right)_c}{\left(N_{\mathrm{HDO}} / N_{\mathrm{H_2O}} \right)_v} = \frac{R_c}{R_v}. \tag{3.16}$$

The fractionation ratio of HDO, with respect to H_2O, over ice has the functional

form (Johnson et al., 2001a)

$$\alpha(T) = \exp\left[\frac{16829\ \mathrm{K}^2}{T^2} - 0.0945\right]. \tag{3.17}$$

Combining equations 3.16 and 3.15 yields an expression for the isotopic ratio of the condensed phase in a closed system

$$R_c(T) = \frac{R_{v_i}}{(1-f) + \frac{f}{\alpha(T)}}. \tag{3.18}$$

At the instant that the condensate is formed it is enriched by a factor of α relative to the initial vapor phase—this is the upper limit by which the ice can be enriched for the process of *in situ* condensation. As the vapor in the air mass is completely converted to condensate, the isotopic ratio of the condensate approaches the isotopic ratio of the initial vapor.

3.2.4 A Model Atmosphere

The atmospheric profile of an air mass that ascends in the absence of convection can be calculated from equation 3.10 by application of an appropriate vertical temperature profile and the pseudoadiabatic approximation.

3.2.4.1 Tropical Temperature Profile

A model vertical profile of the tropical tropopause is derived from MMS (Scott et al., 1990) data collected onboard the WB-57 aircraft during TC4. Temperature data were profiled by latitude so that only data collected between $\pm$ 10° of the

Equator contributed to the model. A manual variable-width binning procedure was utilized to select discrete points to form a monotonically decreasing spline curve that is characteristic of a negative lapse rate. The discretely-selected control points of the spline curve were then fit by a fourth-order polynomial to derive a continuous function that describes temperature with respect to altitude in an atmosphere as that experienced in the equatorial portion of TC4.

The modeled vertical temperature (K) profile with respect to altitude (km) of the equatorial troposphere can be represented a fourth-order polynomial: $T(Z) = c_4Z^4 + c_3Z^3 + c_2Z^2 + c_1Z + c_0$; with $\{c_4,\ c_3,\ c_2,\ c_1,\ c_0\}$ = {4.985E-03, -1.534E-01, 1.397, -1.059E01, 3.054} and fit between 0.8 and 16.1 km.

The modeled temperature profile can be extrapolated to lower altitudes and is valid from sea-level to the tropical cold point tropopause (16.1 km).

3.2.4.2 Pseudoadiabatic Ascent

The pseudoadiabatic approximation can be used to describe the fraction of water that remains as it ascends through the troposphere. An air mass will undergo adiabatic expansion as it ascends and thereby cools. In the tropics the air mass is assumed to be saturated at the surface (sea-level) and will maintain saturation (RH = 100 %) by condensation of water vapor to liquid water.

If the water vapor condenses and is instantly removed from the air mass by condensation the process is irreversible and not strictly adiabatic since some of the latent heat of condensation is carried with condensed phase. However, the amount of heat contained in the products is small relative to the heat carried by the air mass

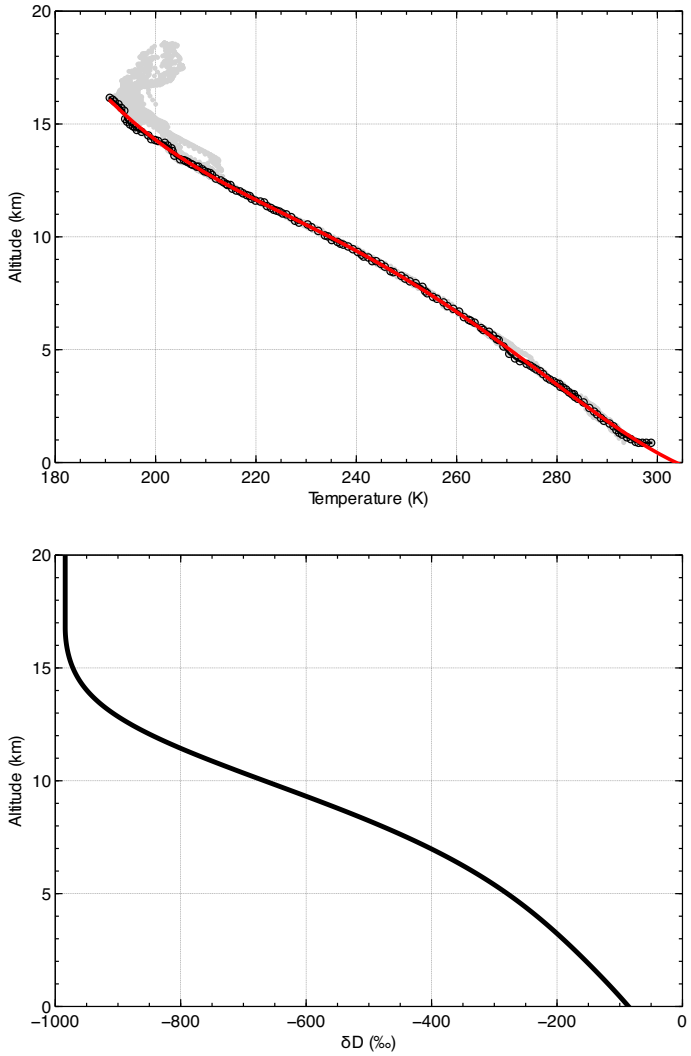

Figure 3.2: (a) The vertical temperature profile of the tropical region during the TC^4 mission. Temperature data collected by MMS between $\pm$ 10 $^\circ$ of the equator is shown by the gray dots, manually binned data is shown by the black open-circles and a fourth-order polynomial fit is shown by the red line. (b) The δD profile that is expected for a saturated air parcel which rises in a tropical atmosphere as modeled by the temperature fit in the upper panel. The air parcel is assumed to undergo pseudoadiabatic expansion and looses moisture via instantaneous condensation to the liquid phase so as to maintain saturation.

and the process can be considered to be *pseudoadiabatic*.

The concentration of water vapor within the air mass is set by the saturation vapor pressure and is a function of temperature. The World Meteorological Organization (WMO) recommends[1] the Goff equation (Goff, 1957), a reformulation of the classic reference equation as presented by Goff and Gratch (1946) for supercooled water:

$$\begin{aligned} \log e_w \;=\; & 10.79574(1 - 273.16/T) \\ & - 5.02800 \log(T/273.16) \\ & + 1.50475 \times 10^{-4}(1 - 10^{[-8.2969(T/273.16-1)]}) \\ & + 0.42873 \times 10^{-3}(10^{[4.76955(1-273.16/T)]} - 1) \\ & + 0.78614, \end{aligned} \tag{3.19}$$

where T(K) and the saturation vapor pressure, e_w, has units of hectopascal (hPa). The equation is valid in the range 223 - 375 K (Gibbins, 1990). There is less than 1% deviation over the entire temperature range between the 1946 and 1957 formulations.

The air mass, in this model, is assumed to be saturated at sea-level. Saturation is maintained as the air mass rises, such that the fraction of water vapor remaining in the air mass throughout ascent is simply:

$$f = \frac{e_{w_Z}}{e_{w_{Z=0}}} = \frac{e_{w_Z}}{\text{X (hPa)}}, \tag{3.20}$$

[1]See `http://cires.colorado.edu/~voemel/vp.html` for a discussion of the various formulations of saturation vapor pressure over liquid and ice. Additionally, errors contained in the 1998 & 2000 WMO formulations of the saturation vapor pressure over liquid are discussed.

with $T = 305$ K at sea-level as discussed in modeled tropical temperature profile (see Section 3.2.4.1).

3.2.5 The Role of Convection

Convection is prevalent throughout the tropical troposphere up to the base of the TTL ($\approx$ 14 km) but the degree to which it contributes to the water budget of the stratosphere is debated (Folkins et al., 1999; Liu and Zipser, 2005). In order to reconcile Lagrangian trajectory models with isotope observations the inclusion of convective ice lofting in the TTL is required (Dessler et al., 2007; Bony et al., 2008). While there is ample evidence of convective overshoots penetrating the stratosphere (above 380 K θ) and directly injecting ice (Corti et al., 2008; Hanisco et al., 2007; Danielsen, 1993; Weinstock, 2009), this may be more important in decoupling trends in stratospheric water vapor from tropopause temperatures (Dessler et al., 2007) than setting the entry value. Remote (Kuang et al., 2003) and in situ (Sayres et al., 2010; Webster and Heymsfield, 2003) water vapor isotope measurements throughout the TTL reiterate that convection can not be neglected.

Initially, convection can hydrate the local TTL by generating ice clouds above the cloud top. The mechanism by which these ice clouds are generated can be viewed, conceptually, at the boundaries of two distinct processes. At one limit, deep convection can be viewed as processes which entrains air in the lower/mid troposphere and lofts it into the TTL. As the entrained air is lofted it becomes saturated and condenses. The strong updraft velocities inside the convective tower prevents sedimentation, the air that is detrained carries with it a large amount of

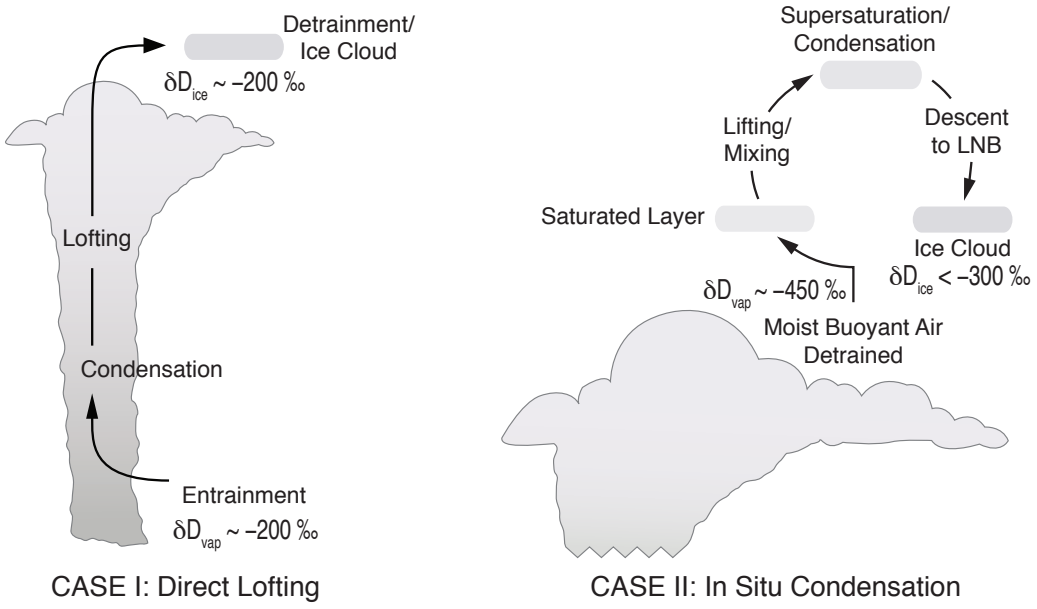

Figure 3.3: A conceptual drawing of the two scenarios for ice cloud formation mechanisms by convection. The isotopic signature of the sampled ice differs between the two scenarios; δD values shown are representative of observations described in the text. CASE I: Air is entrained in the lower atmosphere, where the vapor is isotopically heavier, and ice is formed by condensation. Strong vertical motion carries ice upwards and it is detrained into the TTL. CASE II: Moist buoyant air is detrained in the anvil region, where it lifts and mixes with a pre-existing saturated layer. This layer is displaced upwards and cools until it is supersaturated and ice is formed; the nascent ice cloud then descends back to its level of neutral buoyancy (LNB).

ice. This process is referred to as convective ice lofting (Fig. 3.3, CASE I).

At the other limit, the formation of ice clouds can be seen as a process which occurs outside of the convective tower. Convection detrains moist, ice-free air in the anvil region which is positively buoyant. As this air rises, and mixes in ambient air, it cools and reaches a level of (super)saturation suitable for ice nucleation and growth to occur. Finally, the nascent ice cloud descends to its level of neutral buoyancy (LNB). This processes is referred to as in situ condensation (Fig. 3.3, CASE II).

The isotopic signature of the ice in the clouds generated by these two processes will differ. It is inside this conceptual framework with which our observations of the isotopic composition of ice in clouds above the convective cloud top are interpreted in this paper.

3.3 Observations & Model

3.3.1 Measurement technique

The isotopic composition of the ice phase is determined from the difference between total (combined condensed and vapor phase) water and vapor phase isotope measurements made by Hoxotope and ICOS, respectively, two instruments developed at Harvard. Integrated Cavity Output Spectroscopy (ICOS) is a cavity enhanced absorption technique that uses a tunable quantum cascade laser to measure individual rotational transitions of H_2O, HDO, $H_2{}^{17}O$, $H_2{}^{18}O$ and CH_4 near 6.74 μm in the mid-infrared (Sayres et al., 2009). Sensitive detection in the UT/LS is achieved by the use of highly reflective mirrors to create a high-finesse cavity with a long effective path length. The Hoxotope instrument measures water isotopologues by a combination of photofragmentation and laser-induced fluorescence. Water is photolyzed by a pair of 172 nm excimer flash lamps to generate ground state OH and OD. The nascent radicals are subsequently detected by rotational state selective laser excitation at 287 nm and fluorescence at 309 nm (St. Clair et al., 2008). Apart from the conversion of Hoxotope from a vapor to a total water instrument by the addition of a heated forward-facing inlet, both instruments flew in a nearly identical

configuration for the TC4 mission as during the AVE_WIIF campaign where excellent agreement was demonstrated between the instruments in the subtropical and midlatitude UT/LS (Hanisco et al., 2007). A constant scaling factor of 1.1 and 1.2 are applied to the ICOS vapor measurements of H_2O and HDO, respectively. This scaling factor brings the measurements by the two isotope instruments into closer agreement during periods of clear-air sampling.

Hoxotope and ICOS flew together aboard the NASA WB-57 in pallet positions 1 and 2, respectively, as part of the Tropical Composition, Cloud and Climate Coupling (TC4) mission based out of Juan Santamaría International Airport near San José, Costa Rica during July/August 2007. Measurements from several instruments carried aboard the WB-57 during the TC4 mission are used throughout this paper: the Hoxotope instrument (total H_2O and HDO); the ICOS instrument (vapor H_2O, HDO, and $H_2^{18}O$); the Harvard Lyman-α hygrometer (vapor H_2O) (Weinstock et al., 1994); the Meteorological Measurement System (MMS) (pressure and temperature) (Scott et al., 1990); and the Cloud, Aerosol and Precipitation Spectrometer (CAPS) (Baumgardner et al., 2001) packaging together two instruments, a Cloud and Aerosol Spectrometer (CAS) (0.5 – 50 μm dia., particle size distribution) and a Cloud Imaging Probe (CIP) (25 – 1550 μm dia., particle size distribution). Additionally, data from the the Cloud Radar System (CRS) on the ER-2 (94 GHz radar reflectivity, dBZ) (Li et al., 2004) is used when the two aircraft are coordinated.

The TC4 mission was designed to investigate profiles and structures of the upper troposphere and lower stratosphere in the Tropical Eastern Pacific. During the flight on 8 August 2007, the WB-57 directly sampled above a large convective system over

the Panama Bight between 11 – 12 km. A stable layer, characterized by a zero lapse rate between 350 – 360 K θ, effectively capped convection to the sampling altitude near the base of the TTL.

Coordinated flight paths between the WB-57 and ER-2 during this flight allow us to use nadir radar reflectivity measurements from the CRS instrument on the overhead ER-2 to image the convective cell, as shown in Figure 3.4. Radar reflectivities less than −28 dBZ are removed from the data and a two-dimensional median smoothing filter, corresponding to bin sizes of 25 seconds and 225 meters in sampling time and altitude, respectively, is applied to minimize scatter noise. The convective cell was centered near 6.5°N, 83°W and had a spatial extent covering an area larger than 100 by 300 km. Note that the radar reflectivity data shown in Figure 3.4 only reflects periods of coordination between the two aircraft. Racetrack maneuvers were concentrated in two regions: in the southeastern quadrant near the core; and a northern east-west flight path over the outflow region. Cross sectional slices of the convective cell representing the structure directly below the WB-57 at the time of sampling are shown in Figure 3.6. Regions where ice clouds were sampled by Hoxotope along the flight path are shown by the red stars and cyan triangles (Fig. 3.4).

We apply strict criteria to determine cloud regions suitable for analysis: periods of ascent and descent are excluded; only water measurements by ICOS greater than 10 parts per million volume (ppmv) are included; and the ice fraction, derived from the difference between Hoxotope total water and ICOS vapor water measurements, is greater than 30 %. A 10 ppmv minimum threshold is placed on ICOS data to ensure good signal-to-noise from vapor measurements and a 30 % ice fraction ensures that

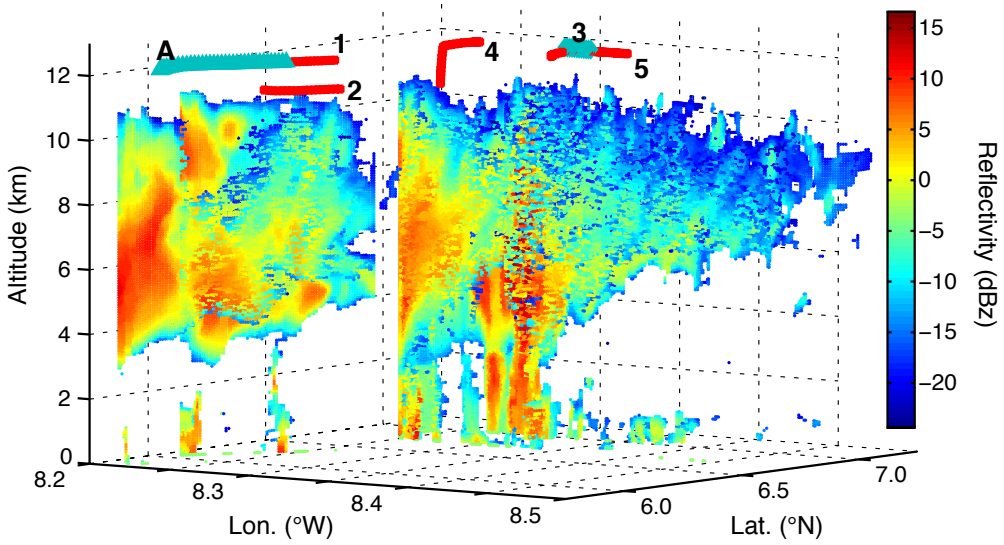

Figure 3.4: A pseudo-three-dimensional structure of the sampled convective cell generated from the CRS instrument aboard the ER-2. Only periods of coordination between the two aircraft are shown here. Two series of racetrack maneuvers sampled the core region in the southeast and the anvil region to the north. Identified ice cloud regions sampled by Hoxotope along the WB-57 flight track are shown by the red stars.

data is representative of clouds. The isotopic composition of the condensed phase is then directly calculated from Hoxotope and ICOS:

$$\delta\mathrm{D}_{ice} = \left[\frac{1}{R}\left(\frac{[\mathrm{HDO}]_{tw} - [\mathrm{HDO}]_{v}}{[\mathrm{H_2O}]_{tw} - [\mathrm{H_2O}]_{v}}\right) - 1\right] 1000 \tag{3.21}$$

where the subscripts tw and v represent total water and vapor measurements made by Hoxotope and ICOS, respectively, and R is the standard reference isotope ratio (VSMOW). The resulting data is then passed through a median smoothing filter and averaged in 60 second bins. Median filtering removes noisy point-to-point fluctuations and averaging binned data improves the signal-to-noise ratio.

3.3.2 In situ isotopic cloud model

With the assumption that air parcels are represented by only a single temperature history, the δD of the condensed phase serves as an indicator of its origin. Here we develop a simple model to ascertain whether condensation in the sampled air parcels occurred at the level of detrainment from the anvil or whether the condensate was generated during convection at lower altitudes (see Fig. 3.3 for a conceptual model). The first mechanism is consistent with in situ ice formation in the TTL, while the second is characteristic of ice being directly injected into the TTL. We model the case of in situ formation and ask: are our observations of $\delta\mathrm{D}_{ice}$ consistent with those predicted for a condensation event occurring at the temperature at which the air parcel was sampled?

Formation of ice by an in situ mechanism in our model requires that only the vapor

phase is detrained from the convective system (Fig. 3.3, CASE II). In the absence of sedimentation, total water is conserved in the air parcel and δD_{tw} is equivalent to the isotopic composition of the initial vapor at the time of detrainment. Supersaturation of the air parcel during detrainment results in instantaneous condensation. The rates of condensation of each of the isotopes of water are not equivalent, resulting in a temperature dependent enhancement of the heavy isotopes relative to H_2O in the condensed phase. The functional form of this enhancement for ice relative to vapor is

$$\alpha(T) = \exp\left[c_0 + c_1/T + c_2/T^2\right], \tag{3.22}$$

where $\{c_0,\, c_1,\, c_2\}$ are given by $\{-0.0945,\, 0,\, 16829\,\mathrm{K}^2\}$ and $\{-0.028224,\, 11.839\,\mathrm{K},\, 0\}$ for HDO and $H_2^{18}O$ over H_2O, respectively (Johnson et al., 2001a). Figure 3.1 (solid black line) shows the temperature dependence of α for HDO over H_2O during ice-vapor transitions.

In an air parcel where total water is conserved during condensation, the process can be modeled as Rayleigh fractionation in a closed system, where the ratio of the heavy isotope (HDO or $H_2^{18}O$) with respect to H_2O in the condensed phase, R_c, is given by

$$R_c = \frac{R_{v0}}{(1-f) + f/\alpha}. \tag{3.23}$$

R_{v0} is the isotope ratio of the initial vapor in the detrained air parcel; α is the fractionation ratio; and f is the fraction of the initial vapor remaining.

In the limit that a small fraction of the total water forms ice, the ice will have a maximum enhancement relative to the vapor. HDO in the ice is enhanced by a

factor α relative to its initial value in the vapor. In the limit that a large fraction of the total water forms ice, the ice will have an equivalent δD as the total water since HDO and H_2O are conserved during condensation. In determining the origin of the ice in cirrus clouds we invoke the limit that a small fraction of the total water forms ice. An in situ process therefore generates ice with an isotopic composition

$$\delta\mathrm{D}_{ice} \leq \alpha \cdot \delta\mathrm{D}_{v0} + 1000(\alpha - 1). \tag{3.24}$$

Formation of ice in a region of high vapor concentration and with significant mixing would give similar results as fractionation in an open system with a near constant isotope ratio in the vapor source throughout the condensation process.

Ice that is heavier than this limit is taken to be generated inside the convective system and directly lofted to the level of sampling. While the ice-vapor fractionation ratio is lower at the higher temperatures of the lower/middle troposphere, this is countered by the presence of isotopically heavier vapor. While it is tempting to use ice measured during convective lofting to determine the altitude of entrainment, the δD of ice does not necessarily represent this. Without a knowledge of detailed microphysics and ice processing history in the convective core, one cannot say without ambiguity that sampled ice represents a single condensation event. However, the δD of the sampled ice does place a limit on the maximum level of entrainment if air in the lower troposphere closely follows the Rayleigh curve (see Fig. 3.7, solid line).

3.3.2.1 Temperature sensitivity

The sensitivity of the isotopic threshold for ice formed under conditions of in situ condensation (Eq. 3.24) with respect to the temperature at which the process occurs in our isotopic model is given by

$$\frac{\partial \delta \mathrm{D}_{ice}}{\partial T} = [\delta \mathrm{D}_{v0} + 1000] \cdot \left[-\frac{2c_2 \exp\left(c_0 + c_2/T^2\right)}{T^3} \right] \tag{3.25}$$

for the case of HDO relative to H_2O; c_2 and c_0 are constants related to the functional form of isotopic fractionation factor and noted previously (see Eq. 3.22).

The more depleted the vapor in the parcel initially (prior to condensation), the less sensitive the final isotopic composition of the ice phase is to the temperature at which condensation occurs. At higher temperatures, there is less sensitivity to the input temperature in the model as $\partial\alpha/\partial T$ scales, approximately, as T^{-3}.

For an initial vapor composition $\delta \mathrm{D}_{v0} = -450$ ‰ the sensitivity of the final $\delta \mathrm{D}_{ice}$ to temperature ranges from 2.7 ‰/K to 1.8 ‰/K for input temperatures of 210 K and 235 K, respectively. Sensitivity to the input temperature is greater for a parcel that contains vapor that is less depleted (nearer to VSMOW) prior to condensation. A parcel with an initial vapor composition $\delta \mathrm{D}_{v0} = -350$ ‰ has temperature sensitivity between 3.1 ‰/K and 2.1 ‰/K for input temperatures of 210 K and 235 K, respectively.

MMS temperature measurements differ by less than 2 K for pressure coordinates between 190–240 hPa throughout the entire TC4 tropics. A lapse rate of 8.85 K km^{-1} from MMS measurements in this region of the atmosphere coupled with the

temperature sensitivity of the model implies a maximum uncertainty of less than 30 ‰ if convective outflow, and any subsequent condensation process, is taken to have occurred within ±1 km of the sampling altitude.

3.3.3 Cloud encounters

Implementing the criteria above yields five distinct cloud regions (Table 3.3.3) during the flight of 8 August 2007. Low O_3 and high CO mixing ratios in the identified cloud regions (Fig. 3.5, red diamonds) support that the air sampled was formed in the lower troposphere and lifted by convection.

Figure 3.6(a) shows the cross-sectional structure of the convective cell as the WB-57 traverses it. We identify the core of the convection cell in the region (designated region A) nearby region 1. Region A is characterized by high radar reflectivities that extend near to the surface and high total water concentrations. While no HDO vapor (ICOS) measurements are available during this region, water vapor (Lyman-α) measurements are available and indicate that a significant fraction of ice, up to 80 %, makes up the total water content.

Of the five ice regions where δD_{ice} measurements are available, region 1 can be identified as the region of strongest convection on the basis of radar reflectivity measurements, particularly at the upper levels of convection. This is supported by comparing measurements of the δD of ice to the predictions of the in situ cloud model. When the δD of observed ice (Fig. 3.6(e), yellow diamonds) is heavier than the δD predicted by the model (Fig. 3.6(e), green circles), that is when $\delta D_{meas.} > \delta D_{calc.}$, this indicates that the observed ice was convectively lofted to the level of sampling.

Table 3.1: Ice Encounters During the Flight of 08 August 2007

Region	Time ($\times 10^4$ s)	δD_v [a]	δD_{tw}	δD_{ice}	$[H_2O]_v$ [b]	$[H_2O]_{tw}$	$S_{i,v}$ [c]	$S_{i,tw}$
1	4.8403 – 4.8523	−541	-346 ± 157	-163 ± 67	97	166 ± 52	1.2	2.1 ± 0.6
2	4.9183 – 4.9363	−475	-460 ± 30	-391 ± 42	194	293 ± 44	1.2	1.9 ± 0.3
3	5.0503 – 5.0623	−521	-454 ± 70	-369 ± 55	101	128 ± 19	1.3	1.6 ± 0.2
4	5.0983 – 5.1223	−514	-455 ± 58	-350 ± 20	139	209 ± 119	1.1	1.6 ± 0.6
5	5.5423 – 5.5783	−514	-415 ± 93	-288 ± 112	109	176 ± 42	1.2	2.0 ± 0.4
A	4.8580 – 4.9120		-340 ± 90		109	269 ± 179	1.2	4.1 ± 1.7

Sampling conditions: altitude, 11.4 – 12.1 km; pressure, 191 – 226 mbar; θ 345 – 348 K; temperature 215 – 226 K.
All reported values reflect the mean value and standard deviation (1σ) in each region.
δ values are in units of ‰. Concentrations are in units of ppm.
[a] max. std. ≤ 23 ‰.
[b] max. std. ≤ 69 ppm in region 4, with max. std. ≤ 16 ppm in all other regions; measurements from Lyman-α.
[c] max. std. ≤ 0.2.

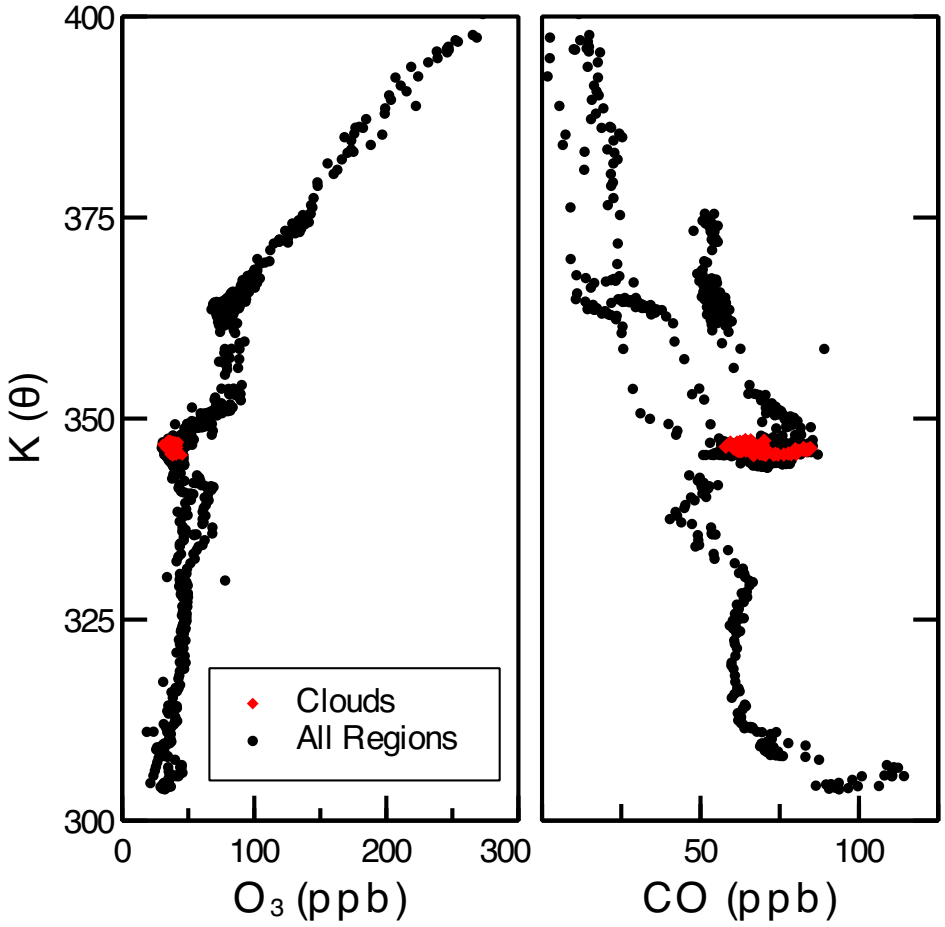

Figure 3.5: Measurements of convective tracers indicate a significant fraction of low-altitude air above the convective cell (black dots) and throughout the sampled ice regions (red diamonds).

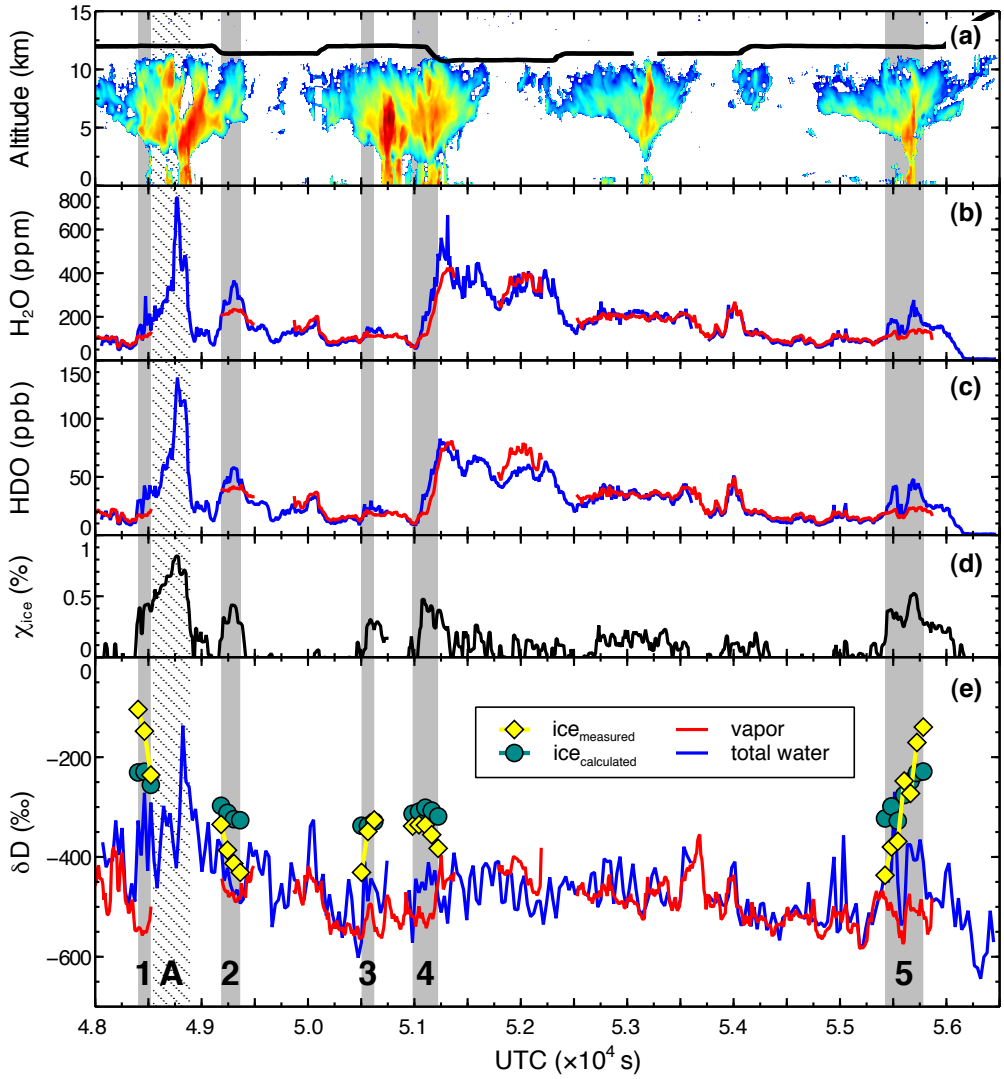

Figure 3.6: (a) CRS radar reflectivities along the WB-57 flight track (black line). The strongest convection is near region 1. (b) H_2O mixing rations of total water (blue) and vapor (red). (c) HDO mixing ratios of total water (blue) and vapor (red). (d) ice fraction determined from the difference between Hoxotope and Lyman-α. (e) δD of total water (blue) and vapor (red). The δD of ice is determined from the difference between Hoxotope and ICOS measurements (yellow). The heaviest value of δD of ice is expected from an in situ process (green) is shown. δD_{ice} that is lighter than this limit is taken to be generated by an in situ mechanism, see text for more details.

Conversely when $\delta D_{meas.} \leq \delta D_{calc.}$, the ice is taken to be formed by an in situ process near the level of sampling.

The model places an upper-limit isotopic threshold by which to evaluate in situ condensation processes. Underdepletion of ice in our model relative to observations are to be taken as a limitation of the model, which neglects to describe the potential processes discussed below. However, as the model is designed to evaluate the maximum enhancement expected during in situ condensation any significant overdepletion in the model relative to observations is indicative of alternate pathways that can generate ice that is heavier. Specifically, condensation within the lower or middle troposphere, where the source vapor is heavier (see Fig. 3.7), and subsequent lofting of the condensate to the sampling altitude by convection.

The kinetic fraction factor α decreases with increasing temperatures whereby the preference of the heavy isotopes in the condensed phase is diminished. While assuming too low a temperature of condensation temperature biases the model towards underdepletion, it plays a minor role relative to the following processes.

Condensation in a closed system produces maximum isotopic enhancement of the ice phase in the limit that only a small fraction of ice forms from the initial vapor. As the ice fraction grows the kinetic isotope effect is diminished. The preference of the heavy isotope for the condensed phase is limited by its decreased availability in the vapor phase. This is discussed previously (see eq. 3.23) .

Formation of ice under conditions of supersaturation diminishes α as the uptake rate of the isotopes of water into the condensed phase is diffusion-controlled. The influence of supersaturation on the kinetic fractionation factor is discussed later in

this chapter (see eq. 3.27).

Isotope measurements of ice are heavier than -150 ‰ at first encounter in region 1 while the maximum value predicted for ice in this region formed by an in situ process is less than -200 ‰. Underdepletion of observed ice in this region is well outside any error that can be prescribed to the temperature sensitivity of our model. Region 5 is the only other region that exhibits a measured ice isotope ratio which exceeds that predicted by in situ formation and is similar to ice in region 1. Radar reflectivity measurements show weaker convection in region 5 than region 1. This region was sampled roughly 75 minutes after region 4 and it is downwind of the convective core near the outflow region so it may reflect earlier convection nearer to the core.

The aircraft descended into the convective system in region 4. Both total water and water vapor ratios are observed to increase as the aircraft moves nearer the convective system, with total water increasing at a faster rate than the vapor, indicating the presence of ice. Outside of the shaded region 4, the vapor is heavier than the ice. The sharp peaks seen in the total H_2O signal in this region are not reflected in the total HDO signal or in either vapor isotope, leading to lighter δD measurements of total water during these events relative to the vapor phase.

Regions 2, 3 and 4 exhibit HDO signatures that are consistent with in situ ice formation. In these regions the saturation of vapor over ice is similar to the other regions. The total water observed in these regions is twice the saturation ratio, lower than in region 1.

A high water event was encountered in region A where total water mixing ratios

exceed 600 ppmv. This region is directly above the core region, as determined by high radar reflectivities, particularly at the upper levels of convection. During this period only measurements by Hoxotope and Lyman-α are available. Without a vapor isotope measurement, an estimate of the minimum value for δD of ice can be made from the measured ice fraction in the region, which ranges from 40 – 80 %.

Taking the measurement of the isotopic ratio of total water as a composite of ice and vapor, we can estimate the isotopic composition of the ice as a function of the ice fraction, χ_{ice}:

$$\delta\mathrm{D}_{ice} = \frac{\delta\mathrm{D}_{tw} - (1 - \chi_{ice})\delta\mathrm{D}_{v}}{\chi_{ice}}. \tag{3.26}$$

δD of the vapor is consistent across all cloud regions, so we can take the isotopic composition of vapor in region A to be equivalent to the aggregate mean, $\delta\mathrm{D}_v = -552 \pm 26$ ‰. Applying the same 30 % ice fraction criteria for clouds in the region, gives a mean cloud ice fraction of $\chi_{ice} = 0.63 \pm 0.13$ in region A. The mean value for total water in the cloud region is $\delta\mathrm{D}_{tw} = -338 \pm 102$ ‰. With these constraints the isotopic composition of ice in this region is estimated from equation 3.26 as −212 ‰. Although there are no direct measurements of $\delta\mathrm{D}_v$ in this region, we show by example that the large ice fractions in this region make the estimate relatively insensitive to the uncertainty in $\delta\mathrm{D}_v$. Choosing $\delta\mathrm{D}_v$ near the limits observed in the TTL of −450 ‰ and −650 ‰ yield an estimate of the $\delta\mathrm{D}_{ice}$ of −272 ‰ and −155 ‰, respectively. A more realistic choice places the limits of the δD of the vapor between −500 ‰ and −600 ‰, yielding a $\delta\mathrm{D}_{ice} = -212 \pm 31$ ‰ in this region.

Region A has a vapor saturation ratio of 1.3 relative to ice and total water content over eight times the saturation ratio. Large total water concentrations and

the brief encounter with heavy δD_{tw} indicate that the ice encountered in this region is directly injected. It is unlikely that convection would be able to maintain the high supersaturation ratios required for in situ formation of ice under these conditions. Further evidence of ice lofting from low altitudes comes from measurements of the size distribution of ice, the particles in this region have an average area nearly an order of magnitude larger than particles outside this region.

3.4 Discussion

Flight to flight variations of δD of vapor at the base of the TTL were observed with values ranging from -450 to -600 ‰ in the summertime tropics with a mean value of -552 ‰ during cloud encounters on the 8 August flight. The variation in δD at the base of the TTL is consistent with observation throughout the TTL during TC4, however the mean vertical profile is invariant and has a value of -550 ‰. ATMOS observations of tropical HDO/H_2O ratios in the TTL show a similar invariance in the vertical profile despite a mean δD in the TTL region of approximately -650 ‰ (Kuang et al., 2003). These observations are from the wintertime tropics and are consistent with in situ observations made by ICOS during the wintertime CR-AVE mission. The wintertime water vapor minimum at the tropical tropopause ($\theta \approx$ 380 K) is 2.5 ppmv, while the summertime tropopause water vapor minimum showed significant variations between flights and ranged from a minimum of 5 ppmv to a maximum of 10 ppmv (Sayres et al., 2009). Summertime convection is capable of moving significantly more water vapor, which is also isotopically heavier, through

the tropical tropopause into the stratosphere.

3.4.1 Ice lofting in the TTL

3.4.1.1 Convective dehydration models

The "convective dehydration" model presented by Dessler and Sherwood (2003), hereafter Dessler03, found that the budget of HDO and H_2O in the TTL is set by the balance between drying by the convective injection of dry air and moistening by sublimation of ice, with the rate of maximum detrainment from convection found near the base of the TTL ($\approx$ 140 hPa). Mixing between dry and wet air parcels produces different outcomes with respect to concentration of water and the isotope ratio in the mixed parcel. The final concentration is the mean of the weighted contribution of each parcel. In the case that a supersaturated parcel containing ice is mixed with a dry parcel, the final mixed parcel will be undersaturated given a large contribution from the dry parcel. However, the isotope signature in the mixed parcel looks very different. In the limit that the dry air parcel contains no water, the mixed parcel will have the same isotopic composition as the wet parcel. This results from both H_2O and HDO being diluted equally and thus there is no change in the isotopic ratio although there is a change in the absolute concentration of both isotopes. Even if the dry parcel contains water, it only starts to influence the isotope ratio of the mixed parcel when it contributes a significant fraction of the water.

As the rate of detrainment of water decreases exponentially above the base of the TTL, the isotopic composition at the base of the TTL is almost entirely responsible for setting the isotopic composition throughout the TTL. Sherwood and

Dessler (2001) found that the retention of ice in detrained air was required to produce a distribution of water in the TTL and entering the stratosphere that matched observations. Using a 4:1 ice/vapor ratio from this previous work as a constraint, the Dessler03 model required that lofted ice have a δD = −565 ‰ to reproduce the ATMOS observations (Kuang et al., 2003) of the δD in the TTL. While the authors note that this value does not necessarily reflect the δD of ice, but rather the δD of ice that evaporates, this value is much more depleted than the measurements of δD ice from TC4.

If we take our limited observations to be representative of the entire summertime tropics then choosing a value of −314 ‰ which is near the observed mean value of −370 ‰ for in situ regions in our observations, results in a TTL with a mean vertical profile of roughly −430 ‰ in the Dessler03 model. This produces a TTL that is too enriched in HDO, even for summertime conditions. The inclusion of heavier lofted ice, where the ratio of retained ice to vapor in the parcel (3.0 ± 1.2) more closely matches the constraints of the model, would result in a TTL that is under-depleted with respect to all observational data.

3.4.1.2 Convectively influenced trajectory models

Dessler et al. (2007) presented an updated model with "more realistic mixing" in the TTL based on the Fueglistaler and Haynes (2005) model, hereafter Fueglistaler05. The Fueglistaler05 model is a trajectory based model where parcels are saturated at 340 K θ and maintain saturation as they are transported through the TTL by condensation. The concentration of water in any parcel above the tropopause reflects

the minimum temperature ("Lagrangian cold point") experienced by that parcel in the TTL. Water vapor distributions in the tropical UT/LS are accurately predicted by the model but the neglect of isotope physics produces over-depletion of HDO.

The Dessler07 model addressed this issue by incorporating a stochastic convective influence scheme into the model where the probability of convection in the TTL is derived from an annual climatology between $\pm 30^{\circ}$ of the equator. With convection capped below the tropopause, the model is able to enhance HDO in the UT/LS with a minimum perturbation to the overall humidity in the region. In order to reproduce observed HDO in the TTL and 400 K θ H_2O abundances, convection was capped at 375 K θ with the δD of lofted ice set to -100 ‰, a convective timescale of 3 hours and an initial δD of vapor of -650 ‰ at the base of the TTL (340 K θ). The authors note that there are many uncertainties in the parameterization of ice-lofting and that the model should be taken as qualitative with regards to analysis.

Incorporating observations and estimates (i.e., regions 1 and A) of the δD of ice from our in situ data we recommend that δD of ice be constrained to a value of -200 ‰ when parameterizing convective influence schemes such as that used in the Dessler07 model. While δD ice near -100 ‰ was directly observed in region 1, the choice of -200 ‰ reflects the expanded statistics across regions 1 and A. We briefly explore the effect this has on the isotopic composition of the TTL in the context of mixing scheme as described by the Dessler07 model.

A mean vertical profile of δD of -650 ‰ is utilized in the Dessler07 model to match global ATMOS observations of δD between 5°N and 20°N from November 1994 (Kuang et al., 2003) and serves as a reference case to test the sensitivity of

the model to key parameters: δD at the base of the TTL, convective timescale and the isotopic composition of convectively lofted ice, where the reference values are discussed above. This is in agreement with wintertime observations from CR-AVE (Sayres et al., 2010), however, the mean vertical profile of δD in the summertime TTL from TC4 observations is -550 ‰. Decreasing the HDO abundance of the injected ice such that the δD of ice is -200 ‰ lightens the TTL by roughly 25 ‰ relative to the reference case. This results in a mean vertical δD profile in the TTL closer to -675 ‰. Doubling (halving) the convective timescale in the model to 6 hours (1.5 hours) has roughly twice the influence on the δD of the TTL than the change prescribed to altering the δD of ice as above, yielding a mean composition of -700 ‰ (-600 ‰) in the TTL. Setting the isotopic composition at the base of the TTL (340 K θ) to -550 ‰ provides an initial HDO enhancement that quickly diminishes with height, above 365 K θ the vertical profile matches the reference profile.

Vertical profiles of δD in the TTL from the Dessler07 model are sensitive primarily to the choice of convective timescale followed by the δD of lofted ice. Decreasing the convective timescale improves the agreement between the model and our summertime observations. However, seasonal variations are likely important.

3.4.2 In situ ice formation

The in situ cloud regions encountered during the August 8 flight are distinct, both in terms of isotopic composition and saturation profiles, from regions identified as carrying lofted ice. While in situ clouds may be a minor component of the ice that contributes to the water budget of the TTL, they play a role in the radiative

properties of the region. The stacking of tropical tropopause cirrus (TTC) and anvil cirrus, separated by several kilometers, has been observed previously (Winker and Trepte, 1998; Santacesaria et al., 2003). Garrett et al. (2004) observed long-lived thin tropopause cirrus above convective cells with horizontal dimensions nearly identical to the anvils beneath them and proposed a hypothesis that tropopause cirrus are formed at low-latitudes by the moistening and forced uplift of stratiform pileus by convection. Initially, ambient air in a stable layer is forced upwards by a turret from deep convection and reaches its condensation level forming a pileus cloud. The pileus cloud forms a cap over the the top of the turret and the stable layer may be penetrated by the turret if convection is sufficiently vigorous, leading to a mixing of air from the stable layer and the convective cell. As the turret falls to its level of neutral buoyancy, a stratiform layer develops and evaporation is prevented as a result of the enhanced moisture from mixing.

While we do not extend the TTC formation hypothesis presented by Garrett et al. (2004), we discuss our observations of the isotopic composition of ice and vapor in the in situ cloud regions in support of this hypothesis. Evidence for turbulent mixing between air from the convective cell is supported by the low ozone and high carbon monoxide mixing ratios during these clouds encounters (Fig. 3.5). A critical ice saturation ratio of 1.55 is required for homogenous freezing of ice particles at the temperatures measured in the in situ clouds (216 – 222 K) (Koop et al., 2000), similar to the conditions described by Garrett et al. (2004) during CRYSTAL-FACE. While the Garrett et al. (2004) mechanism is speculative, we propose that our observations are consistent with a similar mechanism for the formation of in situ cirrus above the

convective cell during TC4.

3.4.2.1 Kinetic isotope effects

We briefly revisit the issue of kinetic isotope effects to assess the role of supersaturation in determining the isotopic composition within the TTL. The range of δD of vapor sampled at the base of the TTL ranges between -600 and -450 ‰. This range in the vapor is consistent with Rayleigh distillation occurring at saturations of between 1 and 2 (see Fig. 3.7). Moyer et al. (1996) suggested that saturation ratios up to 2 may be sustained within the core of strong convective cells. By investigating the abundance of δ^{18}O relative to δD we show that the requisite total water saturation ratio of 1.7 in the in situ cloud regions was not generated by sustained supersaturation in the convective cell. Rather, the isotope and tracer measurements suggest that mixing and vertical displacement are responsible for generating the supersaturated conditions required for in situ condensation.

When condensation occurs at saturation, the ratio relationship between δ^{18}O and δD falls along the well-known meteoric water line (MWL) (Fig. 3.8b, thick black line) (Craig, 1961b). The ratio of δ^{18}O to δD decreases when condensation occurs under supersaturated conditions as $H_2^{18}O$ becomes less fractionated relative to HDO, a result of the smaller kinetic effect of $H_2^{18}O$. Under supersaturated conditions isotopic fraction is diffusion-controlled and the isotopic fractionation ratio is adjusted as a function of the saturation ratio S of the vapor relative to the condensate (Jouzel and

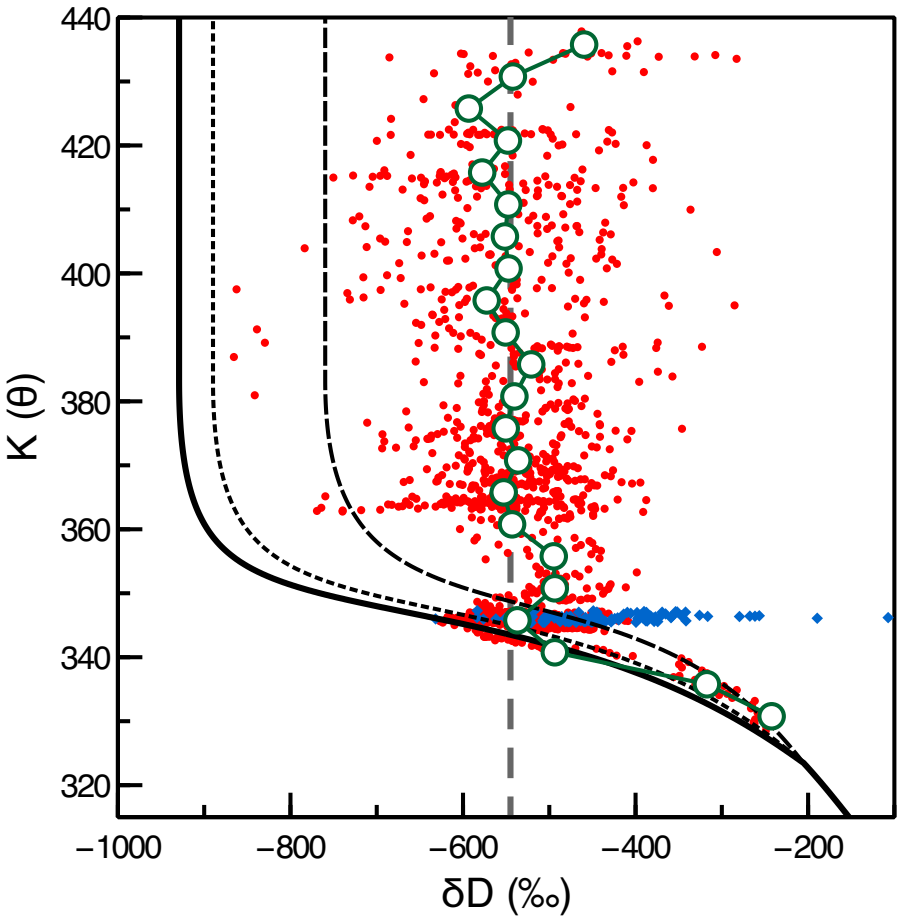

Figure 3.7: The vertical profile for δD vapor (red circles) from all measurements within 10° of the Equator. The mean isotopic composition of vapor in the TTL (binned average every 5 K (θ), shown by open green circles) is largely invariant with height and has a mean value of −545 ‰ between 345 – 430 K (θ) (dashed gray line). The isotopic composition of total water sampled during identified cloud regions for the August 8 flight is shown in blue. The expected δD from a Rayleigh process occurring with saturation ratios (S_i) of 1.0, 1.2, and 2 are shown by the thick solid, dotted and dashed black lines, respectively.

Merlivat, 1984; Keith, 2000)

$$\alpha_{\text{kinetic}} = \frac{\alpha S}{\alpha \frac{D}{D'}(S-1)+1}, \tag{3.27}$$

where D/D' is the ratio of the molecular diffusion coefficients of the lighter isotope (H_2O) to the heavier isotopes (HDO or $H_2^{18}O$).

The values reported by Merlivat (Merlivat, 1978) for HDO and $H_2^{18}O$ with respect to H_2O (i.e., D'/D) are $D_{\text{HDO}}/D_{\text{H}_2\text{O}} = 0.9755$ and $D_{\text{H}_2^{18}\text{O}}/D_{\text{H}_2\text{O}} = 0.9723$, respectively. These values are commonly used. Cappa et al. (2003) reexamined the issue and suggested that the appropriate molecular diffusion coefficients are $D_{\text{HDO}}/D_{\text{H}_2\text{O}} = 0.9839$ and $D_{\text{H}_2^{18}\text{O}}/D_{\text{H}_2\text{O}} = 0.9691$. The recent measurements by Cappa et al. (2003) accounted for surface cooling and the authors noted that the values found are in closer agreement with kinetic theory, eliminating the different effective collision diameters of the isotopes of water as suggested by Merlivat (1978). We do not discuss the discrepancy further but point out that in light of the new values reported by Cappa et al. (2003) there is a decreased likelihood of sustained supersaturation during convection. Note that we use the diffusivity values from Merlivat (1978) in our analysis throughout.

A plot of observed $\delta^{18}O$ against δD of the vapor phase, as measured by ICOS, during cloud encounters shows that the isotopic composition of the vapor phase has been minimally influenced by condensation under supersaturated conditions (Fig. 3.8b, blue squares). Measurements across the entire 8 August flight show a similar supersaturation signature (gray dots). We can rule out direct detrainment of supersaturated air from the convective anvil followed by condensation as the mechanism

responsible for generating in situ clouds.

3.4.2.2 Kinetic isotope effects in a closed system

The curves shown in Fig. 3.8(b) only apply to condensation in an open system, a system where the condensate is removed by sedimentation as it forms. In a closed system the condensate is formed from a vapor reservoir where the heavy isotopes are preferentially condensed. Under supersaturated conditions HDO is condensed at a faster rate than $H_2^{18}O$, due to differences in the their diffusion coefficients. Figure 3.8(a) shows the changes in the isotope ratios of HDO and $H_2^{18}O$, relative to H_2O, as vapor is lost into the condensed phase. We chose conditions representing the mean conditions within in situ clouds regions as constraints to model the process: a constant temperature of 220 K and an initial δD of -455 ‰ in the vapor. We assume that the vapor was not subjected to supersaturation during ascent and therefore the $H_2^{18}O$ abundance of the vapor can be determined directly from the MWL, giving an initial value of $\delta^{18}O = -67$ ‰. Condensation is modeled at the two limits of possible saturation ratios in the air parcel.

In the first scenario, the air parcel is lifted until a saturation ratio of 1.7 is reached. At this point condensation occurs until a 30 % ice fraction is reached in the parcel (shown by the open crosses in Fig. 3.8(a)) leaving a final saturation ratio of 1.2 in the vapor. In the second scenario, the parcel is lifted maintaining saturation ($S_i = 1$) and the rate of loss of both HDO and $H_2^{18}O$ from the vapor is greater as there is no kinetic isotope effect. The ratios of the two isotopes of the vapor in the final parcel are indicated in Fig. 3.8(a) (filled crosses). The results of condensation

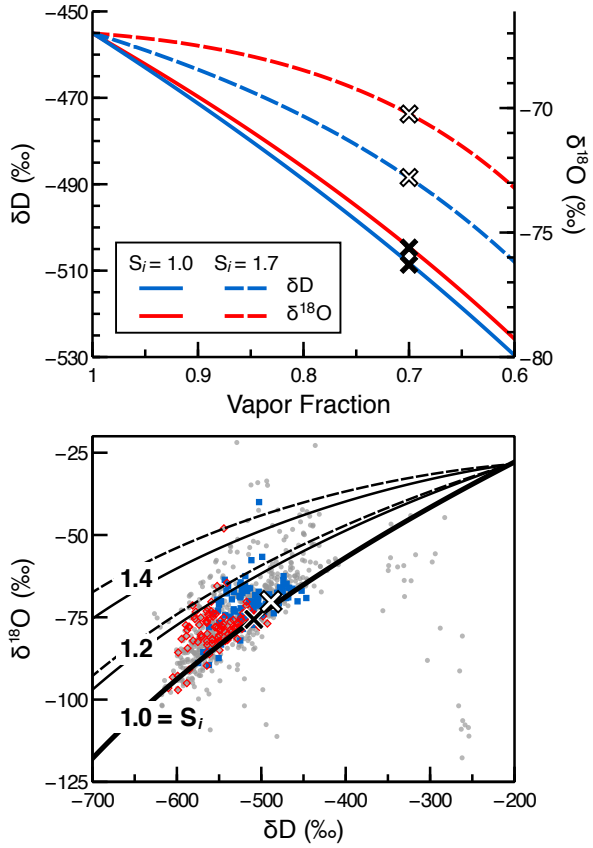

Figure 3.8: (a) A model of the kinetic isotope effect in a closed system. The evolution of the isotopic composition in the vapor is shown under conditions of supersaturation (dashed lines) and saturation (solid lines), with an initial S_i of 1.7 and 1.0. The crosses indicate the δ^{18}O (red) and δD in the vapor after an ice fraction of 30 % is achieved; (b) The ratio of δ^{18}O relative to δD of the measured vapor is expected to decrease with increasing supersaturation as a result of kinetic effects. Shown are the expected ratios of the vapor's isotopes under increasing saturation. The well-known meteoric water line is shown by the bold black line and is expected for condensation occurring at saturation ($S_i = 1$). The expected isotope ratios under supersaturated conditions are shown using diffusivity data from Merlivat Merlivat (1978) (solid lines) and Cappa Cappa et al. (2003) (dashed lines). The isotopic composition of the resulting vapor from condensation in a closed system to form in situ clouds, described in (a), is shown by the crosses. Condensation under supersaturated conditions in a closed system does not produce large deviations from the MWL.

under different saturation ratios can be evaluated in the context of our observations by transforming the results in Fig. 3.8(a) into an alternate coordinate system, this is shown in Figure 3.8(b) (open and closed crosses).

Two sets of in-cloud data are shown in Figure 3.8(b). The red diamonds and gray dots are data taken directly from ICOS without applying a scaling factor to any of the isotopes. Clear air comparisons between ICOS and Hoxotope require that ICOS measurements of HDO and H_2O be scaled by a factor of 1.2 and 1.1, respectively, to bring them into closer agreement with Hoxotope. In order to preserve the relationship with respect to the MWL, a constant scaling factor of 1.0084 is applied to the $H_2^{18}O/H_2O$ ratio when calculating $\delta^{18}O$. The blue squares in Figure 3.8(b) reflect these scaling parameters as applied to the ICOS data set.

The conclusion to draw from this analysis is that sustained supersaturation inside a convective cell is not responsible for generating the supersaturation required for in situ ice clouds above a convective cell. Two corollaries are to be taken from this. Firstly, the enhanced δD in the vapor at the base of the TTL is not determined by supersaturation. This is the same conclusion reached by Keith (2000) and Johnson et al. (2001a). Sayres et al. (2010) came to a similar conclusion with in situ measurements. A seasonal trend is evident in the data presented by Sayres et al. (2010) with supersaturation more prevalent during the boreal summer. It is a subset of this data we are presenting here (Fig. 3.8(b)). Although supersaturation is apparent in the summertime data it is mostly limited to saturation ratios less than 1.2. This degree of supersaturation during convection manifests as a small enhancement to the δD of vapor at the base of the TTL and predicts over-depletion throughout the TTL

(Fig. 3.7). Secondly, high saturation ratios can be generated by convectively-induced lifting of a stably stratified layer. Under such circumstances, condensation generates an isotopic signature in the vapor that lies close to the MWL. That is, in a closed system, condensation under supersaturated conditions does not generate large deviations from the MWL; any isotopic signature of supersaturation in the vapor must be the result of condensation in an open system.

The distribution of points above the MWL in Figure 3.8b results from vapor that has previously experienced supersaturation. The large variation in δD during in situ cloud periods and the increased uncertainty in δ^{18}O due to $H_2^{18}O$ scaling make it difficult to determine the degree of supersaturation during condensation and formation of in situ clouds from the vapor measurements alone. However, the over-depletion in the measurements of the δD of ice relative to the predictions of the in situ closed box model suggests that the formation of in situ ice likely occurred under supersaturated conditions.

To illustrate this point, consider the δD of ice predicted by equation 3.24. Starting with an initial HDO abundance in the vapor of $\delta D_{v0} = -456$ ‰, determined from the mean δD_{tw} values across regions 2, 3 and 4, and a mean temperature of 219 K in these regions, the predicted value of $\delta D_{ice} = -297$ ‰. The HDO content of the ice by this analysis is roughly 70 ‰ under-depleted relative to the observations. If the ice is instead formed under supersaturated conditions the resulting ice would be more depleted.

In order to bring the predicted δD_{ice} from equation 3.24 into agreement with the observations, an adjusted fraction factor, $\alpha_{kin.} = 1.1581$, is required. From equa-

tion 3.27, the saturation ratio over ice that results in such an $\alpha_{kin.}$ is determined to be equivalent to $S_i = 1.55$. This is in close agreement with the critical saturation ratio required for homogenous freezing of ice particles predicted by Koop et al. (2000) at temperatures between 215 – 225 K. While the inferred condensation saturation ratio is high, it is important to note that convectively-induced lifting of a stably stratified layer to such a saturation ratio and its subsequent condensation will not produce a large deviation from the MWL (see Fig. 3.8b). This process is initiated by an induced perturbation to the saturation ratio of a parcel and is modeled as a closed system. Condensation under supersaturated conditions is likely the mechanism responsible for generating in situ clouds observed above convective cells.

3.5 Conclusions

The in situ observations presented here provide direct measurements of the isotopic composition of ice encountered in the TTL. From a simple in situ cloud model we determine that tropical convection is capable of generating ice by two simultaneous mechanisms: direct injection of lofted ice and in situ condensation. Convective tracers indicate that air entrained at low altitudes is a significant component of the cloud regions. We note that our in situ observations of convective influence as well as summertime observations of isotopes in the TTL, in general, are limited.

A comparison of in situ data sets presented by Sayres et al. (2010) suggests that the summertime tropics are capable of transporting heavier and wetter air into the stratosphere. This result, being mindful of the limitations discussed above, acknowl-

edges the increased influence of convection and changes in climatology of the TTL during the summer. Our analysis finds that directly injected ice is isotopically heavier and carries more water into the TTL than in situ clouds. While direct injection of ice into the TTL is generally regarded as being primarily responsible for influencing the isotopic composition of the TTL, further examination is required to resolve the impact of different ice pathways (i.e., localized ice injection near the core versus wider-spread in situ ice throughout the outflow region) on the water budget and radiative properties of the TTL.

The isotopic composition of ice in models has been relatively unconstrained from a lack of measurements. With our observations we suggest that ice be constrained to a value of $\delta\mathrm{D}_{ice} = -200$ ‰ in future models. We explore the implications of this value in the Dessler07 model and find that this value reproduces observations when coupled with a decrease in convective timescales in the model.

Finally, we evaluate the in situ cloud formation mechanism suggested by Garrett et al. (2004) using our isotope measurements. Simultaneous observations of $\delta^{18}\mathrm{O}$ and $\delta\mathrm{D}$ of the vapor phase by ICOS allow us to rule out the detrainment of vapor that has undergone sustained supersaturation during convection as the mechanism responsible for generating in situ clouds. This result reemphasizes the importance of ice lofting in under-depleting the TTL with respect to the Rayleigh process. An analysis of the kinetic isotopes effects finds that condensation under supersaturated conditions does not produce large departures of the vapor from the MWL in a closed system. Moreover, the observed over-depletion of $\delta\mathrm{D}_{ice}$ during in situ cloud encounters, relative to our model, is consistent with the critical saturation ratio required

the for homogenous freezing of ice particles suggested by Koop et al. (2000).

References

D. Baumgardner, H. Jonsson, W. Dawson, D. O'Connor, and R. Newton. The cloud, aerosol and precipitation spectrometer: A new instrument for cloud investigations. *Atmospheric Research*, 59:251–264, 2001.

M. Bonazzola and P. Haynes. A trajectory-based study of the tropical tropopause region. *Journal of geophysical research*, 109(D20):D20112, 2004.

S. Bony, C. Risi, and F. Vimeux. Influence of convective processes on the isotopic composition (δ^{18}O and δD) of precipitation and water vapor in the tropics: 1. Radiative-convective equilibrium and Tropical Ocean–Global Atmosphere–Coupled Ocean-Atmosphere Response Experiment (TOGA-COARE) simulations. *Journal of Geophysical Research*, 113:D19305, 2008.

C. Cappa, M. Hendricks, D. DePaolo, and R. Cohen. Isotopic fractionation of water during evaporation. *Journal of Geophysical Research-Atmospheres*, 108(D16):4525, Aug. 2003. doi: DOI10.1029/2003JD003597.

T. Corti, B. Luo, M. De Reus, D. Brunner, F. Cairo, M. Mahoney, G. Martucci, R. Matthey, V. Mitev, F. Dos Santos, et al. Unprecedented evidence for overshooting convection hydrating the tropical stratosphere. *Geophysical Research Letters*, 35, 2008.

H. Craig. Standard for reporting concentrations of deuterium and oxygen-18 in natural waters. *Science*, 133(3467):1833, 1961a.

H. Craig. Isotopic variations in meteoric waters. *Science*, 133(3465):1702–1703, May 1961b.

E. Danielsen. In situ evidence of rapid, vertical, irreversible transport of lower tropospheric air into the lower tropical stratosphere by convective cloud turrets and by larger-scale upwelling in tropical cyclones. *Journal of Geophysical Research-Atmospheres*, 98(D5):8665–8681, MAY 20 1993.

W. Dansgaard. Stable isotopes in precipitation. *Tellus*, 16(4):436–468, 1964.

A. Dessler, T. Hanisco, and S. Fueglistaler. Effects of convective ice lofting on H_2O and HDO in the tropical tropopause layer. *Journal of Geophysical Research*, 112: D18309, 2007.

A. E. Dessler and S. C. Sherwood. A model of hdo in the tropical tropopause layer. *Atmospheric Chemistry and Physics*, 3(6):2173–2181, 2003. doi: 10.5194/acp-3-2173-2003.

V. Dvortsov and S. Solomon. Response of the stratospheric temperatures and ozone to past and future increases in stratospheric humidity. *Journal of Geophysical Research*, 106(D7):7505–7514, 2001.

I. Folkins, M. Loewenstein, J. Podolske, S. Oltmans, and M. Proffitt. A barrier to vertical mixing at 14 km in the tropics: Evidence from ozonesondes and aircraft measurements. *Journal of Geophysical Research*, 104(D18):22095–22102, Sept. 1999.

S. Fueglistaler and P. Haynes. Control of interannual and longer-term variability of stratospheric water vapor. *Journal of Geophysical Research*, 110:D24108, 2005.

S. Fueglistaler, H. Wernli, and T. Peter. Tropical troposphere-to-stratosphere transport inferred from trajectory calculations. *Journal of Geophysical Research*, 109: 1979–1993, 2004.

T. Garrett, A. Heymsfield, M. McGill, B. Ridley, D. Baumgardner, T. Bui, and C. Webster. Convective generation of cirrus near the tropopause. *Journal of Geophysical Research*, 109(D21), NOV 6 2004. doi: {10.1029/2004JD004952}.

S. D. Gedzelman. Deuterium in water vapor above the atmospheric boundary layer. *Tellus B*, 40B(2):134–147, 1988. doi: 10.1111/j.1600-0889.1988.tb00217.x.

C. J. Gibbins. A survey and comparison of relationships for the determination of the saturation vapour pressure over plane surfaces of pure water and of pure ice. *Annales geophysicae*, 8(12):27, 1990.

J. A. Goff. Saturation pressure of water on the new Kelvin temperature scale, presented at the semi-annual meeting of the American Society of Heating and Ventilating Engineers. In *Transactions of the American Society of Heating and Ventilating Engineers*, pages 347–354, Murray Bay, Que., Canada, 1957.

J. A. Goff and S. Gratch. Low-pressure properties of water from -160 to 212 °F, presented at the 52nd annual meeting of the American Society of Heating and Ventilating Engineers. In *Transactions of the American Society of Heating and Ventilating Engineers*, pages 95–122, New York, 1946.

T. F. Hanisco, E. J. Moyer, E. M. Weinstock, J. M. St. Clair, D. S. Sayres, J. B. Smith, R. Lockwood, J. G. Anderson, A. E. Dessler, F. N. Keutsch, J. R. Spackman, W. G. Read, and T. P. Bui. Observations of deep convective influence on stratospheric water vapor and its isotopic composition. *Geophysical Research Letters*, 34(4), 02 2007.

J. Holton and A. Gettelman. Horizontal transport and the dehydration of the stratosphere. *Geophysical Research Letters*, 28(14):2799–2802, 2001.

J. Holton, P. Haynes, M. McIntyre, A. Douglas, R. Rood, and L. Pfister. Stratosphere-troposphere exchange. *Reviews of Geophysics*, 33(4):403–440, 1995.

D. Johnson, K. Jucks, W. Traub, and K. Chance. Isotopic composition of stratospheric water vapor- implications for transport. *Journal of Geophysical Research*, 106:12, 2001a.

D. Johnson, K. Jucks, W. Traub, and K. Chance. Isotopic composition of stratospheric water vapor- measurements and photochemistry. *Journal of Geophysical Research*, 106:12, 2001b.

J. Jouzel and L. Merlivat. Deuterium and oxygen 18 in precipitation: modeling of the isotopic effects during snow formation. *Journal of Geophysical Research-Atmospheres*, 89(D7):11749–11757, 1984.

D. Keith. Stratosphere-troposphere exchange: Inferences from the isotopic composition of water vapor. *Journal of Geophysical Research*, 105(D12):15167–73, 2000.

D. Kirk-Davidoff, E. Hintsa, J. Anderson, and D. Keith. The effect of climate change on ozone depletion through changes in stratospheric water vapour. *Nature*, 402 (6760):399–401, 1999.

T. Koop, B. Luo, A. Tsias, and T. Peter. Water activity as the determinant for homogeneous ice nucleation in aqueous solutions. *Nature*, 406(6796):611–614, Aug. 2000.

Z. Kuang, G. C. Toon, P. O. Wennberg, and Y. L. Yung. Measured hdo/h2o ratios across the tropical tropopause. *Geophysical Research Letters*, 30(7), 04 2003. doi: 10.1029/2003GL017023.

L. Li, G. Heymsfield, P. Racette, L. Tian, and E. Zenker. A 94-GHz cloud radar system on a NASA high-altitude ER-2 aircraft. *Journal of Atmospheric and Oceanic Technology*, 21(9):1378–1388, 2004.

C. T. Liu and E. J. Zipser. Global distribution of convection penetrating the tropical tropopause. *Journal of Geophysical Research*, 110(D23):D23104, Dec. 2005. doi: DOI10.1029/2005JD006063.

M. McCarthy, K. Boering, T. Rahn, J. Eiler, A. Rice, D. Tyler, S. Schauffler, E. Atlas, and D. Johnson. The hydrogen isotopic composition of water vapor entering the stratosphere inferred from high-precision measurements of δD-CH_4 and δD-H_2. *Journal of Geophysical Research*, 109(D7):D07304, Apr. 2004. doi: 10.1029/2003JD004003.

L. Merlivat. Molecular diffusivities of $H_2^{16}O$, $HD^{16}O$, and $H_2^{18}O$ in gases. *Journal of Chemical Physics*, 69(6):2864–2871, 1978.

L. Merlivat and G. Nief. Isotopic fractionation of solid-vapor and liquid-vapor changes of state of water at temperatures below 0 °C. *Tellus*, 19:122–27, 1967.

K. Minschwaner and A. Dessler. Water vapor feedback in the tropical upper troposphere: Model results and observations. *Journal of Climate*, 17(6):1272–1282, 2004.

E. J. Moyer, F. W. Irion, Y. L. Yung, and M. R. Gunson. ATMOS stratospheric deuterated water and implications for troposphere-stratosphere transport. *Geophys. Res. Lett*, 23:2385–2388, 1996. doi: 10.1029/96GL01489.

W. Pollock, L. E. Heidt, R. Lueb, and D. H. Ehhalt. Measurement of stratospheric water vapor by cryogenic collection. *Journal of Geophysical Research*, 85(C10): 5555–5568, 1980.

K. Rosenlof. How water enters the stratosphere. *Science*, 302(5651):1691, 2003.

V. Santacesaria, R. Carla, R. MacKenzie, A. Adriani, F. Cairo, G. Didonfrancesco, C. Kiemle, G. Redaelli, J. Beuermann, C. Schiller, T. Peter, B. Luo, H. Wernli, F. Ravegnani, A. Ulanovsky, V. Yushkov, N. Sitnikov, S. Balestri, and L. Stefanutti. Clouds at the tropical tropopause: A case study during the APE-THESEO campaign over the western Indian Ocean. *Journal of Geophysical Research*, 108 (D2), JAN 18 2003. doi: 10.1029/2002JD002166.

D. S. Sayres, E. J. Moyer, T. F. Hanisco, J. M. S. Clair, F. N. Keutsch, A. O'Brien, N. T. Allen, L. Lapson, J. N. Demusz, M. Rivero, T. Martin, M. Greenberg, C. Tuozzolo, G. S. Engel, J. H. Kroll, J. B. Paul, and J. G. Anderson. A new cavity based absorption instrument for detection of water isotopologues in the

upper troposphere and lower stratosphere. *Review of Scientific Instruments*, 80 (4):044102, 2009. doi: 10.1063/1.3117349.

D. S. Sayres, L. Pfister, T. F. Hanisco, E. J. Moyer, J. B. Smith, J. M. St Clair, A. S. O'Brien, M. F. Witinski, M. Legg, and J. G. Anderson. Influence of convection on the water isotopic composition of the tropical tropopause layer and tropical stratosphere. *Journal of Geophysical Research*, 115:D00J20, Sept. 2010. doi: DOI10.1029/2009JD013100.

S. Scott, T. Bui, K. Chan, and S. Bowen. The meteorological measurement system on the NASA ER-2 aircraft. *Journal of Atmospheric and Oceanic Technology*, 7 (4):525–540, 1990.

S. Sherwood and A. Dessler. A model for transport across the tropical tropopause. *Journal of the Atmospheric Sciences*, 58(7):765–779, 2001.

D. Shindell. Climate and ozone response to increased stratospheric water vapor. *Geophysical Research Letters*, 28(8):1551–1554, 2001.

C. Smith, J. Haigh, and R. Toumi. Radiative forcing due to trends in stratospheric water vapour. *Geophysical Research Letters*, 28(1):179–182, 2001.

S. Solomon. *Climate Change 2007: the physical science basis. Contribution of Working Group I to the Fourth Assessment Report of the Intergovernmental Panel on Climate Change*. Cambridge University Press, Cambridge, United Kingdom and New York, NY, USA, 2007.

J. M. St. Clair, T. F. Hanisco, E. M. Weinstock, E. J. Moyer, D. S. Sayres, F. N. Keutsch, J. H. Kroll, J. N. Demusz, N. T. Allen, J. B. Smith, J. R. Spackman, and J. G. Anderson. A new photolysis laser-induced fluorescence instrument for the detection of H_2O and HDO in the lower stratosphere. *Review of Scientific Instruments*, 79(6):064101, June 2008. doi: 10.1063/1.2940221.

G. Stephens. Cloud feedbacks in the climate system: A critical review. *Journal of Climate*, 18(2):237–273, 2005.

C. R. Webster and A. J. Heymsfield. Water isotope ratios D/H, $^{18}O/^{16}O$, $^{17}O/^{16}O$ in and out of clouds map dehydration pathways. *Science*, 302(5651):1742–1745, Dec. 2003.

E. Weinstock, E. Hintsa, A. Dessler, J. Oliver, N. Hazen, J. Demusz, N. Allen, L. Lapson, and J. Anderson. New fast-response photofragment fluorescence hygrometer for use on the NASA ER-2 and the Perseus remotely piloted aircraft. *Review of Scientific Instruments*, 65(11):3544–3554, NOV 1994.

E. M. Weinstock. Personal communication, 2009.

D. M. Winker and C. R. Trepte. Laminar cirrus observed near the tropical tropopause by lite. *Geophysical Research Letters*, 25(17):3351–3354, Sep 1998.

Chapter 4

Glyoxal LIP Instrument & Results

> I observed, partly in the fire, which had ceased to blaze, a perfectly regular elliptical ring of light, about five inches in its shortest diameter, six or seven in its longer, and from one eighth to one quarter of an inch wide. It was fully as bright as the fire, but not reddish or scarlet like a coal, but a white and slumbering light, like the glowworm's. I could tell it from the fire only by its whiteness. I saw at once that it must be phosphorescent wood, which I had so often heard of, but never chanced to see.
>
> *The Maine Woods: The Allegash and East Branch*
> Henry David Thoreau

4.1 Glyoxal Instrument Overview

An instrument to measure glyoxal by laser-induced phosphorescence (LIP) was developed for use in the Community Atmosphere-Biosphere Interactions Experiment (CABINEX) field campaign during the summer of 2009. The instrument was based on the detection scheme of the Madison Glyoxal LIP instrument (Huisman et al., 2008) developed by the Keutsch Group at University of Wisconsin-Madison, a collaborator during the CABINEX field campaign.

4.1.1 Measurement Technique

Glyoxal is detected by a laser-induced phosphorescence scheme based on the absorption of visible light:

$$\mathrm{S_0(^1A_g)} + h\nu_{440\,\mathrm{nm}} \rightarrow \mathrm{S_1(8_0^1\,{}^1A_u)} \tag{4.1}$$

$$\mathrm{S_1(^1A_u)} + \mathrm{M} \rightarrow \mathrm{T_1(^3A_u)};\ \Phi_{\mathrm{S_1\rightarrow T_1}} = 1 \tag{4.2}$$

$$\mathrm{T_1(^3A_u)} \rightarrow \mathrm{S_0(^1A_g)} + h\nu_{521\,\mathrm{nm}}. \tag{4.3}$$

Glyoxal is initially excited into its first excited electronic (singlet) state by 440 nm (22710 $\mathrm{cm^{-1}}$) laser light. This strong absorption band corresponds to a transition into the ν_8 C–H wagging vibrational mode (Cossart-Magos, 1978) of the excited state and has a fundamental energy 735 $\mathrm{cm^{-1}}$ above the $\mathrm{S_1}$ zero-point level (Pebay Peyroula and Jost, 1987).

The two major decay pathways from this $\mathrm{S_1}$ state are fluorescence and collision induced intersystem crossing to the triplet ($\mathrm{T_1}$) state. Isomerization of *trans*-glyoxal

to *cis*-glyoxal is a possible deactivation pathway of the S_1 state, however Cossart-Magos (1978) found that the rate of photo-isomerization was at least 2 – 3 orders of magnitude less than the total decay rate in the low pressure collision-free regime so that this pathway can, effectively, be neglected.

At very low pressures the emission is dominated by fluorescence; as the pressure increases fluorescence is quenched and the emission spectrum becomes one of T_1 phosphorescence. Collisional relaxation of the S_1 state is insensitive to the identity of the collision partner (Anderson et al., 1971) and the dominant second-order decay is $S_1 \rightarrow T_1$ intersystem crossing (Anderson, 1973). At pressures above 2 Torr the phosphorescence yield from intersystem crossing approaches unity and the phosphorescence signal intensity is no longer pressure dependent (Beyer and Lineberger, 1975). The sampling cell of the instrument is held constant at 100 Torr, well above the high-pressure threshold.

The triplet ^3A_u is known to proceed via either a radiative (phosphorescence) or non-radiative (collisional deactivation) pathways to the ground state. The collision-free radiative lifetime of the ^3A_u state is 3.29 ± 0.1 ms; deactivation by collision with O_2 is the primary non-radiative process and has a measured rate constant of $3.0 \pm 0.1 \times 10^{-3}$ μs^{-1} $Torr^{-1}$ (Yardley, 1972). A phosphorescence lifetime on the order of 15.8 μs is estimated for the sampling conditions at 100 Torr. The long lifetime of phosphorescence at these sampling conditions allows for an isolated gated detection scheme where fast interferences (Raman, Rayleigh and particle scattering and competing fluorescence) can be neglected.

4.1.2 Hardware Overview

The non-reactive nature of glyoxal and the relatively liberal constraints of a ground-based measurement allowed for the rapid development of the instrument from a series of largely isolated subsystems. Packaging of the instrument into a standard instrument rack was made possible by the opportunity afforded by being located in an indoor laboratory at the sampling site. The subsystems of the instrument are: gas handling, detection, calibration and data acquisition.

4.1.2.1 LIP Axis

The detection axis of the glyoxal instrument consists of a multi-pass White cell (WC), the same design used in the Harvard NO_2 LIF instrument (Perkins et al., 2001). However, unlike its use in NO_2 and IO experiments, the detection axis is not mounted in-line with the flow axis. Gas samples are brought into and out of the cell through flange plates connected to teflon tubing. The flange plates supply a gas flow that is orthogonal to the optical path in the horizontal plane. A photomultiplier tube (PMT) assembly is mounted orthogonal to both the flow and optical path in the vertical orientation. Only a region in the center of the flow and optical path is imaged by the PMT. The zero point energy of the ^3A_u state lies 3514 cm^{-1} below the excitation wavelength (Cossart-Magos, 1978), such that detection is red-shifted closer to the wavelength of maximum sensitivity for the PMT.

A White cell is made from three spherical concave mirrors, all of which have the same radius of curvature. The distinct multi-pass spot pattern on the entrance mirror is generated by the rule that object and image points near the center of curvature of

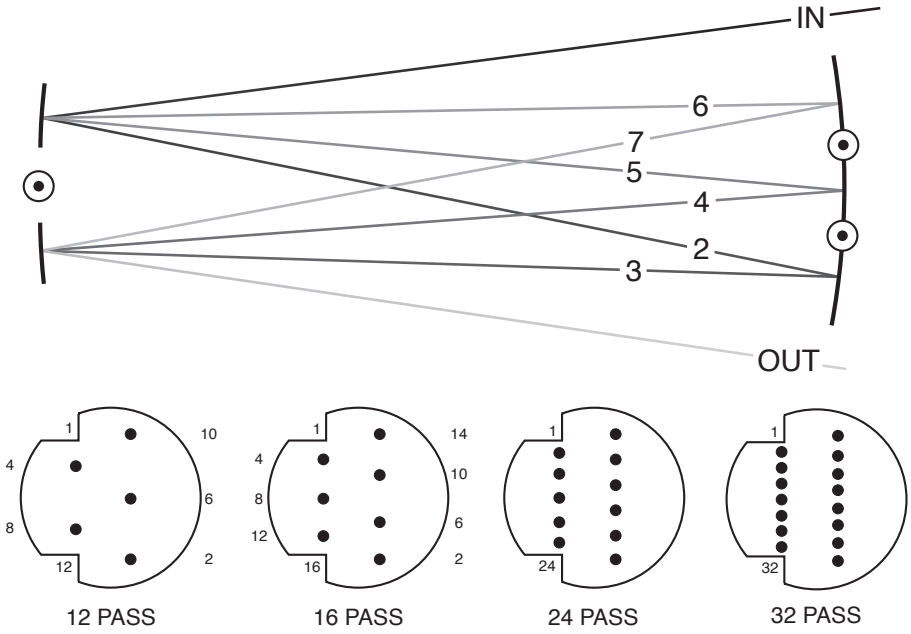

Figure 4.1: The optical path through an 8-pass configuration of a three mirror White cell is shown in the upper figure. The pass number is noted and the overall path is shown by a gradient from dark-to-light from visual clarity. The centers of curvature of the mirrors are shown by the circles. The spot configuration on the entrance mirror for 12-, 16-, 24- and 32-pass configurations of a White Cell. Note that the 12- and 16-pass configurations display the corresponding number of passes at each spot on the entrance mirror. (Adapted from White (1942).)

a spherical mirror always lie on a straight line whose midpoint falls on the center of curvature (White, 1942).

The number of passes is determined by the separation of the centers of curvatures of the smaller rear twin mirrors. The total number of passes P is related to the total number of spots n: $P = 2n+2$, where n is any odd integer. The relationship between the number of spots on the right side n_r versus the left side n_l of the mirror (for the mirror configuration shown in the lower panel of Figure 4.1) for any number of total

spots is then $n_r : n_l \equiv (n/2 + 1/2) : (n/2 - 1/2)$.

A 32-pass configuration of the WC is used in the instrument. Instrument sensitivity and accuracy are directly tied to the WC configuration as calibrations are carried out only with the designed 32-pass configuration. While the WC is robust to changes in the multipass configuration, a simple check of the spot count is needed to ensure that the optical configuration is not affected by shipping.

Glyoxal is detected by measuring the difference counts between "online" and "offline" positions. A high-resolution absorption spectrum of glyoxal is shown in Figure 4.2, where the online and offline positions are indicated.

The laser is scanned to the online position for 40 seconds then offline for 20 seconds. Glyoxal phosphorescence counts are detected at a rate of 1 Hz and this data is post-processed to obtain final data at a 1 minute acquisition rate by taking the difference the between the mean online counts and the mean offline counts for both the period preceding and following an online period. Taking offline periods on either side of an online event removes any potential trend in the background counts. A full spectral scan precedes the online-offline procession to ensure that there has been no shift in the position of the online and offline positions over time. A full spectral scan takes roughly 7.5 minutes and is repeated every time there is a change in the sampling inlet which occurs on the timescale of 25 minutes.

4.1.2.2 CRD Axis

Theoretical considerations of cavity ringdown spectroscopy are discussed in Section 2.3.1.1. A separate cavity ringdown (CRD) axis is packaged on the underside

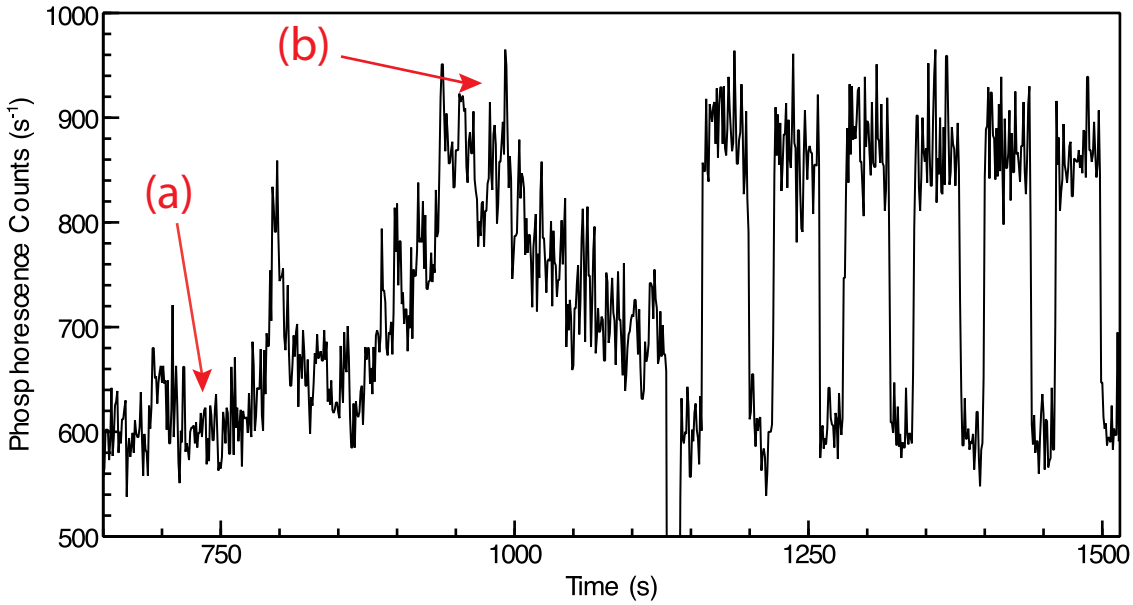

Figure 4.2: A full spectrum scan precedes the alternating procession between online and offline positions from which the difference counts are calculated and are directly related to the concentration through a calibration factor. Note that the raw PMT signal is shown and the laser power is not constant through the spectral range. The online position can be seen near 950 s, indicated by (a) at 440.26 nm, and the offline position near 750 s, indicated by (b) at 440.23 nm. The large loss in signal near 1150 s is from the mechanical shutter which blocks the laser so that background due to room light and dark counts can be determined, this is on the order of 20 s^{-1}.

of the optical table and is used for calibration. A section of 3/8 inch OD teflon tubing determines the overall length of the cell. Two FluoroPel coated stainless steel run tees (Swagelok, SS-600-3TMT) are attached to the teflon tubing providing a T-junction where the sample input and output ports are at right angles to the cell. A 1/4 inch male NPT fitting inline with with a 3/8 inch OD Swagelok fitting allows for the direct attachment of a Quick Flange plate which couples to a two-axis mirror mount. Highly reflective 1 inch mirrors ($R \geq 99.995$ %) (Los Gatos Research, now CRD Optics, 901-0010-0440) with a 1 meter radius of curvature complete the cavity. An aluminum block that runs the length of the tubing, including the run tees, encapsulates the tubing maintaining straightness and has heaters mounted to it to maintain a constant cell temperature of 30 °C. The overall length of the cavity is 47.82 cm, however the effective path length, 27.61 cm, is determined by the distance between the input and output ports. The effective path length has been verified by NO_2 calibrations (Keutsch, 2010).

Proper alignment of the laser with the cavity results in the desired behavior of the laser coupling completely to the fundamental longitudinal mode of the cavity and not to higher-order off-axis modes. At 440 nm the Ti:Sapphire laser has a bandwidth, or laser linewidth (llw), of approximately 1.2 GHz (0.04 cm^{-1}; 7.8×10^{-4} nm), while the free-spectral range (longitudinal mode spacing) of the ringdown cavity is approximately 300 MHz (see eq. 2.37). Since $\Delta\nu_{\text{cavity}} \ll \Delta\nu_{\text{llw}}$ multiple cavity modes are excited by the laser and the intensity fluctuation in the output power due to changes in the cavity length will be minimal. Furthermore, the CRDS technique is insensitive to changes in the intensity of the laser as it is the first order decay which

is fit. However, higher-order transverse electromagnetic (TEM) modes are generated by misalignment resulting from transverse displacement and mismatch of waist size of the input beam with respect to the cavity (Anderson, 1984). A two-lens telescope is used to match the laser beam waist to the cavity beam waist D, which is given by (Kogelnik and Li, 1966):

$$D^2 = \frac{\lambda}{2\pi}\sqrt{d\,(2r-d)} \tag{4.4}$$

where λ is the wavelength, r is the radius of curvature of two identical mirrors and d is the mirror separation. Accurate alignment of the input beam with the axis of the cavity should then eliminate higher-order TEM modes. "Transverse mode beating" from these higher-order modes can not be completely eliminated from the cavity and manifest as modulations in the decay profile as a result of their different path through the cavity. Modulations are fast with respect to the decay time and have little influence on the overall fits.

The minimum detectable absorption coefficient α by the CRDS technique is given by (Vogler and Sigrist, 2006; Zalicki and Zare, 1995):

$$\alpha_{\min} = \left(\frac{1-R}{L}\right)\left(\frac{\Delta\tau}{\tau}\right). \tag{4.5}$$

For a modest $(\Delta\tau/\tau)_{\min} = 0.5 \times 10^{-3}$ and a specified mirror reflectivity of 99.995 %, the minimum detectable absorption (i.e., αL) in the glyoxal CRD cell is 2.5×10^{-7}. This corresponds to 1.8×10^{10} molecules cm^{-3} or, equivalently, 683 ppm at 760 Torr. While CRDS is not sensitive enough to measure ambient glyoxal, it proves to be a sensitive method yielding direct absolute calibrations at higher mixing ratios.

The CRDS axis is used exclusively for purposes of calibration, both in the field and the laboratory, to determine the concentration of a glyoxal in a bulb. The standard calibration procedure is described in Section 4.1.2.4.

4.1.2.3 Data Acquisition

Data acquisition and system control are provided through a pair of commercial data acquisition boards (National Instruments, PCI-6221 and PCI-6229). The PCI-6229 is nearly identical to the PCI-6221, except that it doubles the number of available channels across two connectors. However, the digital counters are not duplicated on the second connector. The IO/glyoxal main computer now contains two PCI-6229 cards after the failure of the PCI-6221 card. This essentially provides a redundant card in all but the digital counter channels. Each card provides a total of: 32 single-ended and 16 differential analog input channels with 16-bit resolution and 250 kS/s sampling rate; 4 analog output channels with 16-bit resolution and 833 kS/s update rate; 48 bi-directional digital input/output channels with a maximum 1 MHz clock rate; and 2 counters with 32-bit resolution with a maximum source frequency of 80 MHz.

The data acquisition cards are interfaced to a custom main distribution panel (main DP) designed in-house. The main DP interfaces to all the components through appropriate connectors, in addition to providing +5, ±15 and +24 VDC power. All input/output channels from the data acquisition cards are buffered at the main DP. The instrument is controlled by custom software written in LabView (National Instruments), a graphical programming environment. Post-processing to obtain final

data is done with MATLAB (MathWorks), a high-level interactive language.

4.1.2.4 Calibration

Gas-phase glyoxal suitable with purity suitable for calibration is generated by the procedure outline by Kroll et al. (2005). White crystalline polymeric glyoxal in the form of a trimer dihydrate (Sigma Aldrich) is heated under vacuum in the presence of P_2O_5 until bubbling occurs, indicating the release of monomeric glyoxal. The desired monomer is condensed in a LN_2 cold trap producing a yellow crystal. This crystalline solid is sublimed from the cold trap by removing the LN_2 and transferred into 12.5 L evacuated glass bulb as monomeric gas-phase glyoxal. Glyoxal is diluted and the bulb slightly pressurized to 800 Torr by the addition of UZA. A final concentration of glyoxal with mixing ratios on the order of ppm in the bulb is achieved.

Glyoxal in its monomeric gas-phase form is stable in the absence of light and humidity. Great care is taken to remove water from the surfaces of glassware by heating it repeatedly with a butane flame under vacuum. The bulb is covered by black-out cloth and is stored in a dark environment.

Since the concentration of glyoxal in the bulb can decrease as a result of polymerization or photolysis, the bulb concentration must be determined prior to any subsequent calibration of the LIP detection axis. Cavity ringdown spectroscopy is used to determine the concentration of glyoxal in the bulb. During a ringdown calibration, the laser is redirected from the LIP axis to the CRDS axis and the decay of each laser pulse is monitored by a 125 MHz silicon photodiode detector (New Focus, 1801-FS). Each ringdown trace is acquired and digitized by a 12-bit, 50 MS/s

A/D card (CompuScope, 1250) and fit by custom software on a dedicated computer. The software fits each decay with to a single parameter exponential function, with the fit parameter being the cavity time constant (Equation 2.32). However, the fit parameter is ultimately reported in terms of "loss per pass" by rearrangement of equation 2.32:

$$\text{loss per pass (ppm)} \equiv \left[\frac{L}{c\tau}\right] \times 10^6 = [1 - R + \alpha(\nu)L] \times 10^6 \tag{4.6}$$

where this newly defined quantity is also referred to as "ppm loss." When the CRD axis is evacuated, no absorbers are present and the ringdown time constant (and by extension the ppm loss) reflects the reflectivity of the mirrors. In the case of 99.995 % reflective mirrors, a loss per pass of 50 ppm is expected.

The absorption of any sample is given by the difference between the ppm loss in the presence of an absorber and the ppm loss in the absence of an absorber (i.e., background losses): $\alpha(\nu) = [(\text{ppm loss}_{sample}) - (\text{ppm loss}_{bckgnd})]/L \times 10^{-6}$, where L is the absorption path length. A background scan across the spectrum is carried out in UZA at a cell pressure of 600 Torr. Glyoxal is then added to the cell from the bulb with varying flow rates, and the dilution flow correspondingly reduced to maintain a cell pressure of 600 Torr, such that the concentration of glyoxal in the CRD cell is varied. The concentration of glyoxal (molecules cm^{-3}) is directly related to the measured absorption coefficient by the Beer-Lambert law

$$[\text{glyoxal}]_{cell} = \frac{\alpha(\nu)}{\sigma(\nu)} \tag{4.7}$$

where $\sigma(\nu)$ is the absorption cross section (cm^2 $molecule^{-1}$). This is closely related to the relationship in equation 2.27, however the line parameters are not known and the absorption cross section is determined from a high-resolution reference spectrum (Volkamer et al., 2005).

To determine the concentration of glyoxal in the bulb, the dilution of glyoxal must be accounted for. The bulb is diluted by two sources upon entry into the CRD cell: a dilution flow which is well mixed prior to entry into the CRD cell; and a purge flow that is split equally between the two mirrors. Only the purge at the mirror near the gas entry-port is mixed with the pre-diluted glyoxal. The purge on the mirror near the gas-exit port is assumed to have no effect on the glyoxal in the ringdown cell as a result of no turbulent mixing. The concentration of glyoxal in the bulb is then:

$$[\text{glyoxal}]_{bulb} = [\text{glyoxal}]_{cell} \left(\frac{Q_{bulb} + Q_{dilute} + \frac{1}{2} Q_{purge}}{Q_{total}} \right) \tag{4.8}$$

where Q refers to the flow rate (SLM) of each respective flow controller.

Calibration of the phosphorescence signal is carried out in the LIP axis where diluted glyoxal in a bulk UZA flow is added. A flow meter (Honeywell, AWM5104VN) downstream of the LIP detection axis measures the total flow rate, while glyoxal is added from the calibration bulb in known quantities by a small mass flow controller (MKS, 1197A series). Pressure in the LIP detection axis is maintained at sampling conditions of 100 Torr by adjusting the bulk flow to changes in the flow from the bulb.

Laser power is attenuated by a neutral density filter as the minimum glyoxal concentration is on the order of 100 ppt. A linear fit of power normalized difference

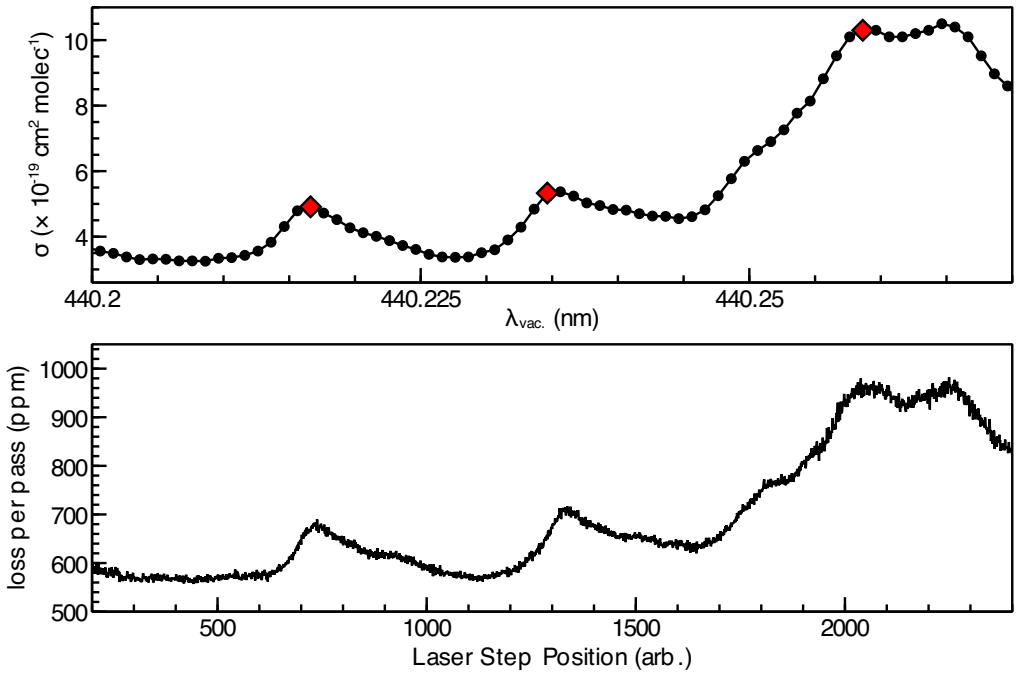

Figure 4.3: (a) Reference spectrum used to determine glyoxal absorption cross section at the three points indicated by the red diamonds. The cross sections at these reference points are 1.03×10^{-18}, 5.33×10^{-19} and 4.91×10^{-19}, from right-to-left (long-to-short wavelength). [Data from Volkamer et al. (2005)] (b) A typical ringdown spectrum for a calibration. This scan corresponds to a mean cell concentration of 1.16 ppm glyoxal determined from the reference points, which gives a bulb concentration of 22.7 ppm. The background scan is not shown. A linear fit of several CRD scans at varying cell concentration gives the standard bulb concentration; for this calibration the bulb was determined to have a concentration of 22.9 ± 1.4 ppm.

counts to the known glyoxal concentration in the LIP axis yields a calibration factor in terms of (s ppt)$^{-1}$. The uncertainty in the linear fit can be determined by analysis of the variance (var) and covariance (cov) of each plot with the method described by Higbie (1991), where the independent variable x refers to the glyoxal concentration (ppt) and the dependent variable y refers to the phosphorescence counts (s^{-1}).

The correlation coefficient R is found from the covariance and variance

$$R = \frac{\mathrm{cov}(x,\, y)}{[\mathrm{var}(x)\mathrm{var}(y)]^{1/2}}. \tag{4.9}$$

The slope can be similarly determined

$$\mathrm{slope} = \frac{\mathrm{cov}(x,\, y)}{\mathrm{var}(x)}, \tag{4.10}$$

and, finally, the uncertainty in the slope σ can be found

$$\sigma_{\mathrm{slope}} = \frac{|\mathrm{slope}|\tan[\arccos(R)]}{(N-2)^{1/2}} \tag{4.11}$$

where N is the number of points in the linear fit.

4.1.2.5 Sampling Method

Glyoxal is non-reactive with respect to polytetrafluoroethylene (PTFE) and perfluoroalkoxy (PFA), so tubing made from these materials are used throughout. As the surfaces of PTFE and PFA are inert, long lengths of tubing can be used to draw glyoxal into the detection axis. Glyoxal is taken up by the surfaces of the walls,

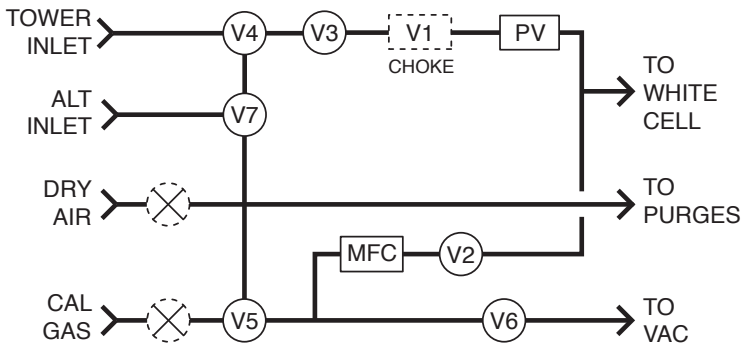

COMMAND	V4	V5	V7	V2	V3	V6
TOWER INLET	O	O	O	O	O	O
ALT INLET	I	O	O	O	O	O
CAL GAS	I	I	O	I	O	O
CAL EVAC	O	I	O	I	I	I
CAL PURGE	O	O	O	I	I	O

Figure 4.4: The glyoxal valve deck is composed of: two- and three-way solenoid valves (V2–V7); a manual choke valve (V1); manual shutoff valves on the dry air and calibration gas inputs; a mass flow controller (MFC) on the calibration gas input; and a pinch valve (PV) to maintain a sampling pressure of 100 Torr. The command sequence for desired operating modes is shown on the right. Valves can be controlled manually through switches on the Main DP or remotely through software control.

however, the equilibration time with the walls is much faster than the change in the ambient concentration so this does not affect measurements.

A valve deck composed of two- and three-way solenoid valves allows for alternate sampling between inlets. During regular sampling the inlets are continuously switched between the tower inlet and alternate inlet with a period of 30 minutes. During the CABINEX field campaign the "tower inlet" was connected by roughly 2 meters of 1/4 inch PFA tubing to a glass manifold in the ceiling of the laboratory building. The laboratory sits adjacent to a 31 meter tower and the glass manifold ($\sim$ 2 inch dia.) runs up the tower where ambient air is sampled from a height of 34 meters. Ambient air is drawn into the manifold by a large pump resulting in a reduced pressure in the manifold. The "alternate inlet" was connected to approximately 30 meters of 1/2 inch PTFE tubing which ran from the valve deck to a small

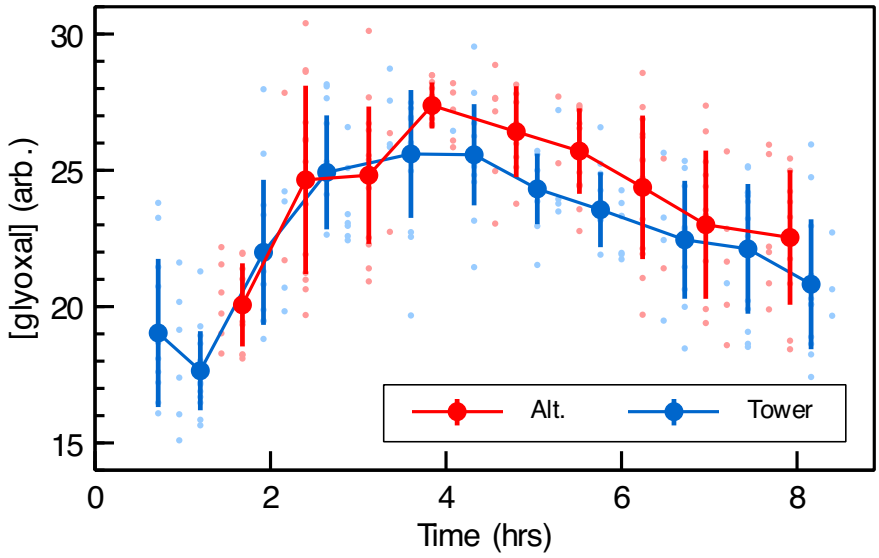

Figure 4.5: Sampling intercomparisons between an inlet directly open to room air (Tower; blue) and an inlet drawing in room air through 30 meters of PTFE tubing (Alt.; red) were performed to ensure that no glyoxal was lost to the walls of the PTFE tubing. Glyoxal in room air varies slowly so any loss in the Alternate inlet relative to the Tower inlet is an indication of loss to the walls of the tubing, not changes in ambient concentration. Minute data for each inlet is shown by the dots and the vertical bars represent $\pm 1\sigma$ of the mean. Glyoxal is on the order of 10 ppt.

6 meter tower atop the WSU trailer. Sampling between inlets located below and above the canopy allows for gradient measurements. A 1 minute delay during data acquisition is added between inlet switching to ensure that ambient air is being sampled and allowing the pinch valve to establish the correct pressure in the detection axis.

Prior to sampling ambient glyoxal from the tower (glass manifold) and within the canopy (30 m PTFE inlet) an intercomparison between inlets was performed to verify that glyoxal uptake on the walls of the PTFE tubing would not affect the measurement. One inlet (tower) was opened directly to room air at the solenoid

valve, while a second inlet (alt) was connected to approximately 30 m of 1/2 inch PTFE tubing and also sampled room air. The concentration of glyoxal in room varies slowly so any decrease in the signal of the alternate inlet is due to loss of glyoxal onto the walls of the PTFE tubing. Approximately half-way through the sampling period ($\sim$ 5 hours, Fig. 4.5) a funnel covered by a mesh screen was added to the end of the tubing; no influence in the signal was detected by this addition. The mesh-covered funnel at the tubing input was the configuration used throughout the campaign as it prevented the uptake insects an small debris into the sampling line. No loss in signal is apparent from the addition of PTFE tubing. Tower inlet data was interpolated into the timebase of the alternate inlet by averaging the nearest neighbors and the maximum difference between the two inlets was found to be less than 8 % over the entire evaluation period. Additionally, optical noise ($\pm 1\sigma$) during during each 25 minute sampling period always exceeds the difference in the mean concentration between the two inlets.

4.2 CABINEX Field Mission

Deforestation in the United States reached its maximum by the 1920s. Most (about 90 %) of the virgin forests present prior to 1600, before the vast expansion of population across North America, had been cleared. Since the 1920s forest coverage has remained relatively constant covering roughly 33 % of the continental United States land area, which represents approximately 20 % of the world's forest ecosystems in terms of area. Continued deforestation in the western United States has

been offset by the regeneration of forest in the southern and, particularly, northern states. Since management practices were applied in the early 20$^{\text{th}}$ century, 2.4 million hectares of new forest (an area roughly equivalent to the size of New Hampshire) can be attributed to the Midwest alone (Smith et al., 2004). However, the composition of this new (second-growth) forest differs from the virgin (old-growth) forests that it has replaced. As these second-growth forests age they will become more characteristic of old-growth forests as early growth species are replaced in the natural succession of the forest.

Forest ecosystems are important components of the global carbon cycle: roughly 30 % (3 PgC yr^{-1}) of all annual CO_2 emissions are absorbed by net growth in forests (Canadell et al., 2007) and forest themselves store twice the amount of carbon as the atmospheric sink (Solomon, 2007). Undoubtedly forests will continue to play an important role in future carbon mitigation through careful management. However, the complexity in the coupled forest-atmosphere system cast uncertainty into any future predictions.

As early as 1960 Went (1960) recognized that plants were capable of releasing a substantial amount of volatile organic compounds into the atmosphere. With no known enzymatic pathways capable of breaking down isoprene derivatives, produced by biophysical plant activities, release into the atmosphere was suggested as the only plausible loss mechanism for such compounds.

Biogenic VOC emissions vary with species, where isoprene is primarily emitted by deciduous trees and α- and β-pinenes are the primary emission of conifers (Rasmussen and Went, 1965). Isoprene is unique amongst the BVOCs as it is a direct by-product

of photosynthesis: its emission is dependent on both light and temperature. This is contrasted with the terpenoids (e.g., terpenoids) which are associated with leaf oils and plant resins, emissions are dependent on the vapor pressure of these compounds and are therefore only dependent on temperature.

Isoprene and its derivatives (terpenes, carotenoids, rubber and phytol) are olefins which lend to them short atmospheric lifetimes as a result of their susceptibility to rapid OH, NO_3 and ozone oxidation. Although isoprene or α- and β-pinene are the dominant BVOCs in forest there is ample observational evidence suggesting that often more than half of the VOC mass emitted by vegetation is composed of other compounds (Isidorov et al., 1985; Singh and Zimmerman, 1990).

4.2.1 Motivation

The Community Atmosphere-Biosphere Interactions Experiment (CABINEX) field campaign was based at the University of Michigan Biological Station (UMBS) forest near Pellston, MI during July/August 2009. The field campaign was motivated by the fact that forests are large sources of biogenic volatile organic carbons (BVOCs). The importance of forests on a global scale is readily apparent when the magnitude of VOCs they are responsible for releasing is accounted for; modeling estimates place the emission of VOCs from natural sources 7 times larger than anthropogenic VOC emissions and twice that of methane on a global scale (Guenther et al., 1995). VOCs are only removed by three possible pathways: oxidation to CO or CO_2; wet or dry deposition; or by formation of secondary organic aerosols (SOA), which are ultimately removed by oxidation or deposition. While there is much un-

certainty in annual VOC budgets it is estimated that one-third is made up from isoprene alone (Goldstein and Galbally, 2007). Understanding and predicting the future role of forests is complicated by changes in their composition, resulting from both a changing climate as well as their natural evolution.

A large scale forest disturbance designed to mimic accelerated forest ecological evolution was implemented in the UMBS forest in 2008. Over 6700 aspen and birch trees, representing more the 35 % of the canopy leaf area index, were girdled over an area of 82 acres as part of the Forrest Accelerated Succession Experiment (FASET). Girdling is a process where bands of bark are removed from trees to inhibit the flow of carbohydrates from the leaves to the roots. This eventually leads to the slow decay of the tree as the supply of carbohydrates in the roots is depleted and regeneration from sprouting is prevented.

While timing of the CABINEX field mission was driven by forest succession experiment (FASET), virtually no impact on the health and prevalence of the aspen population has been observed (Bertman, 2009); the aspen and birch continued to thrive during summer of 2009. As a result, the campaign represents measurements made in a characteristically even-aged second-growth forest with successional species still confined to the understory and the transition to an uneven-aged mixed deciduous-conifer forest largely incomplete. The forest ecology remains nearly identical to 1998 when a smaller scale mission aimed at investigating oxidation processes in the forest was carried out.

With the minimal impact of successional hardwood and pine species on the UMBS forest, the local atmospheric chemistry remains to be dominated by isoprene. An

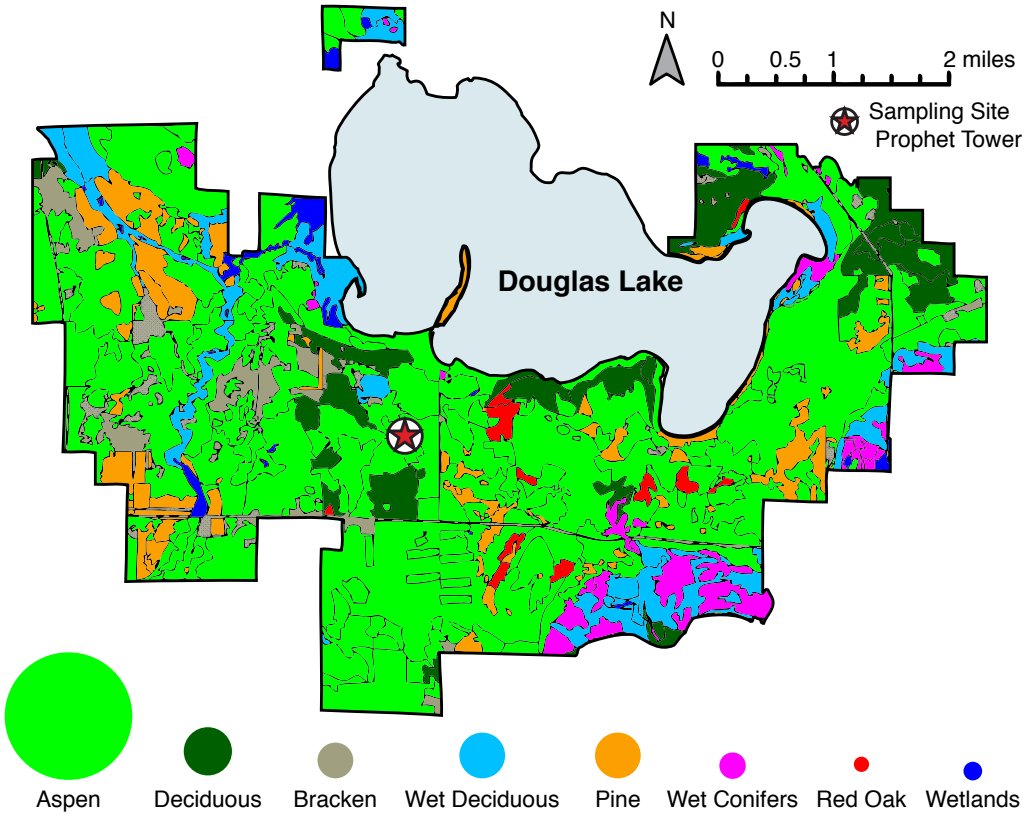

Figure 4.6: Cover types surrounding Douglas Lake on UMBS property. The area surrounding the PROPHET tower is dominated by aspen, where is covers more than 7000 acres of UMBS property. The next most abundant plant types are deciduous, wet deciduous and pine each covering roughly 1000 acres. The area of each plant type is proportional to the area it covers on the UMBS property. [Adapted from Barnes (2011)]

isoprene dominated forest becomes a unique environment to measure glyoxal as it is a ubiquitous intermediate of isoprene oxidation.

Glyoxal (CHOCHO) is the smallest α-dicarbonyl and can be readily detected by laser-induced phosphorescence. Historically, it has been viewed as a secondary and later stage oxidation product but there is new evidence from chamber studies which indicate the presence of pathways leading to direct formation during isoprene oxidation (Galloway et al., 2011).

Modeling studies confirm the importance of North American deciduous forests, such as that encountered at the University of Michigan Biological Station, to the global distribution of glyoxal. Fu et al. (2008) simulated the global daytime distribution of glyoxal at the surface with a GEOS-Chem model and found that the North American contribution, particularly across the Midwest and Northeast, to global loading of glyoxal becomes pronounced during the boreal summer. Globally, surface glyoxal concentrations were highest in biomass burning and isoprene-rich regions. In the wintertime there is a marked decrease of glyoxal in vegetated regions with the anthropogenic contribution dominating: high glyoxal concentrations are coincident with polluted regions.

While glyoxal serves as a proxy for VOC oxidation, it is the impact of local photochemistry in regional forests on air quality that primarily motivates such a measurement. Large emissions of BVOC coupled with their subsequent oxidation are capable of heavily influencing the level of ozone. Despite Blodgett Forest Research Station being located in a typically coniferous forest, prevailing daytime winds are able to influence the site with remote anthropogenic (VOC & NO_x) and biogenic

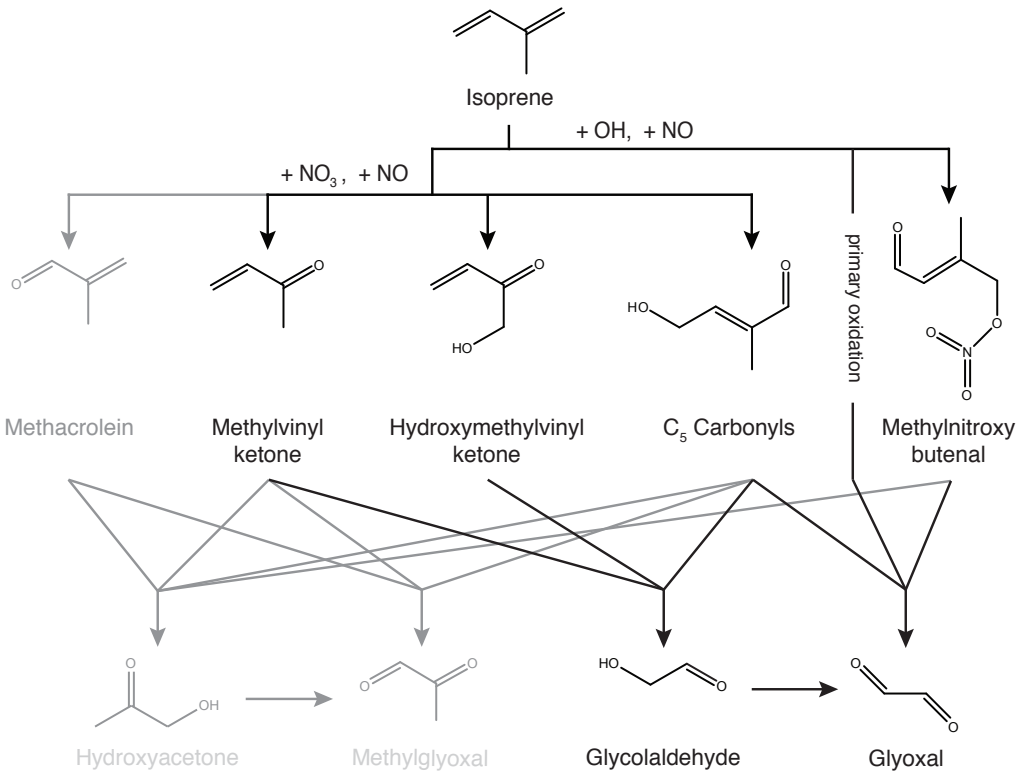

Figure 4.7: Glyoxal is a ubiquitous intermediate in the oxidation of isoprene, generated through various pathways and as a multi-generational oxidation product. Pathways leading to the formation of methylglyoxal are shown in gray. A potential primary oxidation pathway to glyoxal has been suggested, a result of data from chamber studies. [Figure adapted from Fu et al. (2008)]

(isoprene) air masses from California's Central Valley and downwind oak forests, respectively. In Blodgett Forest, isoprene oxidation was found to be responsible for between 40 – 70 % of the total ozone in the region and the ozone forming potential of isoprene was highly modulated by NO_x concentrations (Dreyfus et al., 2002).

The University of Michigan Biological Station is, by contrast, located in a remote region near the tip of Michigan's lower peninsula and is seldom influenced by air masses originating from populated areas. Anthropogenic influence on photochemistry and air quality at the site was limited to air masses originating from industrialized regions of the Great Lakes and Midwest (Fig. 4.8.)

4.2.2 Mission Overview

Within the UMBS Forest, two towers have been erected. A 46 m tower, active since 1999, that is part of the AmeriFlux network designed to study micrometeorological fluxes and carbon cycling in the forest environment. A 31 m tower, in operation since 1997, is the platform for which the Program for Research Oxidants: Photochemistry, Emissions and Transport (PROPHET) is based. It is the PROPHET tower which hosted the CABINEX mission and a previous intensive field campaign in 1998 (Carroll et al., 2001).

The PROPHET tower has a pyrex intake manifold that runs from a temperature controlled laboratory, that sits adjacent to the tower, along the height of the tower. The manifold extends above the tower, giving an intake height of 35 m. The UMBS Forest has a mean canopy height of 21 m. Washington State University (WSU) provided a mobile laboratory, designed to make a variety of measurements, that was

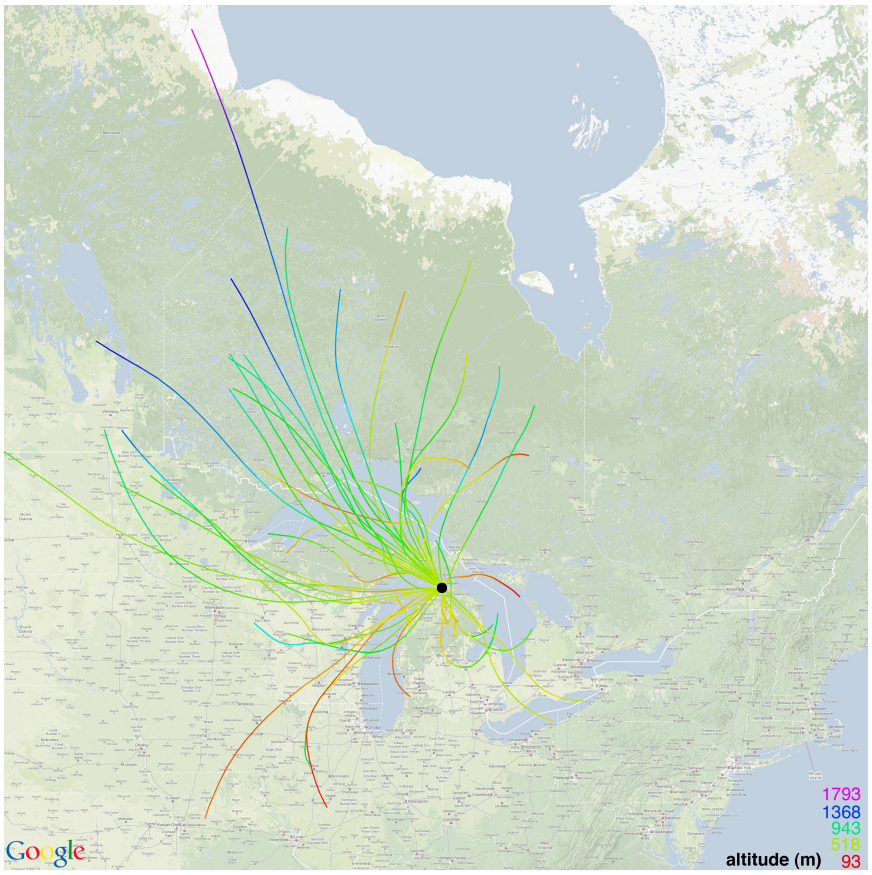

Figure 4.8: Daily 24-hour back-trajectories terminating at 500 m for the duration of the CABINEX field campaign, as calculated by the NOAA ARL/HYSPLIT model (Draxler and Hess, 1997, 1998). The majority of air masses sampled originated over rural Canada. While anthropogenic influence was occasionally observed it was limited to air masses originating from industrialized regions of the Great Lakes and Midwest.

packaged into a trailer. A meteorological tower sat atop this trailer at a height of 6 m and provided an additional sampling location that was in the understory. The WSU trailer was located within 20 m of the PROPHET tower.

The Great Lakes region lies at the intersection of the humid continental United States and the subarctic boreal climate of Canada. The region experiences frequent cloud cover resulting from the proximity to lakes Michigan, Huron and Superior. Temperatures during the field campaign were generally mild, with a mean (median) campaign temperature of 17.9 (18.0) °C on top of the tower. Occasionally temperatures would climb to the upper 20s, however, this never persisted for sustained periods longer than 2 – 3 days. A maximum and minimum temperature of 29.2 °C and 9.6 °C, respectively, were encountered. The release of isoprene from the UMBS forest is influenced both by the local temperature and cloud cover.

4.2.3 Additional Instruments & Data Products

The CABINEX field campaign was supported by a host of instrumentation coming from several universities and research centers. Both real-time measurements and samples for post-mission processing were collected. Brief descriptions of instruments related to the analysis of VOC oxidation and glyoxal formation follow.

4.2.3.1 OH/HO_x Measurements

OH and HO_2 measurements were made by a laser-induced fluorescence instrument from Indiana University (Dusanter et al., 2008). The instrument takes advantage of Fluorescence Assay by Gas Expansion technique (FAGE) with direct excitation of OH

at 308 nm. Indirect measurements of HO_2 are made possible by titration with NO to generate OH inside the fluorescence cell. A detection limit of 3.9×10^5 molecule cm^{-3} over 5-minutes is reported (Dusanter et al., 2007). Decreased sensitivity that results from power losses through long lengths of optical fiber are experienced when sampling from the top of the tower. Detection limits of less than 1.0×10^6 molecule cm^{-3} with 15 – 30 minute averaging are achieved under these scenarios.

The Indiana FAGE instrument is similar in concept to the HO_x instrument developed at Harvard (Wennberg et al., 1994), however the higher concentration of H_2O in the troposphere necessitates pumping the OH electronic transition at longer wavelengths to prevent significant contamination from laser-generated OH. Signal from artifact OH easily dominates ambient OH (Hanabusa et al., 1977; Davis et al., 1981) and is generated by chemistry resulting from O_3 photolysis:

$$O_3 + h\nu_{282\,\mathrm{nm}} \rightarrow O(^1D) + O_2 \tag{4.12}$$

$$O(^1D) + H_2O \rightarrow 2\ OH. \tag{4.13}$$

Operating at reduced pressures limits the availability of water vapor that can participate in reaction 4.13, however interferences from artifact OH can still be significant (Smith and Crosley, 1990). Using a laser light source at 308 nm to probe the OH (0,0) band reduces the interference by a factor of ~ 30 (a combination of lower O_3 absorption cross-section and lower $O(^1D)$ quantum yield) while increasing the OH absorption cross-section by a factor of ~ 6 (Heard and Pilling, 2003). However, this comes at the expense of spectral overlap between the pump and fluorescence

signal. Despite this, the increased fluorescence lifetime ($\sim$ 500 ns) that is achieved at low pressures in a FAGE instrument allows for temporal discrimination between fast scatter (e.g., Rayleigh, Mie and instrumental) processes coincident with the laser pulse and the slower fluorescence signal from OH.

4.2.3.2 Total OH Reactivity

In addition the OH/HO_2 measurements made by Indiana University, a total OH loss rate was made with the discharge-flow technique (Kaufman, 1984; Seeley et al., 1993; Donahue et al., 1996). OH is generated by photolysis of H_2O in saturated air by a 184.9 nm light source (mercury lamp). The generated OH is added to the core of a sample stream, made up of ambient air containing VOCs, by a movable injector. A fraction of the 308 nm laser light used in the OH/HO_2 instrument is sampled and fiber-coupled to the end of the detection cell where it is used to measure OH signal via fluorescence. Constant flow velocities and travel distance of approximately 1 m of the movable OH injector modulates the OH reaction time with species in the ambient air by an order of magnitude.

Under conditions where the concentration of the ambient species is in large excess relative to OH, the reaction can be taken to be pseudo first-order with respect to OH. The rate of loss of OH is proportional to concentration of OH in the case of first order kinetics. A plot of the concentration of OH against the reaction time will yield a straight-line with a slope equal to the pseudo-first order rate constant of the reaction between OH and air. The reaction time of OH with air is governed by the flow rate in the reaction chamber (held constant) and the position of the movable

injector. Since the fluorescence signal S is proportional to the concentration of OH at the detector and it is the relative change in concentration with reaction time that is measured, the absolute concentration of OH at the detector does not need to be determined.

The loss of OH with time is governed by the integrated first order rate equation (Kovacs and Brune, 2001):

$$\begin{aligned}\frac{\ln\left(S/S_0\right)}{t} = &- \left(k_{\mathrm{CO}}[\mathrm{CO}] + k_{\mathrm{CH_4}}[\mathrm{CH_4}] + k_{\mathrm{O_3}}[\mathrm{O_3}] + k_{\mathrm{NO_2}}[\mathrm{NO_2}]\right. \\ &\left. + k_{\mathrm{HCHO}}[\mathrm{HCHO}] + \sum_i k_{\mathrm{HC}_i}[\mathrm{HC}_i] + k_{\mathrm{X}}[\mathrm{X}]\right)\end{aligned} \tag{4.14}$$

where S_0 is the OH signal at the initial position of the injector; S is the OH signal after some reaction time t; k are the rate constants for the various OH reactions; HC_i refers to various hydrocarbons; and, X is representative of unknown or unaccounted for species that react with OH in air. The Indiana total OH reactivity instrument has a time resolution of 2 minutes and found that total OH reactivity has high temporal variability.

Total OH reactivity, which is the inverse of the OH lifetime, measurements are an important component of validating models of OH chemistry. Models which account for all "known" OH chemistry can be compared to the total OH loss rate to evaluate whether models accurately describe OH chemistry. In forest environments, it has been found that the total OH lifetime cannot be completely accounted for by the major chemical species. The difference between measured and modeled total OH reactivity, termed the missing OH reactivity, during the PROPHET 2000 intensive was

found to increase with heightened temperatures and suggested that other unknown reactive BVOCs may be involved in OH chemistry (Di Carlo et al., 2004).

4.2.3.3 VOC measurements

Measurements of a suite of VOCs and hydrocarbons were made by Washington State University using a proton-transfer reaction mass spectrometry (PTR-MS) instrument. The PTR-MS technique relies on the transfer of a proton from a donor XH^+ to a gas species R to generate a cation RH^+:

$$XH^+ (g) + R (g) \rightarrow RH^+ (g) + X (g). \tag{4.15}$$

The proton source is commonly H_3O^+. Selectivity is achieved due to differences between the proton affinity of different gas species. Proton affinities are the negative of the enthalpy change for reaction 4.15. Since the entropic contributions are small and show little variation between reactions, the proton affinity can be used to asses the spontaneity (in a Gibbs free energy sense) of a proton transfer (Smith and Španěl, 2005). Most of the bulk inorganic constituents of air (e.g., N_2, O_2, CO_2 and O_3) have lower proton affinities than H_2O, while trace organic constituents (e.g., alkenes, alkynes and aromatics) have higher proton affinities (Hunter and Lias, 1998). This results in PTR-MS being "transparent" to all but trace organic species (Blake et al., 2009). The cations formed from the proton transfer can then be sampled and detected by mass spectroscopy.

If the proton donor (H_3O^+) concentration is kept in large excess of the gas species (R) then the proton transfer reaction can be taken to be pseudo-first order with

respect to R and the concentration of R can be determined from the ratio of masses detected (Blake et al., 2009):

$$[\mathrm{R}] = \frac{[\mathrm{RH}^+]}{k_R t [\mathrm{H_3O}^+]} \tag{4.16}$$

where k_R is the known rate constant of the proton transfer reaction and t is the reaction time. With only mass spectroscopy providing compound discrimination, interferences resulting from fragmentation is a possibility. The VOC species measured by the WSU PTR-MS instrument are: formaldehyde; methanol; acetaldehyde; methyl hydroperoxide; acetone; isoprene; combined methacrolein and methylvinyl ketone; combined 2-butanone, butanal and methylglyoxal; benzene; toluene; the sum of C_2-alkylbenzenes; and the sum of monoterpenes. All species have a stated calibration accuracy of 10 % except formaldehyde which has a calibration accuracy of 20 % and methyl hydroperoxide which is assumed to have the same sensitivity as methanol.

4.3 Results

A large dataset of glyoxal measurements was made during the 2009 CABINEX field campaign. The final dataset provides both in-canopy and above-canopy measurements with a 1-minute resolution that covers over 47 % (statistically) of the campaign period between 30 June – 08 August 2009. Much of the unreported data comes from the beginning of the campaign and was the result of setup and initial calibrations.

Sampling alternated continuously between tower and alternate inlets (see Sec. 4.1.2.5 for a description of sampling setup) on a 30-minute timescale. While glyoxal data from the campaign is at times nearly continuous, data from a single inlet source is limited to a resolution of 30-minutes.

Glyoxal concentrations exhibited a diurnal profile that fluctuated around a mean concentration of approximately 25 ppt throughout the campaign. Several days during the campaign exhibited much larger concentrations of glyoxal, with a maximum observed concentration of 75 ppt. While variation in glyoxal concentration above-canopy and in-canopy are seen, these variations are smaller than the day-to-day variability in the average concentration.

4.3.1 Vertical Gradients

A comparison of glyoxal concentrations above-canopy (34 m) and in-canopy (6 m) as function of time of day for the entire campaign revealed the presence of vertical gradients. Measurements from each inlet are binned and averaged for each day of the campaign and the resulting daily bins are averaged to give an overall mission diurnal profile for each inlet—daily binning gives each day of the campaign equal weight to the overall profile. A maximum gradient (up to 4 ppt) exists between the top of the canopy and the understory throughout the evening.

Glyoxal is predominantly lost through photolysis—the lifetime of glyoxal for overhead sunlight conditions is roughly 90 minutes (Volkamer et al., 2005). Loss pathways at night are driven by oxidation, transport and deposition.

A simple explanation, with the assumption that precursors are well mixed and

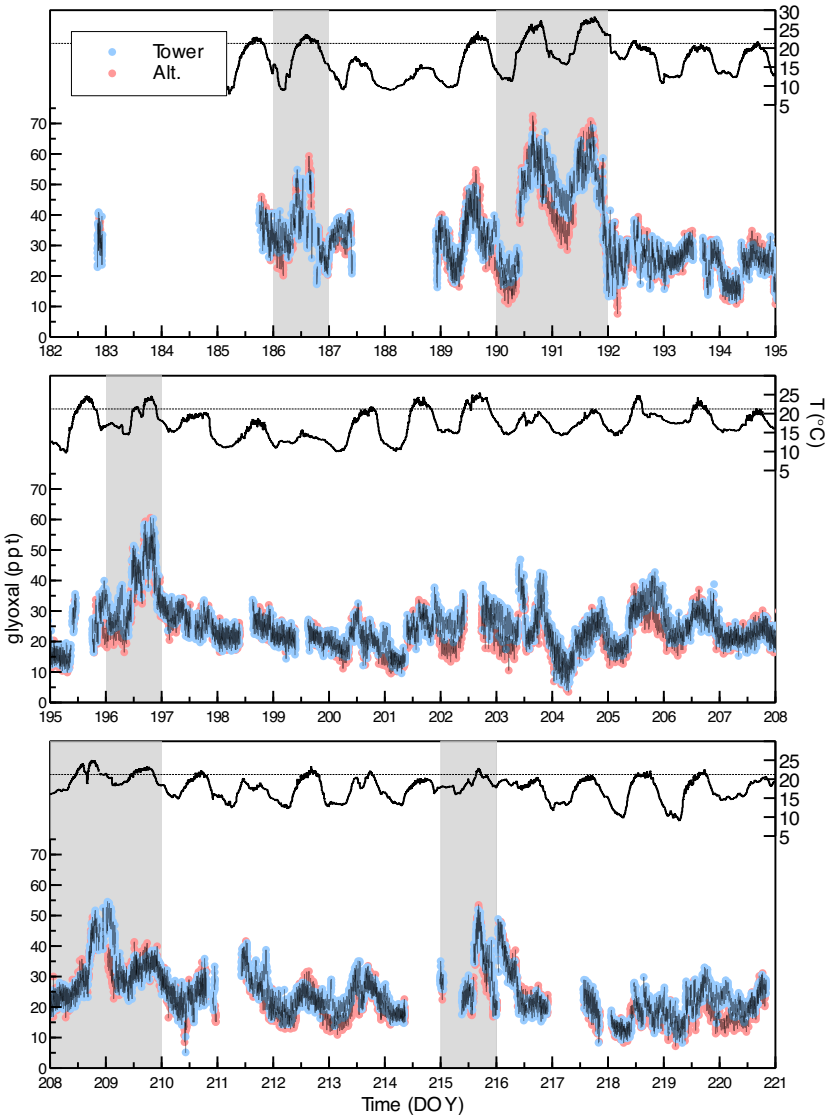

Figure 4.9: Glyoxal measurements for the duration of the CABINEX field campaign. Tower and (cyan dots) alternate (magenta dots) inlet data show are not equivalent, although there is less variation in the vertical gradient than the daily variability in glyoxal (black line). A regular diurnal cycle is seen as well as several days with large glyoxal production (> 50 ppt) denoted by gray shading. One-minute temperature data at a vertical height of 20 m is plotted with the dashed line indicating temperatures greater than 1-σ of the mission mean (17.3 ± 3.9 °C).

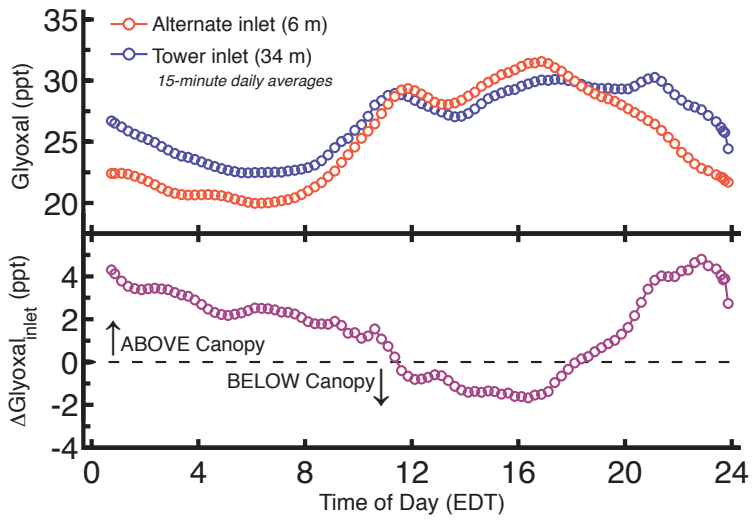

Figure 4.10: (upper panel) A mission average of 15-minute averaged daily data shows the presence of a diurnal cycle in both inlets. (lower panel) The difference between the two inlets reveals the presence of a vertical gradient as well as an inversion in the gradient.

the rate of production of glyoxal is identical in- and above-canopy, for the inversion in the vertical gradient is that there is a higher rate of loss of glyoxal above the canopy where it experiences a greater photolysis frequency. While this explanation for vertical gradients is consistent with radiative transfer in a forest canopy it suffers from the fact that the mid-day gradient inversion is not a typical diurnal feature but is instead driven by days where glyoxal is elevated.

The campaign-wide vertical gradient inversion can almost be completely accounted for by days where glyoxal concentrations exceeded 50 ppt. Only 8 days, representing roughly 20 % of the total data, exhibit such behavior. The daily maximum temperature on these 8 days exceed 1σ of the mean temperature for the campaign as measured by University of Michigan meteorological measurements made at

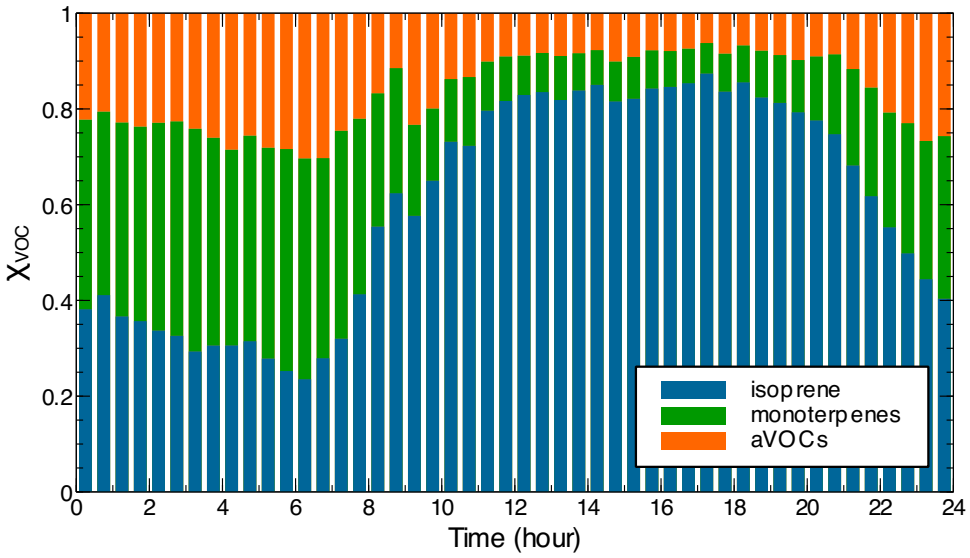

Figure 4.11: The fraction of each three different VOCs averaged across the entire campaign is shown. While the total VOC concentration is much greater when all VOCs measured by WSU PTRMS are included, isoprene, monoterpenes and aVOCs are identified as source VOCs. Other species are potentially sources as well as products of oxidation. Isoprene dominates the source fraction during mid-day while monoterpenes play an important role in the early morning hours.

20 meters on the PROPHET tower. While nearly half of the days of campaign exhibit maximum daytime temperatures greater than 1σ of the mean, the days where glyoxal exceeds 50 ppt are usually proceeded by a warm day.

4.3.2 VOC Sources

Three possible VOCs that contribute to oxidation chemistry and glyoxal formation can be identified from the WSU PTRMS measurements, which include: isoprene; monoterpenes; and anthropogenic VOCs (C2-alkylbenzenes, benzene and toluene). While many more VOCs are measured and contribute to a significant fraction of

observed VOCs they are not included because they are both glyoxal precursors and oxidation products of the three species identified. Decoupling the contribution that these species make as intermediates or as primary VOCs is not possible.

Isoprene is the dominant VOC source during mid-day sunlight periods. This is consistent with isoprene being a direct metabolic product of photosynthesis, where its production is sensitive to both light and heat. During early morning periods a sizable fraction of the VOC source term is contributed by monoterpenes.

4.3.3 Temperature Profiles of VOCs

A comparison of simultaneous in-canopy measurements of monoterpenes and isoprene by the WSU PTRMS instrument shows that there is little correlation between these two glyoxal precursors. Elevated concentrations of monoterpenes are often seen while isoprene concentrations are low. An overlay of in-canopy temperature (21 m) reveals a strong temperature dependence in isoprene while the monoterpenes are largely decoupled from temperature.

The early morning increase in monoterpenes (Fig. 4.11) is due to increases in temperature in the canopy. However the diurnal trend is also highly modulated by the local boundary layer height. The lack of correlation between monoterpenes and isoprene is explained by the processes controlling their release: monoterpenes are controlled exclusively by temperature yet isoprene is a direct product of photosynthesis, controlled by both temperature and light. The decreased fraction of monoterpenes making up the total VOC contribution later in the day is due to the large increase in isoprene that follows photosynthetic productivity.

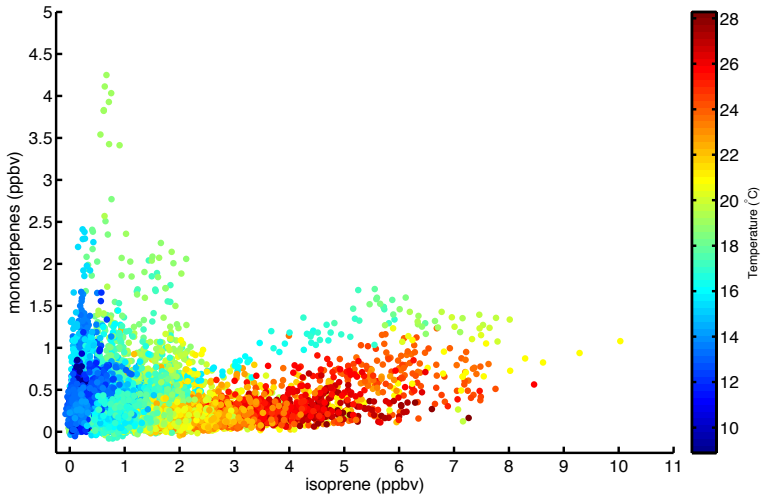

(a)

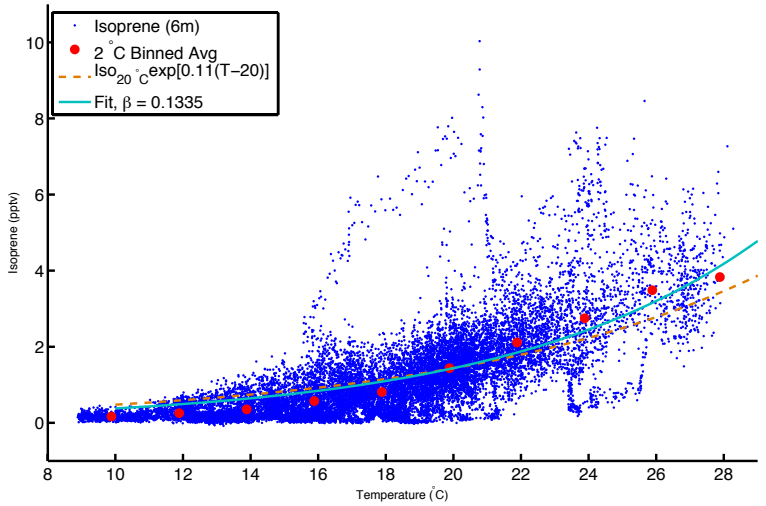

(b)

Figure 4.12: (a) Limited correlation exists between the concentration of monoterpenes and isoprene in the canopy. Monoterpenes do not show a strong temperature dependence while the concentration of isoprene is elevated during periods of high temperature. (b) Isoprene concentration as a function of temperature where curves are fit to the 2 °C bins (red circles). The orange curve uses parameters discussed in Di Carlo et al. (2004), while the cyan curve is fit to the data and gives $\beta = 0.1335$ K^{-1} with an $R^2 = 0.96$.

The daytime gradient inversion of glyoxal that occurs only during hot days and the strong temperature dependence of isoprene (see Fig. 4.12(b)) suggest that production of glyoxal via isoprene oxidation may be driving the gradient inversion. Presence of ground foliage is noted (e.g., ferns) however an in-canopy source is not identified as being responsible for observed increases in in-canopy isoprene.

4.4 Discussion

The glyoxal instrument described here was rapidly deployed to make measurements during the 2009 CABINEX field effort. A large dataset was collected with long periods of instrument uptime. Many of the efforts that went into the design of this instrument were replicated or slightly modified in the IO experiment.

Discussed are some of the direct measurements obtained by the glyoxal instrument as well as other instrument groups. A chemical model is required to extend analysis of glyoxal during this campaign. A model which accounts for production and loss pathways may be able to reveal the mechanisms responsible for the vertical gradient and the apparent temperature dependent factors that drive it.

Glyoxal can serve as a local tracer of VOC oxidation chemistry in rural environments; during BEARPEX glyoxal concentrations were found to be particularly sensitive to OH concentrations (Huisman et al., 2011). However, the forest composition at Blodgett Forest (BEARPEX 2007) is quite different and MBO was identified as the major glyoxal source while isoprene was a secondary source.

The large proportion of isoprene at the PROPHET site suggest that glyoxal can

serve as a direct tracer of isoprene oxidation. While isoprene makes up the bulk of the total OH reactivity discussed by Di Carlo et al. (2004) during the 2001 PROPHET measurements, the authors suggested that unmeasured terpenes may be substantial contributors to the VOC budget, particularly at elevated temperatures.

Kim et al. (2011) made branch enclosure measurements of OH reactivity during the campaign. The authors found that isoprene and monoterpenes could account for all the measured OH reactivity from red oak, white pine and beech at the site. Inclusion of a sesquiterpene, specifically α-farnesene, was required to reconcile the large discrepancy between modeled and observed OH reactivity in red maple branch enclosures. Kim et al. (2011) also found that typically unmeasured first generation isoprene oxidation products (e.g., glyoxal, C4- and C5-hydroxycarbonyl compounds, and glycolaldehyde) could account for ~ 8.0 % of the isoprene contribution to total OH reactivity and that branching ratios of these typically unmeasured products relative to the sum of methacrolein and methyl vinyl ketone are highly modulated by NO. Later generation oxidation products, which can also include glyoxal, can contribute significantly, to the point that they surpass isoprene's contribution, to the total OH reactivity (Kim et al., 2011).

The binned temperature profile isoprene (Fig. 4.12(b)) is fit with the parameters described by Di Carlo et al. (2004) that "represent" monoterpene emission rates. The parameters closely fit the temperature profile of isoprene. A relaxed fit, yields a similar exponential parameter ($\beta = 0.1335$) to that for monoterpenes ($\beta = 0.11$), with good correlation to the data ($R^2 = 0.96$). Taken together with the results of Kim et al. (2011) this suggests that isoprene and its later stage oxidation products

may be exclusively responsible for the measured OH reactivity in the PROPHET forest. Measurements of secondary oxidation products, like glyoxal, and mechanisms of isoprene oxidation need to be incorporated into models of OH reactivity to accurately represent VOC distributions.

References

D. Z. Anderson. Alignment of resonant optical cavities. *Applied Optics*, 23:2944–2949, Sept. 1984. doi: 10.1364/AO.23.002944.

L. Anderson. Collision induced intersystem crossing the photophysics of glyoxal vapor excited at 4358 Å. *Chemical Physics*, 1:401–417, Aug. 1973. doi: 10.1016/0301-0104(73)87001-6.

L. G. Anderson, C. S. Parmenter, H. M. Poland, and J. D. Rau. Intersystem crossing in glyoxal vapor. An experimental study of both the resonant and statistical limit. *Chemical Physics Letters*, 8:232–234, Jan. 1971. doi: 10.1016/0009-2614(71)80023-4.

B. V. Barnes. Cover types of UMBS, April 2011.

S. Bertman. personal communication, 2009.

R. A. Beyer and W. C. Lineberger. Relaxation in the ^1A_u state of glyoxal. II. Collisional quenching. *Journal of Chemical Physics*, 62:4024–4031, May 1975. doi: 10.1063/1.430326.

R. S. Blake, P. S. Monks, and A. M. Ellis. Proton-Transfer Reaction Mass Spectrometry. *Chemical Reviews*, 109(3):861–896, 2009. doi: 10.1021/cr800364q.

J. G. Canadell, C. Le Quere, M. R. Raupach, C. B. Field, E. T. Buitenhuis, P. Ciais, T. J. Conway, N. P. Gillett, R. A. Houghton, and G. Marland. From the Cover: Contributions to accelerating atmospheric CO2 growth from economic activity, carbon intensity, and efficiency of natural sinks. *Proceedings of the National Academy of Science*, 104:18866–18870, Nov. 2007. doi: 10.1073/pnas.0702737104.

M. A. Carroll, S. B. Bertman, and P. B. Shepson. Overview of the Program for Research on Oxidants: PHotochemistry, Emissions, and Transport (PROPHET) summer 1998 measurements intensive. *J. Geophys. Res.*, 106(D20):24275–24288, 2001. doi: 10.1029/2001JD900189.

C. Cossart-Magos. Fluorescence and phosphorescence spectra of glyoxal-h_2 and -d_2 from single vibronic levels of ^1A_u and ^3A_u states. *Spectrochimica Acta Part A: Molecular Spectroscopy*, 34:195–204, 1978. doi: 10.1016/0584-8539(78)80116-0.

D. D. Davis, M. O. Rodgers, S. D. Fischer, and K. Asai. An experimental assessment of the O_3/H_2O interference problem in the detection of natural levels of OH via laser induced fluorescence. *Geophysical Research Letters*, 8(1):69–72, 1981. doi: 10.1029/GL008i001p00069.

P. Di Carlo, W. H. Brune, M. Martinez, H. Harder, R. Lesher, X. Ren, T. Thornberry, M. A. Carroll, V. Young, P. B. Shepson, D. Riemer, E. Apel, and C. Campbell. Missing OH Reactivity in a Forest: Evidence for Unknown Reactive Biogenic VOCs. *Science*, 304:722–725, Apr. 2004. doi: 10.1126/science.1094392.

N. M. Donahue, J. S. Clarke, K. L. Demerjian, and J. G. Anderson. Free-Radical Kinetics at High Pressure: A Mathematical Analysis of the Flow Reactor. *The Journal of Physical Chemistry*, 100(14):5821–5838, 1996. doi: 10.1021/jp9525503.

R. R. Draxler and G. D. Hess. Description of the HYSPLIT_4 modeling system. NOAA Tech. Memo. ERL ARL-224, NOAA Air Resources Laboratory, Silver Spring, MD, 1997.

R. R. Draxler and G. D. Hess. An overview of the HYSPLIT_4 modeling system of trajectories, dispersion, and deposition. *Aust. Meteor. Mag.*, 47:295–308, 1998.

G. B. Dreyfus, G. W. Schade, and A. H. Goldstein. Observational constraints on the contribution of isoprene oxidation to ozone production on the western slope of the Sierra Nevada, California. *Journal of Geophysical Research*, 107(D19), 2002. doi: 10.1029/2001JD001490.

S. Dusanter, D. Vimal, P. S. Stevens, R. Volkamer, and L. T. Molina. Hydroxyl and Hydroperoxy Radical Chemistry during the MCMA-2006 Field Campaign: Measurement and Model Comparison. *AGU Fall Meeting Abstracts*, page C6, Dec. 2007.

S. Dusanter, D. Vimal, P. S. Stevens, R. Volkamer, and L. T. Molina. Measurements of OH and HO_2 concentrations during the MCMA-2006 field campaign Part 1: Deployment of the Indiana University laser-induced fluorescence instrument. *Atmospheric Chemistry & Physics Discussions*, 81:13689–13739, July 2008.

T.-M. Fu, D. J. Jacob, F. Wittrock, J. P. Burrows, M. Vrekoussis, and D. K. Henze. Global budgets of atmospheric glyoxal and methylglyoxal, and implications for formation of secondary organic aerosols. *Journal of Geophysical Research*, 113: D15303, Aug. 2008. doi: 10.1029/2007JD009505.

M. M. Galloway, A. J. Huisman, L. D. Yee, A. W. H. Chan, C. L. Loza, J. H. Seinfeld, and F. N. Keutsch. Yields of oxidized volatile organic compounds during the OH radical initiated oxidation of isoprene, methyl vinyl ketone, and methacrolein under high-NO_x conditions. *Atmospheric Chemistry and Physics*, 11(21):10779–10790, 2011. doi: 10.5194/acp-11-10779-2011.

A. H. Goldstein and I. E. Galbally. Known and unexplored organic constituents in the earth's atmosphere. *Environmental Science & Technology*, 41(5):1514–1521, 2007. doi: 10.1021/es072476p.

A. Guenther, C. N. Hewitt, D. Erickson, R. Fall, C. Geron, T. Graedel, P. Harley, L. Klinger, M. Lerdau, W. A. McKay, T. Pierce, B. Scholes, R. Steinbrecher, R. Tallamraju, J. Taylor, A. Guenther, C. N. Hewitt, D. Erickson, R. Fall, C. Geron, T. Graedel, P. Harley, L. Klinger, M. Lerdau, W. A. McKay, T. Pierce, B. Scholes, R. Steinbrecher, R. Tallamraju, J. Taylor, and P. Zimmerman. A global model of natural volatile organic compound emissions. *Journal of Geophysical Research*, 100:8873–8892, 1995. doi: 10.1029/94JD02950.

M. Hanabusa, C. Wang, S. Japar, D. Killinger, and W. Fisher. Pulsewidth dependence of ozone interference in the laser fluorescence measurement of OH in the atmosphere. *Journal of Chemical Physics*, 66(5), 1977.

D. E. Heard and M. J. Pilling. Measurement of OH and HO_2 in the Troposphere. *Chemical Reviews*, 103(12):5163–5198, 2003. doi: 10.1021/cr020522s.

J. Higbie. Uncertainty in the linear regression slope. *American Journal of Physics*, 59(2):184–185, 1991. doi: 10.1119/1.16607.

A. J. Huisman, J. R. Hottle, K. L. Coens, J. P. DiGangi, M. M. Galloway, A. Kammrath, and F. N. Keutsch. Laser-induced phosphorescence for the in situ detection of glyoxal at part per trillion mixing ratios. *Analytical Chemistry*, 80(15):5884–5891, 2008. doi: 10.1021/ac800407b. PMID: 18593190.

A. J. Huisman, J. R. Hottle, M. M. Galloway, J. P. DiGangi, K. L. Coens, W. Choi, I. C. Faloona, J. B. Gilman, W. C. Kuster, J. de Gouw, N. C. Bouvier-Brown, A. H. Goldstein, B. W. LaFranchi, R. C. Cohen, G. M. Wolfe, J. A. Thornton, K. S. Docherty, D. K. Farmer, M. J. Cubison, J. L. Jimenez, J. Mao, W. H. Brune, and F. N. Keutsch. Photochemical modeling of glyoxal at a rural site: observations and analysis from BEARPEX 2007. *Atmospheric Chemistry & Physics*, 11(17): 8883–8897, 2011. doi: 10.5194/acp-11-8883-2011.

E. P. L. Hunter and S. G. Lias. Evaluated Gas Phase Basicities and Proton Affinities of Molecules: An Update. *Journal of Physical and Chemical Reference Data*, 27 (3):413–656, 1998. doi: 10.1063/1.556018.

V. Isidorov, I. Zenkevich, and B. Ioffe. Volatile organic compounds in the atmosphere of forests. *Atmospheric Environment*, 19(1):1–8, 1985. doi: 10.1016/0004-6981(85) 90131-3.

F. Kaufman. Kinetics of elementary radical reactions in the gas phase. *The Journal of Physical Chemistry*, 88(21):4909–4917, 1984. doi: 10.1021/j150665a024.

F. N. Keutsch. personal communication. Determination of effective pathlength of CRDS axis by NO_2 calibration, 2010.

S. Kim, A. Guenther, T. Karl, and J. Greenberg. Contributions of primary and secondary biogenic VOC tototal OH reactivity during the CABINEX (Community Atmosphere-Biosphere INteractions Experiments)-09 field campaign. *Atmospheric Chemistry & Physics*, 11(16):8613–8623, 2011. doi: 10.5194/acp-11-8613-2011.

H. Kogelnik and T. Li. Laser beams and resonators. *Applied Optics*, 5:1550, Oct. 1966. doi: 10.1364/AO.5.001550.

T. A. Kovacs and W. H. Brune. Total OH Loss Rate Measurement. *Journal of Atmospheric Chemistry*, 39:105–122, 2001. 10.1023/A:1010614113786.

J. H. Kroll, N. L. Ng, S. M. Murphy, V. Varutbangkul, R. C. Flagan, and J. H. Seinfeld. Chamber studies of secondary organic aerosol growth by reactive uptake of simple carbonyl compounds. *Journal of Geophysical Research*, 110:D23207, Dec. 2005. doi: 10.1029/2005JD006004.

E. Pebay Peyroula and R. Jost. $S_1 \leftarrow S_0$ laser excitation spectra of glyoxal in a supersonic jet: Vibrational analysis. *Journal of Molecular Spectroscopy*, 121:177–188, Jan. 1987. doi: 10.1016/0022-2852(87)90180-9.

K. K. Perkins, T. F. Hanisco, R. C. Cohen, L. C. Koch, R. M. Stimpfle, P. B. Voss, G. P. Bonne, E. J. Lanzendorf, J. G. Anderson, P. O. Wennberg, R. S. Gao, L. A. Del Negro, R. J. Salawitch, C. T. McElroy, E. J. Hintsa, M. Loewenstein, and T. P. Bui. The NO_x-HNO_3 system in the lower stratosphere: Insights from in situ measurements and implications of the J(HNO_3)-[OH] relationship. *Journal of Physical Chemistry A*, 105(9):1521–1534, MAR 8 2001.

R. A. Rasmussen and F. W. Went. Volatile Organic Material of Plant Origin in the Atmosphere. *Proceedings of the National Academy of Science*, 53:215–220, Jan. 1965. doi: 10.1073/pnas.53.1.215.

J. V. Seeley, J. T. Jayne, and M. J. Molina. High pressure fast-flow technique for gas phase kinetics studies. *International Journal of Chemical Kinetics*, 25(7):571–594, 1993. doi: 10.1002/kin.550250706.

H. B. Singh and P. Zimmerman. Atmospheric distributions and sources of non-methane hydrocarbons. In J. O. Nriagu, editor, *Advances in Environmental Science and Technology*, volume 24, pages 177–235. Wiley, New York, 1990.

D. Smith and P. Španěl. Selected ion flow tube mass spectrometry (SIFT-MS) for on-line trace gas analysis. *Mass Spectrometry Reviews*, 24(5):661–700, 2005. doi: 10.1002/mas.20033.

G. P. Smith and D. R. Crosley. A photochemical model of ozone interference effects in laser detection of tropospheric OH. *Journal of Geophysical Research*, 95:16427–16442, Sept. 1990. doi: 10.1029/JD095iD10p16427.

J. N. Smith, K. F. Moore, P. H. McMurry, and F. L. Eisele. Atmospheric Measurements of Sub-20 nm Diameter Particle Chemical Composition by Thermal Desorption Chemical Ionization Mass Spectrometry. *Aerosol Science and Technology*, 38(2):100–110, 2004. doi: 10.1080/02786820490249036.

S. Solomon. *Climate Change 2007: the physical science basis. Contribution of Working Group I to the Fourth Assessment Report of the Intergovernmental Panel on Climate Change*. Cambridge University Press, Cambridge, United Kingdom and New York, NY, USA, 2007.

D. E. Vogler and M. W. Sigrist. Near-infrared laser based cavity ringdown spectroscopy for applications in petrochemical industry. *Applied Physics B: Lasers and Optics*, 85:349–354, 2006. doi: 10.1007/s00340-006-2313-z.

R. Volkamer, P. Spietz, J. Burrows, and U. Platt. High-resolution absorption cross-section of glyoxal in the UV-vis and IR spectral ranges. *Journal of Photochemistry and Photobiology A: Chemistry*, 172(1):35–46, 2005.

P. O. Wennberg, R. C. Cohen, N. L. Hazen, L. B. Lapson, N. T. Allen, T. F. Hanisco, J. F. Oliver, N. W. Lanham, J. N. Demusz, and J. G. Anderson. Aircraft-borne, laser-induced fluorescence instrument for the in situ detection of hydroxyl and

hydroperoxyl radicals. *Review of Scientific Instruments*, 65:1858–1876, June 1994. doi: 10.1063/1.1144835.

F. W. Went. Organic Matter in the Atmosphere, and its Possible Relation to Petroleum Formation. *Proceedings of the National Academy of Science*, 46:212–221, Feb. 1960. doi: 10.1073/pnas.46.2.212.

J. U. White. Long optical paths of large aperture. *Journal of the Optical Society of America (1917-1983)*, 32:285, May 1942.

J. T. Yardley. Collisional Quenching and Photochemistry of *trans*-Glyoxal (^3A_u) Molecules. *Journal of Chemical Physics*, 56:6192–6197, June 1972. doi: 10.1063/1.1677171.

P. Zalicki and R. N. Zare. Cavity ring-down spectroscopy for quantitative absorption measurements. *Journal of Chemical Physics*, 102:2708–2717, Feb. 1995. doi: 10.1063/1.468647.

Chapter 5

IO LIF Instrument & Results

> If you are looking for perfect safety, you will do well to sit on a fence and watch the birds; but if you really wish to learn, you must mount a machine and become acquainted with its tricks by actual trial.
>
> Wilbur Wright

5.1 IO Instrument Overview

The IO laser-induced fluorescence (LIF) instrument in its current configuration is an outgrowth of previous work by Co (2007) who investigated the feasibility of the LIF and CRDS techniques to the in situ measurement of iodine monoxide. What follows is a description of the instrument as developed for deployment and extended operation at remote coastal locations.

5.1.1 Measurement Technique

The $A^2\Pi_{3/2}$–$X^2\Pi_{3/2}$ spectrum was first observed by Vaidya (1937) while investigating methyl iodide-methanol flames. Durie and Ramsay (1958) were the first to measure the absorption spectrum of IO, the (0,0) and (2,0) bands showed sharp rotational features whereas other levels were reported to be heavily predissociated. The (2,0) band is strongest in the LIF spectrum (Newman et al., 1998). The LIF spectrum of the (3,0) has been demonstrated to show extensive rotational structure, however it is considerably weaker in LIF than the (2,0) band (Turnipseed et al., 1995).

IO is detected by initiating the $A^2\Pi_{3/2}(v' = 2) \leftarrow X^2\Pi_{3/2}(v'' = 0)$ transition with 445 nm photons. Predissociation of the $A^2\Pi_{3/2}$ competes directly with radiative decay.

$$\mathrm{IO}(\mathrm{X}^2\Pi_{3/2})(v''=0) + h\nu_{445\ \mathrm{nm}} \rightarrow \mathrm{IO}(\mathrm{A}^2\Pi_{3/2})(v'=2) \quad (5.1)$$

$$\mathrm{IO}(\mathrm{A}^2\Pi_{3/2})(v'=2) \rightarrow \mathrm{IO}(\mathrm{X}^2\Pi_{3/2})(v''=5,\,6) + h\nu \quad (5.2)$$

$$\mathrm{IO}(\mathrm{X}^2\Pi_{3/2})(v'=2) \rightarrow \mathrm{I}(^2\mathrm{P}_{3/2}) + \mathrm{O}(^3\mathrm{P}) \quad (5.3)$$

The $\mathrm{A}^2\Pi_{3/2}$ correlates diabatically with products $\mathrm{I}(^2\mathrm{P}_{3/2})$ and $\mathrm{O}(^1\mathrm{D})$ (Newman et al., 1998), however several repulsive states cross the $\mathrm{A}^2\Pi_{3/2}$ yielding the observed products as shown in Rxn. 5.3.

The (2,0) band exhibits J'-dependent linewidth broadening indicating rotation-induced predissociation. While the (0,0) and (3,0) bands do not show evidence of J'-dependent linewidths, the lineshapes in the (2,0) band are the narrowest observed (Newman et al., 1998). This implies the that predissociation of $v'=2$ is weaker than for any other vibrational level of the $\mathrm{A}^2\Pi_{3/2}$ state.

The natural lifetime (τ) of a molecule in the excited state (in the absence of collisional quenching) is given by:

$$\frac{1}{\tau} = \frac{1}{\tau_{\mathrm{rad}}} + \frac{1}{\tau_{\mathrm{pre}}} \quad (5.4)$$

where τ_{rad} is the radiative lifetime and τ_{pre} is the predissociative lifetime. A 1 – 10 ns radiative lifetime is estimated for the $\mathrm{A}^2\Pi_{3/2}$ state of IO (Bekooy et al., 1983). However, the more rapid predissociation limits the natural lifetime of the excited state to less than 1 ns for low rotational states and it decreases linearly with increasing J' (Newman et al., 1998). Since the lifetime of IO in the excited state is shorter than

the length of the laser pulse ($\sim$ 40 ns), temporal discrimination of the excitation pulse and fluorescence signal by electronic gating methods is not possible.

The strong absorption of the (2,0) band coupled with limited predissociation in this state, resulting in appreciable fluorescence quantum yield, make this transition most suitable for IO detection.

5.1.2 Hardware Overview

At the heart of the IO instrument is pulsed titanium sapphire (Ti:Al_2O_3, or Ti:sapph) laser capable of generating 445 nm radiation. The laser system is the same used to generate the 440 nm light required for laser-induced phosphorescence of glyoxal. The laser system is briefly discussed here as it was specifically designed with the spectroscopy of IO in mind.

Light at 445 nm is generated by pumping a titanium-doped sapphire crystal with a 532 nm frequency-doubled neodymium-doped yttrium aluminum garnet (Nd:YAG) laser. Titanium sapphire has a very large gain bandwidth (650–1100 nm) centered at 800 nm. A diffraction-grating in the laser cavity is used to generate a narrow linewidth source at 890 nm which is then frequency doubled by an extra-cavity cesium lithium borate crystal generating the requisite 445 nm. Wavelength tuning is made possible by rotating the angle of the diffraction grating on a rotation stage.

Previously, a continuously movable rotation stage driven by a stepper motor was used to tune the laser wavelength; however, significant hysteresis was observed in the rotation stage making it difficult to reliably scan over spectral peaks. Replacement with a piezo-driven tangent arm rotation stage (Physik Instrumente, M-036.PS) pro-

vides increased repeatability.

5.1.2.1 LIF Axis

The maximum fluorescence signal intensity for IO is obtained for the $v'' = 1 \leftarrow v' = 2$ transition at 460 nm. There also exists a relatively strong fluorescence signal near 520 nm, corresponding to the $5 \leftarrow 2$ transition. Aggressive filtering with longpass (Semrock LP02-514RE-25) and bandpass (Semrock FF01-530/23-25) filters allow for the fluorescence signal of the strong $5 \leftarrow 2$ transition, and a weaker $6 \leftarrow 2$ transition, to be detected by the PMT while suppressing coincident photons from the excitation pulse. The longpass filter has an edge at 514.5 nm and a very narrow transition region of 97 cm^{-1}. The bandpass filter is centered at 530 nm and has a bandwidth of 27.8 nm with an optical depth, outside the bandpass region, greater than 6 between 400 – 750 nm.

Rotation of the PMT from a vertical position to a horizontal position in the packaged assembly required the addition of a zero-order half-wave plate (Thorlabs, WPH05M-488) to rotate the plane of linear polarization to reduce Rayleigh scatter in the White cell.

5.1.2.2 CRD Axis

An inline cavity ringdown axis that is 15 cm downstream of the LIF axis is used for calibration. The same high reflective mirrors (CRD Optics, 901-0010-0440) used in the glyoxal instrument (Sec. 4.1.2.2) are used for IO. Although the mirrors have reflectivity centered at 440 nm, they have a 50 nm bandwidth where the reflectivity

is greater than 99.99 %.

Mirrors are mounted in stainless steel mounts (CRD Optics, 902-0010) that attach to 2.75 inch Conflat vacuum flanges. Three equilaterally-spaced fine-threaded turn-screws (80 turns per inch) around the perimeter of the mirror are used to adjust the angle of the mirror. Considerable slippage has been experienced with these mounts, necessitating a more robust redesign of the mirror mounts.

A minimum detectable absorption (see Eq. 4.5) of 2.5×10^{-7} for IO in the CRD axis corresponds to 2.5×10^{19} molecules cm^{-3}, or 100 pptv near the surface. An increase in the minimum detectable absorption by an order of magnitude (i.e., $[\Delta\tau/\tau]_{min} = 0.5 \times 10^{-4}$) is likely possible with higher sensitivity (low-noise) detector electronics. Indeed, Wada et al. (2007) demonstrated an open-path cavity ringdown spectrometer to measure IO in the marine boundary layer with a 10 pptv minimum limit of detection during a 30 s data acquisition time under ideal conditions.

5.1.2.3 Data Acquisition

Data acquisition is controlled by custom software primarily written with LabVIEW (National Instruments). Signals are generated and acquired with associated data acquisition cards (National Instruments, PCI-6229 & USB-6221; see Sec. 4.1.2.3 for more details).

Each PCI-6229 DAQ card has 2 counter channels, giving a total of four available counters, which are used for photon counting. An 80 MHz clock is generated on a primary counter which is used to generate a 125 ns gate on a secondary channel. The remaining two channels are used to count pulses from the LIF axis and reference

cell photomultiplier tubes. Additional DAQ hardware (USB-6221) was added to the instrument to make more counters available in order to generate a second 150 μs gate used to count background solar scatter in the LIF axis.

5.1.2.4 Calibration

The fundamental equation which dictates the retrieved fluorescence signal S_{IO} to the absolute concentration of IO is given by

$$S_{\mathrm{IO}} = [\mathrm{IO}] \times E \times \Phi \times C \tag{5.5}$$

where E is the excitation rate, Φ is the fluorescence efficiency and C is the collection efficiency. While the excitation rate is proportional to the effective IO absorption cross section and the IO population density in the probed rotational state, it is only the laser power which fluctuates appreciably during calibrations which are carried out at constant pressure and temperature. The collection efficiency is the product of the collection optics' area solid angle cross product and transmission efficiency, and the quantum efficiency of the PMT. The fluorescence efficiency is the fraction of IO molecules excited into the $\mathrm{A}^2\Pi_{3/2}$ state that undergo a radiative transition back to the ground state.

For IO the fluorescence efficiency is the dimensionless quantity that relates the rate of the radiative decay of the excited state to the sum of all decay processes

$$\Phi = \frac{k_{\mathrm{rad}}}{k_{\mathrm{rad}} + k_{\mathrm{pre}} + k_{\mathrm{q}}[Q]}. \tag{5.6}$$

Decay from the excited state can occur through both radiative and non-radiative (predissociation and collisional quenching) processes. The lifetime in the absence of quenching

$$\tau = \frac{1}{k_{\text{rad}} + k_{\text{pre}}} = \frac{1}{2\pi c\Gamma} \tag{5.7}$$

can be determined from the experimentally determined rotational linewidths Γ of the (2,0) band (Gravestock et al., 2010)

$$\Gamma = 0.004 + \kappa J'(J' + 1), \tag{5.8}$$

where $\kappa = 113 \times 10^{-6}$. The quenching rate coefficient for the (2,0) state has been determined by Gravestock et al. (2010) to be, at 296 K, equivalent to $k_q = (12.8 \pm 0.8) \times 10^{-11}$ cm^3 molecule^{-1} s^{-1}. At low sampling pressure (20 Torr) a small decrease ($\sim$ 50 ps) to the excited state lifetime is attributed to collisional quenching. At high sampling pressures (150 Torr) a 30 % decrease in the excited state lifetime is due to the increase in the rate of collisional deactivation. Changes in the quantum efficiency of fluorescence due to pressure fluctuations during calibrations can be neglected as the pressure in the White cell is kept constant at 20 Torr.

A plot of the power normalized fluorescence signal against the concentration of IO in the LIF axis yields a slope that is equivalent to the instrument sensitivity constant β

$$\frac{S}{P_{\text{laser}}} = \beta[\text{IO}] + S_0 \tag{5.9}$$

where S_0 is the background signal due instrumental scattering processes. The instrumental sensitivity constant β encapsulates the various terms in Equation 5.5

which do not need to be known explicitly as they are experimentally determined. Correction terms are required if the temperature or pressure in the LIF axis differ from conditions during calibration. Changes in temperature will affect the rotation population distribution of the ground state while changes in pressure manifest as changes to the rotational lineshape and quantum efficiency of fluorescence.

Calibration of the fluorescence signal requires that the concentration of IO at the fluorescence axis be accurately known. Two available methods are available to quantitatively determine the concentration of IO as the detection axis: correlated LIF/CRD spectroscopy and chemical titration.

5.1.2.4.1 Correlated LIF/CRD Spectroscopy Method Previous work by Co (2007) revealed that chemical titration and correlated CRD-LIF spectroscopy could be used to quantify and calibrate the concentration of IO in the sampling duct. While CRDS is not a viable option for measuring IO in the field, as it has a detection threshold that is greater than ambient tropospheric mixing ratios of IO, it can be used at elevated IO concentrations to directly measure the IO mixing ratio. This can be used in conjunction with LIF detection at decreased laser powers to calibrate the sensitivity of the optical system to fluorescence.

At high IO concentrations the laser power has to be reduced in order to prevent saturation of the photomultiplier tube. When the rate of fluorescence exceeds the temporal resolution of the PMT, multiple photon events that occur during a single gate cannot be distinguished and the PMT output is no longer linear. Reducing the average laser power in the White cell, through the use of beam splitters and neutral density filters, reduces the rate of fluorescence so that the PMT output remains

linear. The decrease in fluorescence signal is due to the fact that the excitation rate (Eq. 5.5) is linearly proportional to the average laser power in the White cell. However, as calibrations are made in terms of a power normalized signal, changes in the fluorescence signal due to changes in the laser power are inherently accounted for, hence the instrument sensitivity constant β is insensitive to the laser power at which the calibration is carried out.

The concentration of IO can be determined directly from an absorption measurement using CRDS (see Sec. 4.1.2.4). Measurement of the IO concentration at various distance from the injector allows for the determination of the wall loss rate for a given flow condition. Mixing ratios of IO in the ppbv range are generated by photolyzing trifluoroiodomethane (CF_3I) and reacting the resulting iodine with ozone.

$$CF_3I + h\nu_{254\text{ nm}} \rightarrow CF_3 + I \tag{5.10}$$

$$I + O_3 \rightarrow IO + O_2 \tag{5.11}$$

IO concentrations can vary between the CRD and LIF axis as a result of either irreversible uptake onto the walls of the duct or through the IO self reaction

$$IO + IO \rightarrow \text{products.} \tag{5.12}$$

With a large excess of O_3 the formation of IO occurs rapidly in the sampling duct. Only at high concentrations of IO ($\sim$ 100 ppb) does the loss due to the self reaction become non-negligible between the CRD axis and the LIF axis. There is approximately a 20 % loss in IO between the two axes under such conditions. A kinetic model

is used to introduce a correction term to account for loss due to the self reaction.

While the correlated LIF/CRD spectroscopy has been successfully demonstrated as means to calibrate the instrument in the laboratory it proved inadequate during field trials. Rapid loss in mirror reflectivity resulted in low sensitivities in the CRD axis. Removing and cleaning the mirrors was able to reestablish mirror reflectivity, although still below specification ($\tau \approx 7$ μs). However, within a few minutes and prior to the addition of reagents to generate IO the cavity time constant would fall to levels that were not able to be fit accurately ($\tau < 1$ μs). Salt migration onto the mirror surfaces at decreased pressure is speculated as the reason for degradation in the performance of the mirrors, although there is no conclusive evidence to support this hypothesis.

The mirror reflectivity appears to have permanently degraded as the mirrors have aged. The mirrors have a reflectivity, $R = 99.985$ %, with a per pass loss three times above specification. Although a new pair of mirrors was purchased recently, these are from the same batch and are the same age as the original mirrors purchased for the CRD experiment in 2006. Aggressive cleaning of the mirrors was not able to restore the mirrors to the manufacturer's specified reflectivity. The combination of permanent mirror degradation and rapid loss of reflectivity in a field (marine) environment led to the decision to abandon correlated LIF/CRD as a calibration technique in favor of chemical titration. With new mirrors having adequate reflectivity ($R \geq 99.995$ %) CRD remains an ideal laboratory calibration method and serves as an independent method for intercomparison with chemical titration methods.

5.1.2.4.2 Chemical Titration The concentration of IO in the LIF axis can be quantitatively determined from the reaction between CF3I and O(^{3}P) since the branching ratio of the reaction has been experimentally determined. At 100 Torr and 298 K the IO yield is reported as $\Phi(\mathrm{IO}) = 0.83 \pm 0.09$ (Gilles et al., 1996). At 2 – 4 Torr and 298 K the yield is reported as $\Phi(\mathrm{IO}) = 0.93 \pm 0.04$ (Bloss et al., 2001). It has been suggested that the IO yield may be pressure dependent if the reaction proceeds via a collisionally stabilized intermediate.

$$\mathrm{CF_3I} + \mathrm{O}(^3\mathrm{P}) \rightarrow \mathrm{CF_3IO^*} \tag{5.13}$$

$$\mathrm{CF_3IO^*} + \mathrm{M} \rightarrow \mathrm{CF_3IO} \tag{5.14a}$$

$$\mathrm{CF_3IO^*} \rightarrow \mathrm{CF_3} + \mathrm{IO} \tag{5.14b}$$

An investigation into the pressure dependence of the IO yield between 100 – 760 Torr at 298 K found that there was no significant changes in the yield; however, at low temperatures (220 K) a 20 % decrease in the IO yield was witnessed as pressure was increased over the range (Bloss et al., 2001).

The reaction of excess O(^{3}P) with CF_3I as a limiting reagent is seemingly the most straightforward calibration route. The concentration of CF_3I is known, a $\sim$ 10 ppb tank (Scott-Marrin) is typically used, and excess O(^{3}P) ensures that the CF_3I is completely consumed. Calibrations are carried out at 298 K and 20 Torr so that, coupled with the findings of Gilles et al. (1996), the initial IO concentration is simply $0.83 \times [\mathrm{CF_3I}]$. However, the excess O(^{3}P) initiates the rapid loss of IO. The relevant

iodine reaction that occur in the duct are shown below.

$$CF_3I + O(^3P) \rightarrow CF_3 + IO \quad (5.15)$$

$$IO + O(^3P) \rightarrow O_2 + I \quad (5.16)$$

$$IO + IO \rightarrow \text{products} \quad (5.17)$$

$$I + O_3 \rightarrow IO + O_2 \quad (5.18)$$

A full chemical model incorporating the above reactions is required to determine the temporal profile of IO in the duct. Any appreciable excess of $O(^3P)$ will result in Reaction 5.16 dominating the IO loss pathways. The concentration of $O(^3P)$ must be known in order to successfully calibrate with this method, limiting some of the benefits afforded by this method.

An alternative calibration method is chemical titration of $O(^3P)$ with excess CF_3I. With this method the rapid loss of IO with excess reagent is not possible and the IO self reaction (Rxn. 5.17) is the only available loss pathway. A large excess of CF_3I ensures that the formation of IO is fast relative to its loss. An accurate measurement of $O(^3P)$ is required to determine the initial yield of IO. Excess CF_3I has been found to contaminate the fluorescence axis so that it interferes with the CF_3I titration method. Subjecting the instrument to heat, high UV flux and atomic oxygen will slowly ($\sim 1-2$ weeks) decrease contamination. Contamination of the duct and White cell with precursor does not interfere with ambient sampling as high UV fluxes and atomic oxygen concentrations are required to generate IO.

5.1.2.5 Sampling Method

Air is sampled by drawing it through a small diameter pinhole formed in stainless steel cap with a 1 hp oil-free dry scroll vacuum pump (Varian, TriScroll 600) that pulls 5 standard liters minute^{-1}, generating a flow velocity of $\sim$ 1 m s^{-1} in the detection axis. The loss of IO through a pinhole is characterized by measuring the absolute concentration on either side of the inlet with CRDS. A loss of 20 % is experienced for sampling conditions that produce 20 Torr in the duct (Co, 2007).

While a decrease in the number density of IO is expected to result from gas expansion through the inlet, this is compensated for by other increases in sensitivity. Small signal gains are achieved by the narrowing of rotational lines and the increased fluorescence efficiency at decreased pressure. A large increase in sensitivity is gained by the reduction of solar scatter that a small pinhole affords. The inlet is directed toward the zenith in order to make sampling insensitive to horizontal wind direction but this comes at the expense of increased background counts.

5.2 IO Field Deployment

The IO LIF instrument was deployed into the field on two occasions, that served primarily as instrument validation missions. Field sites were chosen based on a variety of criteria and posed different sets of challenges but both were demonstrated sites where IO had been previously measured.

5.2.1 Mace Head, Ireland

During August – September 2010 the IO instrument was deployed to a remote coastal atmospheric research station on Ireland's west coast, near the town of Carna, Co. Galway. The research station is operated by the National University Ireland and also serves as site of the Advanced Global Atmospheric Gases Experiment (AGAGE) network. Measurements of aerosols, background anthropogenic gases (CFCs and HCFCs), and fluxes of carbon dioxide and ozone are made on site. Standard weather products are available as the site is also home to instruments that are part of the Irish Meteorological Service.

There is a long history of measurements of IO at the site made using a long-path differential optical absorption spectrometer (LP-DOAS) (Seitz et al., 2010; Saiz-Lopez et al., 2006; Alicke et al., 1999). Point measurements of IO were made with an LIF instrument, similar in concept to the Harvard design, during August 2007 (Commane et al., 2011). The concentration of IO measured at the site varies widely between the two methods. LP-DOAS measurements report peak concentrations less than 10 ppt while the LIF point measurements by Commane et al. (2011) report peak concentrations of nearly 50 ppt. This discrepancy can be attributed to the spatial inhomogeneity of IO along the coast and the strong influence of the intertidal region on iodine production.

Mace Head Research Station (53° 19′ 34″ N, 9° 54′ 14″ W) is located on a headland that protrudes into the Irish Sea. The site experiences semi-diurnal tides and tide heights can vary by as much 4.7 m during spring tides. A gentle slope in the coastline results in large horizontal tidal range ($\sim$ 50 m), exposing large populations

of kelp during spring low tides. Extensive beds of *Laminaria digitata*, a subtidal kelp species, only become exposed when the tide height falls below 0.3 m. Large increases in IO at the site are thought to be due the atmospheric exposure of *L. digitata*, where molecular iodine is directly released as a result of iodide oxidation during the scavenging of reactive oxygen species (Küpper et al., 2008). Peak IO concentrations are expected during mid-day low tides when the photolysis frequency of molecular iodine is greatest.

Figure 5.1: *Laminaria digitata* which is named for the its long segments that resemble fingers. This sample was harvested from a site in coastal Maine in Acadia National Park. This species of kelp is known to uptake iodine, which gives it its color, and is a sub-tidal species, exposed only during spring low tides.

5.2.2 Appledore Island, Maine

A deployment to the Shoals Marine Laboratory (SML) on Appledore Island, Maine was carried out during August – September 2011. SML is a seasonal marine laboratory operated collaboratively by Cornell University and University of New Hampshire with the mission of providing undergraduate education in the marine sciences. While not a traditional research station, the site can provide infrastructure and support to research groups. The site is located approximately 6 nautical miles southeast from the nearest port in Portsmouth, NH within the Isles of Shoals archipelago.

Measurements of IO were previously made between Appledore Island and White Island, covering a total path length of 4.6 km at a height of 35 – 15 m above the surface of the open ocean with a long-path DOAS instrument (see Fig. 5.2). IO was only observed during the daytime with a maximum concentration of 4 pptv (Stutz et al., 2007). Additionally, year-round measurements are made on Appledore Island by UNH/NOAA as part of the Atmospheric Investigation, Regional Modeling, Analysis and Prediction (AIRMAP) network. Standard meteorological data products are available as well as measurements of ozone, carbon dioxide, carbon monoxide and cloud base height.

The site is isolated from the mainland and generates its own power with a combination of wind and solar sources and, primarily, with diesel engine-generator sets. This presented a logistical challenge as the peak power loads of the instrument exceeded the baseline available power at the site. Significant overhead power must be available to the instrument during the startup of various motors used in the vacuum

and coolant subsystems. A single phase, liquid-cooled diesel generator (Kubota, GL11000) capable of producing a maximum of 11 kW at 240 VAC was acquired to meet the power demands of the instrument on the island.

The southwestern Gulf of Maine are populated by a variety of kelp species. Throughout the 1970s the area was dominated by canopy forming kelps, *Laminaria* spp., and red algae (Martin et al., 1988; Witman, 1987). A change in the composition of the region began in the 1980s with shallow-water communities becoming dominated by sea urchins (*Strongylocentrotus droebachiensis*) (Witman, 1985) and subsequent commercial harvesting leading to large scale decline in the 1990s (Harris and Tyrrell, 2001). Opportunistic and introduced species have flourished and the inland shores are populated by much smaller kelp communities mixed in with new species including *Codium fragile* (green alga), *Membranipora membranacea* (bryozoan), *Diplosoma listerianum* (tunicate), *Bonnemaisonia hamifera* (red alga), *Mytilus edulis* (mussel) and *Desmarestia aculeata* (brown alga) (Harris and Tyrrell, 2001). A visual survey of the tidal ledges surrounding Appledore Island did not reveal the presence any exposed beds of *L. digitata* during spring low tides. While no near shore kelp beds were observed, large quantities of *Laminaria* spp. were washed on shore, particularly in Broad Cove, following Hurricane Irene on 28 – 29 August 2011. However, only a small fraction of the *Laminaria* washed on ashore was identified as *L. digitata*.

Many of the thermal and optical issues that were encountered during the Mace Head deployment, and discussed below, were confronted before the deployment to the Shoals Marine Laboratory on Appledore Island.

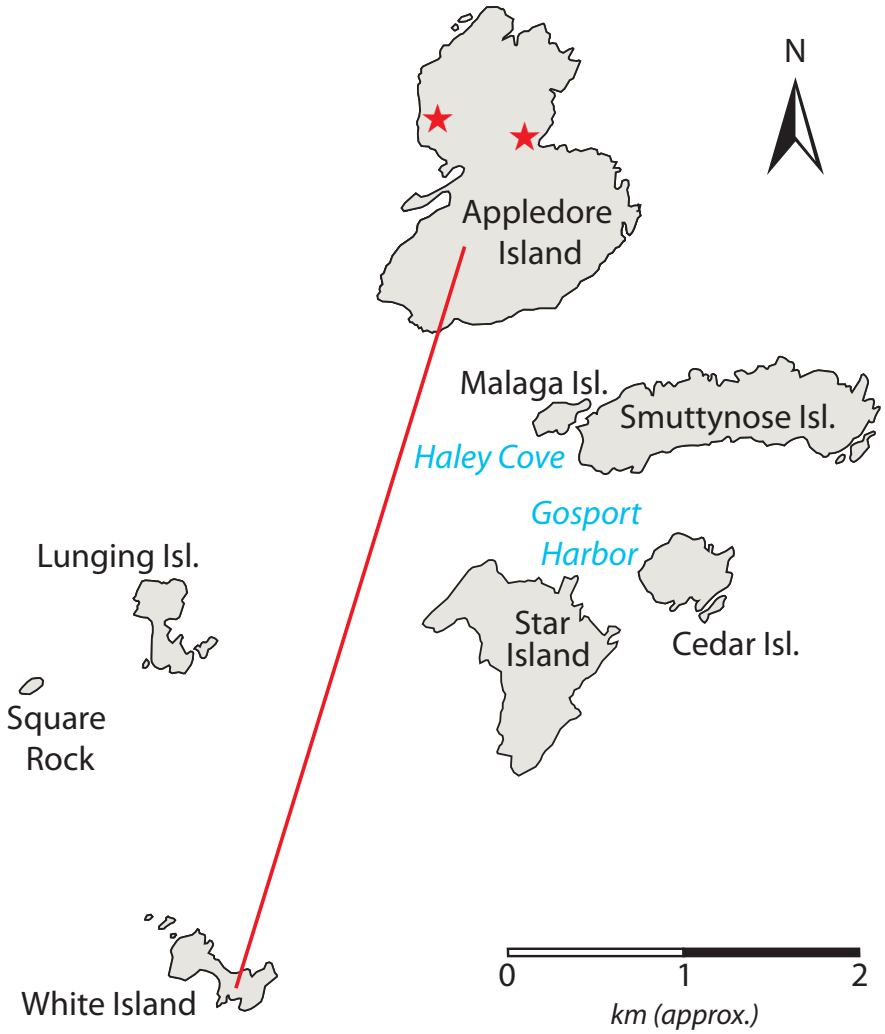

Figure 5.2: A partial map of the Isles of Shoals archipelago in the southwestern Gulf of Maine, located 6 nautical miles from the nearest mainland port. The approximate LP-DOAS sampling path, between Appledore and White Islands, is shown by the solid red line. Approximate sampling locations made by the IO LIF instrument are shown by the red stars: near the Grass Foundation Laboratory on the west side of the island and near Broad Cove on the east side of the island. Kelp populations near Appledore Island are reported to be found primarily on the exposed (east) side. *Map data adapted from the OpenStreetMap project, under CC-BY-SA license.*

5.3 Results

5.3.1 Measurement Challenges & Constraints

The primary challenge of making a point measurement of IO at a coastal site is to package equipment designed for laboratory use into an instrument that is both mobile and capable of withstanding large fluctuations in weather conditions.

The IO instrument as deployed in 2010 and 2011 was developed around two waterproof cases (Pelican, 0550) each providing over 300 L of interior volume. Each case was mounted to a custom aluminum chassis with heavy-duty, low-pressure polyurethane tires (Wheeleez, WZ1-49U) designed for transport over sand and soft terrain. An optical table, mounted via wire rope isolators, and electronics rack were fit into a "sensor box," while an "auxiliary box" contained a vacuum pump (Varian, TriScoll 600), UPS battery backup (APC, SUA2200I), thermoelectric chiller (Solid State Cooling, ThermoCube 400), water pump, and an electrical distribution panel. The cases were modified to allow addition of various bulkhead and thru-fittings used for fluid, electrical and data connections.

5.3.1.1 Thermal & Spectral Stability

A major hurdle to successful and repeatable operation is thermal stability inside the cases, particularly in the sensor box. Laser power, at frequency-doubled wavelengths (445 nm), is sensitive to the baseplate temperature of the laser. At colder temperatures there is an increase in the output power.

At Mace Head high temperatures inside the auxiliary box decreased the effec-

tiveness of the liquid-circulating thermoelectric cooler which was used to control the baseplate temperature of the Ti:sapphire laser. The overall temperature of the sensor box was controlled by fans and a flowing-liquid radiator. Liquid in the sensor box cooling loop was cooled to approximately 1 °C above ambient temperatures by passing the coolant (fresh water) through large external fan-cooled radiators. The temperature of the auxiliary box was unregulated but kept at roughly 5 °C above ambient by continuously circulating air through the sensor box with washdown fans mounted directly to the box.

A 400 W cooling capacity is specified for the thermoelectric chiller, used to maintain the temperature of the Ti:sapph baseplate, when there is a 0 °C differential between the process temperature and ambient temperature; as the temperature differential increases the cooling capacity is quickly diminished. During operation in the field, the laser baseplate temperature tracked closely with ambient temperatures resulting in large fluctuations in power. Instrument operation usually suffered at mid-day and into the early afternoon when temperatures were highest and during periods where IO was expected to be greatest.

A second issue that became apparent was that piezo/rotation stage position, and therefore wavelength, is very sensitive to the laser baseplate temperature. This wavelength dependence on temperature is related to changes in the laser cavity, however, no single component could be identified as being solely responsible. The position of peaks with respect to control voltages in the piezo driver change as the temperature of the baseplate changes, making repeated scans over a single rotational line difficult to achieve with consistency. A larger scanning interval ensures that the

peak is scanned but this comes at the cost of time resolution and signal-to-noise during acquisition.

Laboratory tests indicated that the relative shift in peak position decreased at lower temperatures. In order for a shift in the position of a rotational peak to be less than the full-width at half maximum (FWHM) the temperature of the baseplate had to be maintained at 16.5 ± 0.1 °C. To maintain the baseplate temperature to this degree of control extensive modifications were made to the cooling strategy of the laser.

The laser has an an internal cooling loop integrated into the nickel-plated aluminum baseplate which the optical components are mounted to. The internal loop is designed primarily to remove heat generated in the Nd:YAG head, although there is a small secondary cooling loop that runs in parallel to cool the Ti:sapphire crystal housing. A buildup of aluminum oxide deposits frequently led to blockages of flow in the secondary loop. Previously, a second baseplate with a serial serpentine coolant had been added to the laser increase the effectiveness of the coolant loop.

The factory-designed coolant loop was removed from active operation. The coolant loop was filled with coolant, to ensure maximum heat transfer, and sealed with NPT plugs. The secondary loop was removed and replaced by an aluminum plate to which was mounted six 15 W thermoelectric cooling elements providing a total of 90 W of cooling capacity. The maximum estimated heat that must be dissipated from the baseplate is 20 W. The thermoelectric elements were aligned in two rows of three elements allowing for a pair of liquid-cooled heat exchangers to be mounted to the hot-side of the thermoelectric elements. A large refrigerated re-

circulating chiller (Neslab) was used as a roughing chiller bringing the baseplate to roughly 16 °C. An in-house heater controller was used to control the thermoelectric elements and provide temperature stability in the baseplate to within ±0.1 °C of the setpoint. The combined thermoelectric/recirculating chiller system was able to bring the baseplate to 16.5 °C from ambient box temperatures (∼ 30 °C) in approximately 15 minutes and provided exceptional stability of the baseplate temperature. Many of the issues of wavelength stability that had previously been experienced were alleviated by this cooling strategy and the scanning software rarely had trouble identifying and tracking the position of the IO rotational peak.

5.3.1.2 Laser Power Instability

During the Mace Head deployment a large modulation in the laser power was apparent as the laser was scanned over the IO spectrum. The modulation in laser power was approximately 50 % of the total laser power and exhibited multiple cycles through the IO spectrum. The large oscillation in baseline power made it difficult to power normalize the fluorescence counts.

The large modulation in the power of the 445 nm laser light was thought to be attributed to the limited number of longitudinal modes that were excited in the laser cavity. The laser linewidth (FWHM) at 890 nm is 590 MHz, determined by a diffraction grating with 2000 lines mm^{-1}, while the longitudinal mode spacing in the cavity is approximately 200 MHz. Bad alignment of the Ti:sapphire cavity results in only a limited number of these longitudinal modes reaching the lasing threshold. As the laser is scanned mismatch in overlap between the longitudinal modes and the laser

lineshape results in an oscillation of output power. Realignment of the laser cavity increased the total output power and minimized power fluctuations. The increase in power in the cavity made more longitudinal modes available that were above the lasing threshold and minimized mismatch leading to the large power oscillations.

5.3.1.3 Reference Cell

Determining peak positions and the wavelength of the laser from the reference cell was hampered by the oscillation in laser power. When the reference cell signal was strongest, within a few hours of filling the reference cell, the fluorescence counts dominated the baseline signal and the baseline signature had minimal impact on the peak detection algorithm. As the fluorescence signal degraded, due to leaks and loss of IO precursor, PMT counts that could be attributed to baseline power modulations were comparable to counts from IO fluorescence. Under these conditions the peak scanning algorithm struggled to find and maintain the IO peak.

Reference stability was greatly improved by the addition of two solenoid valves used at the fill and evacuation ports of the cell. The addition of these automated valves had two-fold benefit to operation of the instrument in the field. Firstly, the solenoid valves allowed for the refilling of the reference cell without requiring the opening of the box. This resulted in an increase in instrument uptime and minimized the chance of contamination of the optical system in the harsh field environment. Secondly, the solenoid valves greatly decreased the leak rate into the reference cell. Whereas during the Mace Head deployment the reference cell had to be filled daily, during the Appledore campaign the reference cell leaked at a rate of less than 1 Torr

day^{-1}. This slow leak rate coupled with tuning of the reference cell filament to limit loss of the precursor meant that the reference could be filled on weekly or longer periods.

5.3.2 IO Generated From Kelp

Prior to the Appledore deployment, a laboratory test was conducted to test the instrument sensitivity to IO generated from kelp samples. *Laminaria digitata* was harvested from a coastal location at Schoodic Point in the Acadia National Park, Maine and transported back to the laboratory. Keeping the kelp samples in a container with sea water placed on ice maintained their viability despite $\sim$ 12 hours of elapsed time between harvesting and sampling.

Several pieces of *Laminaria digitata* were added to a polypropylene bin, a total volume of kelp of approximately 5 L, which was loosely covered by another bin. A 1 m length of corrugated PTFE tubing was attached to the pin-hole cap on the detection duct and the other end placed inside the bin containing the kelp. The bin was illuminated by fluorescent lights only. No IO signal was observed when laboratory air was drawn across the kelp into the instrument.

A small flow of ozone (100 sccm) generated by passing oxygen across a mercury lamp was added to the bin containing the kelp and a significant signal of IO was observed by the instrument. As time progressed the intensity of the IO signal would decay. However, agitating and moving the position of the O_3 flow would regenerate a signal. It is speculated that the decay was a result of a local depletion of iodine at the site of O_3 addition.

It is very difficult to quantify the amount of iodine released by the *Laminaria digitata* sample under these conditions. However, the test served as qualitative indicator as to whether a small quantity of North American *Laminaria digitata* would produce sufficient IO to be detected by the instrument. Given the strong fluorescence signal from the small sample volume it was expected that IO detection at a coastal site would be feasible even if beds were not as extensive as at Mace Head, Ireland so long as the instrument could be situated near enough to the beds.

5.4 Discussion

The modifications made to the IO instrument discussed and implemented prior to the deployment to Appledore Island significantly improved the reliability and stability of the instrument. Decrease in the magnitude of the laser power oscillation made the instrument more stable and increased the sensitivity of the instrument. The increased repeatedly of scans across rotational peaks that came with stabilizing the baseplate temperature made continuous collection possible. Additionally, new thermal management techniques made operation across diurnal temperature variations possible.

One of the tasks that remain for the instrument is to improve the signal-to-noise ratio. During the mission a clear anodized section of duct upstream of the White cell was replaced with a treated section of duct. This treated section of duct work was finished with a cupric oxide layer upon which was deposited a thin painted light-trapping coating. Background PMT counts were reduced by a factor of 3, from more

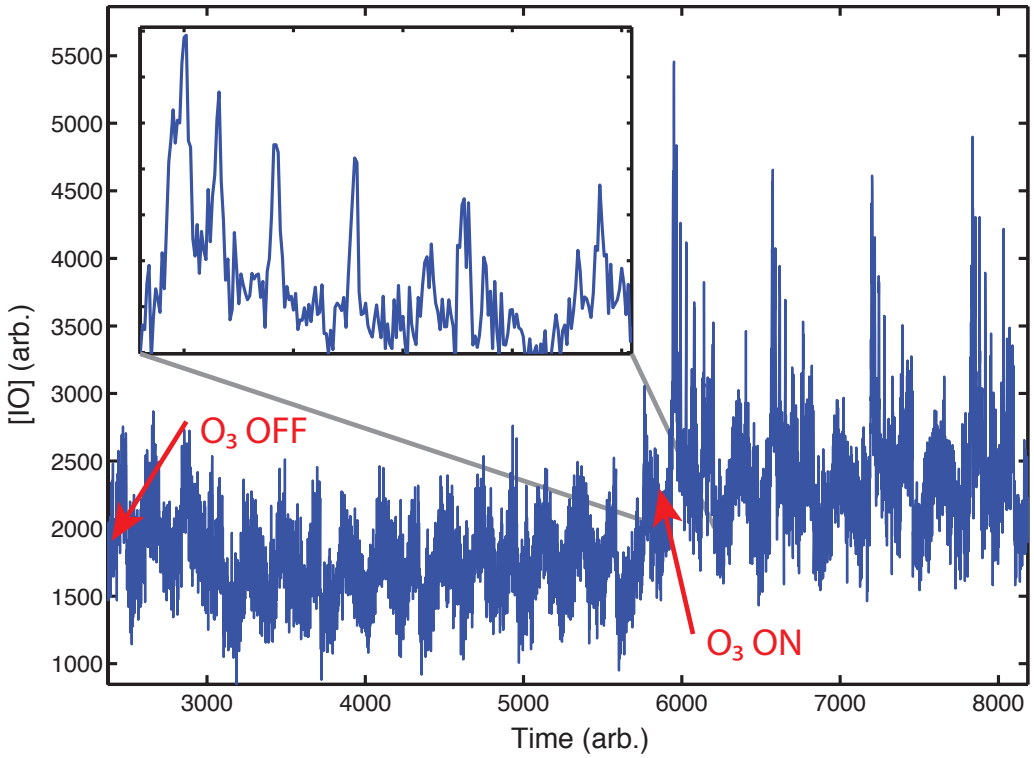

Figure 5.3: A large IO signal was observed when a small flow of O_3 directed across a sample of *L. digitata* in the laboratory. The sample was illuminated by fluorescence lights in the laboratory (see text for additional details). No signal was seen unless O_3 was added. The IO is seen to slowly decay, but could be regenerated by agitating the sample. Low signal to noise was the result of poor alignment during the experiment which generated significant laser scatter in the LIF detection axis. A closeup shows the characteristic fluorescence spectrum of IO; the large peak is the (2,0) bandhead.

than 1000 s^{-1} to roughly 300 s^{-1} by changing the duct. Further increases in sensitivity can be made by changing the software algorithm that drives the position of the rotation stage in the Ti:sapphire cavity and determines the wavelength. The increase in stability of laser wavelength and the addition of a feedback sensing circuit to the piezo actuator will likely make it possible to implement an online/offline dithering technique rather than continuous scans over the rovibronic transition. While this has yet to be implemented in the instrument software, it would potentially lead to an increase in both the signal-to-noise and acquisition speed.

Preliminary data from the deployment to the Isles of Shoals indicate that IO was detected during several intermittent periods. These periods coincide with an IO mixing ratio on the order of several pptv. DOAS measurements made by Stutz et al. (2007) at the site revealed similar IO mixing ratios as in clean marine environments like Mace Head. A maximum mixing ratio of 4 pptv was observed by this technique during the Chemistry of Halogens at the Isles of Shoals (CHAiOS) campaign, but the usual mixing ratio was regularly below 2 pptv.

Stutz et al. (2007) made simultaneous measurements of NO_2 and OIO and found that OIO was more homogeneously distributed spatially than IO, which they attributed to a longer chemical lifetime of OIO that results from rapid chemical cycling processes. OIO mixing ratios exceeded that of IO and there was little observed dependence of the IO/OIO ratio to NO_x. Furthermore, there was a lack of a tidal signature in the IO mixing ratios, which is well pronounced at Mace Head (Saiz-Lopez and Plane, 2004; Commane et al., 2011), and no explanation for this behavior is given. The Gulf of Maine and, particularly, the Isles of Shoals, in contrast to Mace

Head, is a polluted marine environment with high NO_x concentrations that result from its proximity to the heavily populated cities of New England.

Large differences between point source and integrated long-path techniques (i.e., LP-DOAS) are known (Commane et al., 2011), indicating spatial heterogeneity of IO production from tidal kelp beds. This may explain some of the sporadic episodes of IO observed. As measurements made during campaign on the Isles of Shoals were not situated near kelp beds, as in the case of Mace Head, IO must be transported to the sampling site. It is not clear where the primary sources of iodine are located in the Isles of Shoals and the point-source measurements would be influenced very differently by the local topography than LP-DOAS measurements (see Fig. 5.2).

While results from the deployment to the Isles of Shoals are preliminary, it remains difficult to interpret them in the absence of additional species. This becomes especially true when considering that the understanding of iodine chemistry in the marine boundary layer is still incomplete. The deployment did validate the technique and instrument under field conditions and indicated the feasibility of future field studies.

References

B. Alicke, K. Hebestreit, J. Stutz, and U. Platt. Iodine oxide in the marine boundary layer. *Nature*, 397:572–573, Feb. 1999. doi: 10.1038/17508.

J. P. Bekooy, W. L. Meerts, and A. Dymanus. High-resolution laser-rf spectroscopy on the $A^2\Pi_{3/2}$-$X^2\Pi_{3/2}$ system of iodine oxide (IO). *Journal of Molecular Spectroscopy*, 102(2):320–343, 1983. doi: 10.1016/0022-2852(83)90044-9.

W. J. Bloss, D. M. Rowley, R. A. Cox, and R. L. Jones. Kinetics and Products of the IO Self-Reaction. *The Journal of Physical Chemistry A*, 105(33):7840–7854, 2001. doi: 10.1021/jp0044936.

D. T. P. Co. Development of a laser-induced fluorescence instrument for the in situ atmospheric measurements of iodine monoxide, 2007.

R. Commane, K. Seitz, C. S. E. Bale, W. J. Bloss, J. Buxmann, T. Ingham, U. Platt, D. Pöhler, and D. E. Heard. Iodine monoxide at a clean marine coastal site: observations of high frequency variations and inhomogeneous distributions. *Atmospheric Chemistry & Physics*, 11:6721–6733, July 2011. doi: 10.5194/acp-11-6721-2011.

R. A. Durie and D. A. Ramsay. Absorption spectra of the halogen monoxides. *Canadian Journal of Physics*, 36:35, 1958.

M. K. Gilles, A. A. Turnipseed, R. K. Talukdar, Y. Rudich, P. W. Villalta, L. G. Huey, J. B. Burkholder, and A. R. Ravishankara. Reactions of $O(^3P)$ with Alkyl Iodides: Rate Coefficients and Reaction Products. *The Journal of Physical Chemistry*, 100(33):14005–14015, 1996. doi: 10.1021/jp960688v.

T. J. Gravestock, M. A. Blitz, and D. E. Heard. A laser induced fluorescence study relating to physical properties of the iodine monoxide radical. *Physical Chemistry Chemical Physics*, 12:823–834, 2010. doi: 10.1039/B910571A.

L. Harris and M. Tyrrell. Changing Community States in the Gulf of Maine: Synergism Between Invaders, Overfishing and Climate Change. *Biological Invasions*, 3: 9–21, 2001. 10.1023/A:1011487219735.

F. C. Küpper, L. J. Carpenter, G. B. McFiggans, C. J. Palmer, T. J. Waite, E.-M. Boneberg, S. Woitsch, M. Weiller, R. Abela, D. Grolimund, P. Potin, A. Butler, G. W. Luther, P. M. H. Kroneck, W. Meyer-Klaucke, and M. C. Feiters. Iodide accumulation provides kelp with an inorganic antioxidant impacting atmospheric

chemistry. *Proceedings of the National Academy of Sciences*, 105(19):6954–6958, 05 2008.

P. D. Martin, S. P. Truchon, and L. G. Harris. *Strongylocentrotus droebachiensis* populations and community dynamics at two depth-related zones over an 11-year period. In R. Burke, editor, *Proceedings of the 6th International Echinoderm Conference*, pages 475—482, Victoria, BC, August 23–28 1988. AA Balkema, Rotterdam, The Netherlands.

S. M. Newman, W. H. Howie, I. C. Lane, M. R. Upson, and A. J. Orr-Ewing. Predissociation of the $A^2\Pi_{3/2}$ state of IO studied by cavity ring-down spectroscopy. *Journal of the Chemical Society, Faraday Transactions*, 94:2681–2688, 1998. doi: 10.1039/A805103H.

A. Saiz-Lopez and J. M. C. Plane. Novel iodine chemistry in the marine boundary layer. *Geophysical Research Letters*, 31(4), 02 2004. doi: 10.1029/2003GL019215.

A. Saiz-Lopez, J. A. Shillito, H. Coe, and J. M. C. Plane. Measurements and modelling of I_2, IO, OIO, BrO and NO_3 in the mid-latitude marine boundary layer. *Atmospheric Chemistry and Physics*, 6(6):1513–1528, 2006. doi: 10.5194/acp-6-1513-2006.

K. Seitz, J. Buxmann, D. Pöhler, T. Sommer, J. Tschritter, T. Neary, C. O'Dowd, and U. Platt. The spatial distribution of the reactive iodine species io from simultaneous active and passive doas observations. *Atmospheric Chemistry and Physics*, 10(5):2117–2128, 2010. doi: 10.5194/acp-10-2117-2010.

J. Stutz, O. Pikelnaya, S. C. Hurlock, S. Trick, S. Pechtl, and R. von Glasow. Daytime OIO in the Gulf of Maine. *Geophys. Res. Lett*, 342:L22816, Nov. 2007. doi: 10.1029/2007GL031332.

A. A. Turnipseed, M. K. Gilles, J. B. Burkholder, and A. R. Ravishankara. LIF detection of IO and the rate coefficients for I + O_3 and IO + NO reactions. *Chemical Physics Letters*, 242:427–434, Aug. 1995. doi: 10.1016/0009-2614(95)00774-X.

W. Vaidya. The flame spectra of some aliphatic halides—Part I. *Proceedings Mathematical Sciences*, 6:122–128, 1937. 10.1007/BF03051247.

R. Wada, J. Beames, and A. Orr-Ewing. Measurement of IO radical concentrations in the marine boundary layer using a cavity ring-down spectrometer. *Journal of Atmospheric Chemistry*, 58:69–87, 2007. doi: 10.1007/s10874-007-9080-z.

J. D. Witman. Refuges, Biological Disturbance, and Rocky Subtidal Community Structure in New England. *Ecological Monographs*, 55(4):421–445, 12 1985.

J. D. Witman. Subtidal Coexistence: Storms, Grazing, Mutualism, and the Zonation of Kelps and Mussels. *Ecological Monographs*, 57(2):167–187, 06 1987.

Chapter 6

Conclusions

> Finally, it was stated at the outset, that this system would not be here, and at once, perfected. You cannot but plainly see that I have kept my word. . . This whole book is but a draught—nay, the draught of a draught. Oh, Time, Strength, Cash, and Patience.
>
> *Moby Dick; or, The Whale*
> Herman Melville

Much of the work presented here is motivated by the need to develop techniques and instrumentation to measure trace atmospheric species *in situ*. The free radicals, VOCs and tracers discussed can have mixing ratios less than one part in a billion, and often times orders of magnitude less, but still they play significant roles in key cycles that determine the composition and radiative properties of the atmosphere. Despite the importance and global impact these species have, the results presented here represent only a snapshot of an evolving global system. Continued measurements are required to answer new questions and to resolve existing ones that beg answers.

While the instruments and measurement are presented as largely individual topics, their interplay is a central feature of science that enters the realm of public policy. The large concentration of population in midlatitudes, especially in the northern hemisphere, combined with trends in ozone loss in this region (Logan et al., 1999) and recent observations of midlatitude stratospheric water enhancements by convection, make predicting the response of stratospheric water vapor and ozone to increased forcing a pressing issue of public health. Additionally, understanding the mechanisms that control the oxidation of atmospheric mercury in the Arctic spring is necessary to gauge the impact of and regulate public health concerns of bio-accumulation of toxins.

To guide these debates, observations combined with models must be able to address these challenging issues. The problem is compounded by the fact these processes occur in a system where forcing is changing such that understanding the response to forcing is an additional burden that scientific understanding must carry. To conclude, a selected number of outstanding questions, along with brief discussions,

are posed to which the *in situ* instruments and measurements presented previously can contribute:

• Is it possible to quantify the fluxes of water that determine the humidity of the stratosphere?

The challenge of properly quantifying the net flux that determines the humidity of the TTL and stratosphere remains a challenge. Direct measurements of the isotopic composition of ice from convection aid this problem by providing constraints on the role of convection, yet the application to the global scale is hampered by the limited observations. The degree to which observations from a single event in the TTL, as presented in chapter 3, can be extrapolated to represent the bulk behavior of convection in the TTL is uncertain—in the TTL convection reaches different altitudes, occurs in different seasons, over different geographical features and at different latitudes. Only with observations that account for such possible variations can a true global picture emerge.

Quantifying the role of transport by the use of convective tracers requires a level of sensitivity that is an abiding challenge for *in situ* instruments. While remote measurements of HDO, and hence δD, are available from various satellite instruments (e.g., TES, ACE-FTS, and MIPAS), the limited spatial and temporal resolution they provide makes it difficult to address small scale structures that are exceedingly important for the diagnosis of specific mechanisms for convection. High temporal and spatial resolution measurements with large geographical coverage remain in the province of *in situ* instruments deployed aboard a new generation of observing platforms.

• **Is there a secular trend in stratospheric water vapor?**

The debate over the existence of a secular trend in stratospheric water vapor continues and in large part stems from the difficulty of making accurate measurements at the low mixing ratios in the stratosphere. The uncertainty in a secular trend has consequences that potentially impacts our understanding of surface temperature trends in addition to the factors that control stratospheric ozone. For instance, Solomon et al. (2010) has argued that the $\sim$ 10 % decrease in stratospheric water vapor since the year 2000 has contributed to a slowing of the rate of increase of global surface temperatures by about 25 % over the same period. Yet the abrupt decrease in stratospheric water in 2000 reported by the HALOE instrument, flown onboard the UARS satellite, lies within the range of the largely unresolved biases between instruments measuring stratospheric water vapor.

• **What is the origin of cirrus clouds in the TTL?**

Another question that remains for total water isotope measurements is determining the origin of cirrus in the TTL. The observation of ice clouds in the region of convective outflow during TC4 does help to answer how water and ice are transported into the TTL, but the question as to how this ice evolves and to what extent it hydrates the TTL remains an open question. The ice may humidify or dehydrate the TTL, depending on the past and future history of the air the ice was injected into. The genesis of persistent cirrus remains an open question: are TTL cirrus formed directly in the TTL by condensation of water vapor or are they the remnants of deep convection which has since dissipated? As observations of the isotopic composition of ice show, these two processes can be differentiated, yet the ice isotopes

have only been observed during active convection and not in absence of nearby convection. Thin, persistent cirrus that influence the distribution of water and radiative properties of the TTL must be directly sampled to understand their origin.

• **What is the spatial and temporal homogeneity of VSLS transport into the TTL? How efficiently are VSLS transported through the TTL into the stratosphere?**

The halogen contribution to lower stratospheric ozone destruction remains an open question and the effectiveness of halogen sources (e.g., methyl iodide), released at the surface, towards stratospheric ozone destruction may be influenced by the season and region of its release. Such confined enhancement is thought to occur in the Arctic, where closure of total column BrO "hotspots" requires a 5 – 10 ppt source of bromine in the Arctic lowermost stratosphere that is thought to originate from short-lived biogenic bromocarbons (Salawitch et al., 2010).

Chemical processing in the TTL is directly linked to convection and (de)hydration pathways in the TTL. The mixing ratios of these VSLS at the base of the TTL are determined by the convective processes which transport them. But the efficacy by which they enter the lower stratosphere is determined by the details of their transport through the TTL. The factors that influence this include: the residence time of air in the TTL; the photochemical lifetime of the VSLS; the ice solubility of VSLS; and the rate of removal of ice from the TTL. Accurately describing the transport of VSLS through the TTL requires a detailed understanding of transport and the (de)hydration pathways that air is subjected to in the TTL.

• **Is there a seasonal cycle in tropical convection and, if so, how does**

this impact the transport of water into the stratosphere? What role does midlatitude convection play in moistening the stratosphere? How will it respond to changes in forcing?

Understanding seasonality of convection in the TTL and its impact on the δD of water entering the tropical stratosphere are a requirement to disentangle midlatitude contributions. There is evidence of transport of a large amount of water into the stratosphere in the midlatitudes for individual cells and during regional convection (e.g., Asian monsoon), but the contribution of such convection to the overall distribution of water in the stratosphere is unresolved. Observations of water vapor isotopes in the outflow of deep convection in the midlatitudes suggest that the convective contribution could account for up to 58 % of the water vapor in the midlatitude stratosphere (Hanisco et al., 2007). This analysis is subject to uncertainties in the dynamics of stratosphere-troposphere exchange in other regions, primarily in the tropics and from the Asian monsoon, such that the actual contribution may be much smaller. This highlights the importance of understanding regional transport in a global context and the significant role the midlatitudes may have in stratospheric transport pathways.

• **What is the source of atmospheric halogens in the Arctic? How are the reaction networks of the halogens (Cl, Br, I) coupled to heavy metal chemistry in the Arctic and Antarctic? How will Arctic halogen chemistry respond to an ice-free Arctic ocean?**

The mechanism by which halogens enter the atmosphere during the spring time blooms is thought to occur via the conversion of ocean halides to photolabile gases

by heterogenous chemistry occurring on sea ice. However, the mechanism by which this conversion occurs is still debated. While chlorine, and to a larger extent bromine, are thought to be responsible for the conversion of gaseous elemental mercury to a more reactive form, large enhancements in the rate of mercury oxidation and ozone depletion during the Arctic spring are predicted with the addition of iodine-containing compounds (Calvert and Lindberg, 2004a,b).

If sea ice is required to generate atmospheric bromine from oceanic bromide, how will Arctic halogen-mercury-ozone chemistry be impacted by ice-free conditions, predicted to occur as soon as the end of this century. Voulgarakis et al. (2009) ran a model under such conditions and found that both bromine chemistry and OH concentrations will decline. Once the Arctic is ice-free for prolonged periods, stretching from spring until early summer, a large local increase in ozone is seen that can extend into inhabited high latitude regions. Results from this model are subject to sea ice extent as this is required to produce atmospheric bromine. Observations of atmospheric iodine over ice-free regions in the mid-latitudes, at both coastal sites and over the open-ocean (Lai et al., 2011), suggest the possibility of alternate pathways for atmospheric entry.

References

J. G. Calvert and S. E. Lindberg. Potential influence of iodine-containing compounds on the chemistry of the troposphere in the polar spring. I. Ozone depletion. *Atmospheric Environment*, 38(30):5087 – 5104, 2004a. doi: 10.1016/j.atmosenv.2004.05.049.

J. G. Calvert and S. E. Lindberg. The potential influence of iodine-containing compounds on the chemistry of the troposphere in the polar spring. II. Mercury depletion. *Atmospheric Environment*, 38(30):5105 – 5116, 2004b. doi: 10.1016/j.atmosenv.2004.05.050.

T. F. Hanisco, E. J. Moyer, E. M. Weinstock, J. M. St. Clair, D. S. Sayres, J. B. Smith, R. Lockwood, J. G. Anderson, A. E. Dessler, F. N. Keutsch, J. R. Spackman, W. G. Read, and T. P. Bui. Observations of deep convective influence on stratospheric water vapor and its isotopic composition. *Geophysical Research Letters*, 34(4), 02 2007.

S. C. Lai, J. Williams, S. R. Arnold, E. L. Atlas, S. Gebhardt, and T. Hoffmann. Iodine containing species in the remote marine boundary layer: A link to oceanic phytoplankton. *Geophysical Research Letters*, 38:L20801, Oct. 2011. doi: 10.1029/2011GL049035.

J. A. Logan, I. A. Megretskaia, A. J. Miller, G. C. Tiao, D. Choi, L. Zhang, R. S. Stolarski, G. J. Labow, S. M. Hollandsworth, G. E. Bodeker, H. Claude, D. D. Muer, J. B. Kerr, D. W. Tarasick, S. J. Oltmans, B. Johnson, F. Schmidlin, J. Staehelin, P. Viatte, and O. Uchino. Trends in the vertical distribution of ozone: A comparison of two analyses of ozonesonde data. *Journal of Geophysical Research*, 104:26373–26400, 1999. doi: 10.1029/1999JD900300.

R. J. Salawitch, T. Canty, T. Kurosu, K. Chance, Q. Liang, A. da Silva, S. Pawson, J. E. Nielsen, J. M. Rodriguez, P. K. Bhartia, X. Liu, L. G. Huey, J. Liao, R. E. Stickel, D. J. Tanner, J. E. Dibb, W. R. Simpson, D. Donohoue, A. Weinheimer, F. Flocke, D. Knapp, D. Montzka, J. A. Neuman, J. B. Nowak, T. B. Ryerson, S. Oltmans, D. R. Blake, E. L. Atlas, D. E. Kinnison, S. Tilmes, L. L. Pan, F. Hendrick, M. Van Roozendael, K. Kreher, P. V. Johnston, R. S. Gao, B. Johnson, T. P. Bui, G. Chen, R. B. Pierce, J. H. Crawford, and D. J. Jacob. A new interpretation of total column BrO during Arctic spring. *Geophysical Research Letters*, 37:L21805, Nov. 2010. doi: 10.1029/2010GL043798.

S. Solomon, K. H. Rosenlof, R. W. Portmann, J. S. Daniel, S. M. Davis, T. J. Sanford, and G.-K. Plattner. Contributions of Stratospheric Water Vapor to Decadal Changes in the Rate of Global Warming. *Science*, 327:1219–, Mar. 2010. doi: 10.1126/science.1182488.

A. Voulgarakis, X. Yang, and J. A. Pyle. How different would tropospheric oxidation be over an ice-free Arctic? *Geophysical Research Letters*, 36:L23807, Dec. 2009. doi: 10.1029/2009GL040541.